Numerical Study of Different Micro Gas Turbine Combustor Design Configurations for Hydrogen Operation

Numerische Untersuchung verschiedener Designkonfigurationen einer Mikrogasturbinen-Brennkammer für Wasserstoffbetrieb
Master thesis by Akshay Sanjay Vibhute
Date of submission: 17.03.2024

1. Review: Prof. Dr.-Ing. Christian Hasse
2. Review: Dr.-Ing. Hendrik Nicolai
Stuttgart

TECHNISCHE UNIVERSITÄT DARMSTADT

STFS
Simulation of reactive Thermo-Fluid Systems

DLR

Numerical Study of Different Micro Gas Turbine Combustor Design Configurations for Hydrogen Operation
Numerische Untersuchung verschiedener Designkonfigurationen einer Mikrogasturbinen-Brennkammer für Wasserstoffbetrieb

Master thesis by Akshay Sanjay Vibhute

Date of submission: 17.03.2024

Stuttgart

Erklärung zur Abschlussarbeit gemäß § 22 Abs. 7 und § 23 Abs. 7 APB der TU Darmstadt

Hiermit versichere ich, Akshay Sanjay Vibhute, die vorliegende Masterarbeit ohne Hilfe Dritter und nur mit den angegebenen Quellen und Hilfsmitteln angefertigt zu haben. Alle Stellen, die Quellen entnommen wurden, sind als solche kenntlich gemacht worden. Diese Arbeit hat in gleicher oder ähnlicher Form noch keiner Prüfungsbehörde vorgelegen.

Mir ist bekannt, dass im Fall eines Plagiats (§ 38 Abs. 2 APB) ein Täuschungsversuch vorliegt, der dazu führt, dass die Arbeit mit 5,0 bewertet und damit ein Prüfungsversuch verbraucht wird. Abschlussarbeiten dürfen nur einmal wiederholt werden.

Bei der abgegebenen Thesis stimmen die schriftliche und die zur Archivierung eingereichte elektronische Fassung gemäß § 23 Abs. 7 APB überein.

Bei einer Thesis des Fachbereichs Architektur entspricht die eingereichte elektronische Fassung dem vorgestellten Modell und den vorgelegten Plänen.

A.S.Vibhte

Stuttgart, 17.03.2024

Akshay Sanjay Vibhute

Acknowledgements

The present work was conducted during my tenure as a Master's Thesis student at the Institute of Combustion Technology (VT), DLR Stuttgart. Firstly, I would like to express my gratitude to Dr. Felix Grimm for extending me this Thesis opportunity, providing an overview of the department, and arranging the necessary resources for my work.

I would like to extend a special and sincere thanks to Mr. Timo Lingstädt for serving as a co-supervisor in the initial days and then transitioning into my main supervisor after Dr. Grimm's departure. I am truly grateful for the technical and organisational insights that Mr. Lingstädt shared throughout the duration of my Thesis. I would also like to acknowledge and thank Mr. Karl Planke for his unofficial supervisory role and for his assistance in creating automation scripts. In addition to my supervisors, I would like to take this opportunity to express my appreciation to Professor Dr. Andreas Huber, the head of the Institute and Dr. Peter Kutne, head of the MGT Department for providing the necessary resources to carry out this research. I am also grateful to my colleagues at the institute for building a fun and positive atmosphere, particularly the members of the Micro Gas Turbines (MGT) department, who were always willing to lend a helping hand.

Furthermore, I am grateful to Professor Dr. Christian Hasse and Dr. Hendrik Nicolai for acting as supervisors from the university's side. I truly value their prompt responses, especially when dealing with the bureaucracy of Thesis registration. I would also like to extend my thanks to the rest of the STFS department, as their work 'ignited' my interest in the field of reactive flows. Lastly, I would like to express my gratitude to all the professors and colleagues at TU Darmstadt for their invaluable teachings and support.

To my friends who helped me acclimate to Germany and the kind strangers I encountered during my nearly two-year stay in this country, I am incredibly grateful. A warm thank you goes to my family members as well.

However, my deepest and most heartfelt thanks go to my mother, Sneha, and my late grandparents. Despite the hardships faced, you never sidelined my ambitions and always encouraged me to strive to go onwards and upwards.

Stuttgart, March 2024, Akshay Sanjay Vibhute

German Aerospace Center (DLR)
Institute of Combustion Technology
Pfaffenwaldring 38-40, 70569 Stuttgart

Master Thesis

for cand. aer. Akshay Vibhute

Numerical Study of Different Micro Gas Turbine Combustor Design Configurations for Hydrogen Operation

Numerische Untersuchung verschiedener Designkonfigurationen einer Mikrogasturbinen-Brennkammer für Wasserstoffbetrieb

Task Description:

With the upcoming task of renewable energy supply based on hydrogen as energy storage and transport media, decentralized hydrogen combustion in micro gas turbines has become a topic of interest. In this work, different modifications of a jet stabilized DLR combustor and their influence on combustion stability, operating range and NOx pollutant formation will be investigated and evaluated for its optimization potential.

The numerical data to be generated will extend the picture of the influence of different design parameters and boundary conditions like premixing length, pilot stage concept operating pressure and fuel air distribution. Existing experimental data from atmospheric tests will be used for validation of the numerical setup and results.

Finally, general design rules and best practices should be derived based on the findings to supplement the future hydrogen combustor design strategy at DLR.

The thesis topic is suitable for the study programme of Aerospace Engineering.

Work Steps:

- Familiarization with computational fluid dynamics, mesh generation, combustion and turbulence modeling, pollutant formation, parallelization and high-performance computing
- Training in used software (CATIA, Ansys Meshing, in-house CFD and chemistry solver ThetaCOM, Tecplot)
- Model- and mesh preparation for combustor configurations of interest
- Preparation, execution and monitoring of CFD and combustion simulations with detailed chemistry on high-performance computing resources
- Validation of results with experimental data and interpretation
- Derivation of general combustor design rules for investigated geometry and boundary condition variations
- Documentation

Place and Time Schedule:

The Master Thesis can be prepared at DLR Stuttgart and/or from home and should be finished within 6 months. A presence on site of at least 2 days per week is highly appreciated for most efficient exchange and supervision.

Start Date: 01.10.2023 **Submission Date:** 31.03.2024

Main Supervisor:

Dr. Christian Hasse

Digital unterschrieben von Dr. Christian Hasse
Datum: 2023.07.06 11:30:53 +02'00'

Prof. Christian Hasse

DLR Supervisor:

Timo Lingstaedt

Digital signiert von Timo Lingstaedt
DN: C=DE, S=Nordrhein-Westfalen, L=Koeln, O=Deutsches Zentrum fuer Luft- und Raumfahrt e.V. (DLR), SN=Lingstaedt, G=Timo , CN=Timo Lingstaedt
Grund: Ich bin der Verfasser dieses Dokuments
Ort: Stuttgart
Datum: 2023.07.06 10:38:09+02'00'
Foxit PDF Reader Version: 12.1.2

Dipl.-Ing. Timo Lingstädt

Abstract

With the upcoming task of supplying renewable energy through the use of hydrogen as an energy storage and transport medium, there has been a growing interest in decentralised hydrogen combustion in ***M****icro* ***G****as* ***T****urbines (MGT). Hydrogen, as a carbon-free energy carrier, plays an important role in the decarbonisation of energy systems. It serves as a means of energy storage and as a fuel for dispatchable power generation in an attempt to mitigate the intermittent nature of renewable energy sources. Nonetheless, the distinctive attributes of hydrogen, which set it apart from conventional gaseous fuels like biogas and natural gas, introduce new challenges that require attention. To seamlessly incorporate hydrogen as an energy carrier within the energy system, it is essential to develop advanced solutions that are both low-emission and highly reliable. This work aims investigate different modifications of an atmospheric combustor of a DLR MGT - Turbec T100, using* ***C****omputational* ***F****luid* ***D****ynamics (CFD), specifically the* ***R****eynolds-****A****veraged* ***N****avier* ***S****tokes (RANS) method and assess the impact on combustion stability, operating range, and* NO_x *pollutant formation.*

The study begins with a literature review that highlights some of the previous relevant research and potential issues associated with hydrogen combustion, such as high adiabatic temperatures, higher NO_x *emissions, and flame flashbacks. The fundamentals of reactive flows, Reynolds averaging, turbulence and combustion models are also discussed.*

The work then discusses the obtained results. The simulation results for the jet-stabilised pilot stage configurations were consistent and aligned with the general expectations and trends. A noteworthy observation in this work was the impact of premixing on the recirculation zones, where the non-premixed variant had an additional, outer recirculation zone. While some discrepancies were observed for two air-fuel ratios in the swirl-stabilised pilot stage configuration, here too the results were consistent for rest of the operating points.

For all of the tested configurations, the NO_x *emissions were well below the EU regulations for* NO_x *emissions in new gas turbines. Additionally, no flame flashbacks and flame blowout phenomena was observed. It was concluded that the lowest* NO_x *emissions were observed in the non-premixed, jet-stabilised variant. The study also acknowledges the limitations of the RANS approach and encourages further research using additional experiments and high-fidelity simulation methods.*

Keywords: *CFD, Combustion, MGT, Chemiluminescence,* NO_x *emissions*

Kurzfassung

*Mit der bevorstehenden Aufgabe, erneuerbare Energien durch den Einsatz von Wasserstoff als Energiespeicher und Transportmedium bereitzustellen, ist das Interesse an der dezentralen Wasserstoffverbrennung in Mikrogasturbinen (MGT) gestiegen. Wasserstoff spielt als kohlenstofffreier Energieträger eine entscheidende Rolle bei der Dekarbonisierung der Energiesysteme. Er dient sowohl als Option zur Energiespeicherung als auch als Brennstoff für die abschaltbare Stromerzeugung, um den intermittierenden Charakter der erneuerbaren Energiequellen auszugleichen. Die einzigartigen Eigenschaften von Wasserstoff, die sich von denen herkömmlicher gasförmiger Brennstoffe wie Biogas und Erdgas unterscheiden, stellen jedoch neue Herausforderungen dar, die bewältigt werden müssen. Um Wasserstoff als Energieträger vollständig in das Energiesystem zu integrieren, müssen unbedingt emissionsarme und äußerst zuverlässige Technologien entwickelt werden, die die Verbrennung von Wasserstoff beherrschen. In dieser Arbeit werden verschiedene Modifikationen einer atmosphärischen Brennkammer eines DLR **M**icro **G**as **T**urbine (MGT) - Turbec T100 mit Hilfe von **C**omputational **F**luid **D**ynamics (CFD), insbesondere der **R**eynolds-**A**veraged **N**avier **S**tokes (RANS)-Methode, untersucht und die Auswirkungen auf die Verbrennungsstabilität, den Betriebsbereich und die* NO_x*-Schadstoffbildung bewertet. Die Studie beginnt mit einem Literaturüberblick, der einige der bisherigen einschlägigen Forschungsarbeiten und potenzielle Probleme im Zusammenhang mit der Wasserstoffverbrennung aufzeigt, wie beispielsweise hohe adiabatische Temperaturen, höhere* NO_x*-Emissionen und Flammenrückschläge. Außerdem werden die Grundlagen reaktiver Strömungen, Reynolds-Mittelung, Turbulenz und Verbrennungsmodelle erörtert.*

Anschließend werden die erzielten Ergebnisse erörtert. Die Simulationsergebnisse für die strahlstabilisierten Pilotstufenkonfigurationen waren konsistent und stimmten mit den allgemeinen Erwartungen und Trends überein. Eine bemerkenswerte Beobachtung in dieser Arbeit war die Auswirkung der Vormischung auf die Rezirkulationszonen, wobei die nicht vorgemischte Variante eine zusätzliche, äußere Rezirkulationszone aufwies. Während bei zwei Luft-Kraftstoff-Verhältnissen in der drallstabilisierten Pilotstufenkonfiguration einige Diskrepanzen beobachtet wurden, waren auch hier die Ergebnisse für die übrigen Betriebspunkte konsistent.

Bei allen getesteten Konfigurationen lagen die NO_x*-Emissionen deutlich unter den EU-Vorschriften für* NO_x*-Emissionen bei neuen Gasturbinen. Außerdem wurden keine Flammenrückschläge und Flammenblasen beobachtet. Es wurde festgestellt, dass die niedrigsten* NO_x*-Emissionen bei der nicht vorgemischten, strahlstabilisierten Variante beobachtet wurden. Die Studie räumt auch die Grenzen des RANS-Ansatzes ein und regt zu weiteren Forschungen mit zusätzlichen Experimenten und High-Fidelity-Simulationsmethoden an.*

Schlüsselwörter: *CFD, Verbrennung, Gasturbinen (MGT), Chemilumineszenz,* NO_x*-Emissionen*

Table of Contents

Nomenclature

Latin Symbols

Symbol	**Meaning**	***Unit***
A_0	Constant of the *Realizable* k-ε turbulence model	-
A	Empirical Combustion model constant	-
a_1	Constant of the k-ω-*SST* turbulence model	-
A_r	Arrhenius prefactor	*variable*
A_s	Constant of the *Realizable* k-ε turbulence model	-
B	Empirical combustion model constant	-
c	Speed of sound	*m/s*
C_1, C_2	Constants of the *Standard* k-ε turbulence model	-
C_2^*	Parameter of the *RNG* k-ε turbulence model	-
$CD_{k\omega}$	Cross-Diffusion term of the k-ω-*SST* turbulence model	-
c_p	Specific heat capacity at constant pressure	*J/(kgK)*
C_μ	Constant of the *Standard* k-ε turbulence model	-
C_τ	Constant of the EDC combustion model	-
C_ζ	Constant of the EDC combustion model	-
$\underline{\underline{\boldsymbol{D}}}$	Diffusion coefficient	m^2/s
D_k	Diffusion of turbulent kinetic energy	m^2/s
D_t	Turbulent diffusion coefficient	m^2/s
e^a	Approximate relative error	-
$E_{\alpha,r}$	Activation energy for reaction r	*J/kg*
$\boldsymbol{F}$	Cartesian flux vector	*variable*
$\boldsymbol{f}$	Vector of external forces	m/s^2
f	Frequency	*1/s*
f	Autocorrelation function	-
F_1, F_2	Blending functions of the k-ω-*SST* turbulence model	-
$\boldsymbol{G}_\Omega$	Flux vector normal to the cell surface	*variable*
$\boldsymbol{G}_k$	Mean flux vector	*variable*
h	Specific enthalpy	*J/kg*
$h^0{}_{f,\alpha}$	Standard formation enthalpy, species α	*J/kg*
$\boldsymbol{I}$	Identity matrix	-
$\underline{\underline{\boldsymbol{j}}}$	Diffusion mass flux	$kg/(m^2s)$
k	Turbulent kinetic energy	m^2/s^2
k_{br}	Rate constant of the backward reaction	*1/s*
k_{fr}	Rate constant of the forward reaction	*1/s*
L_t	Turbulent time scale	*s*

Symbol	**Meaning**	***Unit***
l_t	Turbulent length scale	*m*
M_α	Molar mass of a species	*kg/mol*
$\dot{m}$	Mass flow rate	*kg/s*
M^*_{tr}	Transfer rate of the EDC model	*1/s*
n	Dimension	-
n_i	Surface normal vector	-
N_r	Number of elementary reactions	-
N_s	Number of species in the mixture	-
O	Order	-
$\boldsymbol{P}$	Iteration matrix	*variable*
p	Pressure	*Pa*
p_{abs}	Absolute Pressure	*Pa*
p_{ref}	Reference Pressure	*Pa*
P_k	Production of Turbulent Kinetic Energy	*kg/(m·s^3)*
$\tilde{P}_k$	Production Term in the $k-\omega$ *SST* Turbulence Model	*kg/(m·s^3)*
P_{therm}	Thermal Power	*W*
R	Specific Gas Constant	*J/(kg·K)*
$\dot{R}_\alpha$	Mass Transfer Rate of Species α	*kg/(m^{3}s)*
RH	Reaction Heat/Integrated Heat Release/Thermal Power	*J/s*
R_m	Universal Gas Constant	*J/(mol·K)*
RR_r	Reaction Rate of Reaction r	*mol/(m^{3}s)*
S_α	Chemical Source Term	*kg/(m^{3}s)*
S_{ij}	Strain rate Tensor	*1/s*
S^0_L	Local Flame speed	*m/s*
T	Temperature	*K*
T_0	Temperature under atmospheric reference conditions	*K*
t	Time	*s*
$\boldsymbol{u}$	Velocity vector	*m/s*
U_t	Turbulent velocity scale	*m/s*
u, v, w	Velocity components	*m/s*
V	Control volume/Cell volume	*m^3*
V	Velocity magnitude	*m/s*
x, y, z	Cartesian coordinates	*m*
y	Wall distance in the $k-\omega$ *SST* turbulence model	*m*
$\boldsymbol{Y}_\alpha$	Species vector	-
Y_α	Mass fraction of species α	-
Y^*_α	Mass fraction of species α within the fine structures	-

Greek Symbols

Symbol	**Meaning**	***Unit***
α	Species index	-
α	Constant of the $k-\omega$ *SST* turbulence model	-
α_1	Constant of the $k-\omega$ *SST* turbulence model	-
α_2	Constant of the $k-\omega$ *SST* turbulence model	-

Symbol	**Meaning**	***Unit***
β	Constant of the $k-\omega$ *SST* turbulence model	-
β_1	Constant of the $k-\omega$ *SST* turbulence model	-
β_2	Constant of the $k-\omega$ *SST* turbulence model	-
β^*	Constant of the $k-\omega$ *SST* turbulence model	-
β_r	Temperature exponent	-
δ_f	Flame thickness	*m*
Γ	Gamma function	-
Δx	Grid spacing	*m*
Δt	Time step	*s*
ε	Turbulent dissipation rate	m^2/s^2
ζ^*	Parameter of the EDC combustion model	-
η	Parameter of the *RNG* *k*-ε turbulence model	-
η_0	Constant of the *RNG* *k*-ε turbulence model	-
λ	Air-fuel ratio	-
λ	Thermal conductivity	*W/(mK)*
λ_t	Turbulent thermal conductivity	*W/(mK)*
μ	Dynamic viscosity	*kg/(m·s)*
μ_t	Turbulent dynamic viscosity	*kg/(m·s)*
ν	Kinematic viscosity	m^2/s
ν_t	Turbulent kinematic viscosity	m^2/s
$\nu'_{\alpha,r}$, $\nu''_{\alpha,r}$	Stoichiometric coefficients, reactant ('), and product side (")	-
ρ	Density	kg/m^3
σ	Constant of the $k-\omega$ *SST* turbulence model	-
σ^*	Constant of the $k-\omega$ turbulence model	-
σ_k	Constant of the *RNG* *k*-ε turbulence model	-
σ_{k1}	Constant of the $k-\omega$ *SST* turbulence model	-
σ_{k2}	Constant of the $k-\omega$ *SST* turbulence model	-
σ_ε	Constant of the *standard* *k*-ε turbulence model	-
σ_ω	Constant of the $k-\omega$ *SST* turbulence model	-
$\sigma_{\omega 1}$	Constant of the $k-\omega$ *SST* turbulence model	-
$\sigma_{\omega 2}$	Constant of the $k-\omega$ *SST* turbulence model	-
$\underline{\underline{\tau}}$	Shear stress tensor	N/m^2
τ_{ign}	Ignition delay time	*s*
τ_m	Time scale of the mean flow field	*s*
τ_t	Turbulence timescale	*s*
τ^*	Timescale of the fine structures	*s*
ϕ	Equivalence ratio	-
ϕ	Arbitrary flow quantity	*variable*
π	Pi (mathematical constant)	-
ω	Turbulent frequency	*1/s*
Ω	Cell surface area	m^2
Ω_{ij}	Rotation tensor	-

Indices and Accents

Index/Accent	Meaning
ϕ	Parameter
ϕ_0	Reference state
ϕ_{abs}	Absolute value
ϕ_{initial}	Initial condition
ϕ_α	Species
ϕ_b	Backwards
ϕ_{fuel}	Fuel
ϕ_f	Forwards
ϕ_{air}	Air
ϕ_{max}	Maximum value
ϕ_{min}	Minimum value
ϕ_{mod}	Modification
ϕ_r	Elementary reaction
ϕ_{ref}	Reference
ϕ_{stoich}	Stoichiometric ratio
ϕ_t	Turbulence-related quantity
ϕ^*	Dimensionless
$\overline{\phi}$	Mean of a Reynolds-decomposed quantity
$\widetilde{\phi}$	Mean of a Favre-decomposed quantity
ϕ'	Fluctuation of a Reynolds-decomposed quantity
ϕ''	Fluctuation of a Favre-decomposed quantity

Operators

Operator	Meaning
ϕ	Scalar
$\boldsymbol{\phi}$	Vector
$\underline{\underline{\boldsymbol{\phi}}}$	Matrix
$\frac{\partial \phi}{\partial x}$	Partial derivative of ϕ with respect to x
$\frac{D\phi}{Dt}$	Material derivative of ϕ with respect to time t
$\int \phi \, dV$	Integral of ϕ over the volume V
$\int \phi \, dx$	Integral of ϕ over x
$\sum_{i=1}^{n} \phi$	Sum of ϕ from $i = 1$ to $i = n$
$\prod_{i=1}^{n} \phi$	Product of ϕ from $i = 1$ to $i = n$
$\phi \cdot \psi$	Dot product of ϕ and ψ
$\phi \otimes \psi$	Dyadic product of ϕ and ψ
$\underline{\underline{\boldsymbol{\phi}}} : \underline{\underline{\boldsymbol{\psi}}}$	Frobenius inner product of $\underline{\underline{\boldsymbol{\phi}}}$ and $\underline{\underline{\boldsymbol{\psi}}}$
$\nabla \phi$	Gradient of ϕ
$\nabla \cdot \phi$	Divergence of ϕ
$\exp(\phi)$	Exponential function of ϕ
$\max(\phi, \psi)$	Maximum of ϕ and ψ

Operator	**Meaning**
$\min(\phi, \psi)$	Minimum of ϕ and ψ
$\tanh(\phi)$	Hyperbolic tangent of ϕ

Dimensionless Numbers

Notation	**Number**
Da	Damköhler Number
Ka	Karlovitz Number
Le	Lewis Number
Pr	Prandtl Number
Re_t	Reynolds Number
Sc	Schmidt Number

Constants

Model	**Constants**
Standard $k-\varepsilon$ Turbulence Model	C_1, C_2, C_μ, σ_k, σ_ε
RNG $k-\varepsilon$ Turbulence Model	β, C_1, C_2, C_μ, σ_k, σ_ε, η
Realizable $k-\varepsilon$ Turbulence Model	A_0, C_2, σ_k, σ_ε
$k-\omega$ Turbulence Model	α, β, β^*, σ, σ^*
$k-\omega$ SST Turbulence Model	a_1, α_1, α_2, β_1, β_2, β^*, σ_{k1}, σ_{k2}, $\sigma_{\omega 1}$, $\sigma_{\omega 2}$
EDC Combustion Model	C_ζ, C_τ, ζ^*
Arrhenius Equation	A, β

Chemical Formulae

Chemical Symbol	**Meaning**
H_2	Hydrogen
N_2	Nitrogen
NO	Nitric Monoxide
NO_2	Nitrogen Dioxide
N_2O	Dinitrogen oxide
O_2	Oxygen
OH	Hydroxyl Radical
CO_2	Carbon Dioxide
CO	Carbon Monoxide

Abbreviations

Abbreviation	**Meaning**
ATM	Atmosphere
CDS	Central Difference Scheme
CFD	Computational Fluid Dynamics
CIVB	Combustion-Induced Vortex Breakdown
CPU	Central Processing Unit
DC1S30N18	DLR Concise High Temperature Reaction Mechanism for fuel surrogate
DLR	Deutsches Zentrum für Luft und Raumfahrt (German Aerospace Center)
DNS	Direct Numerical Simulation
EDC	Eddy Dissipation Concept
EDM	Eddy Dissipation Model
EU	European Union
FDM	Finite Difference Method
FLOX®	Flameless Oxidation
FRC	Finite Rate Chemistry
FVM	Finite Volume Method
GCI	Grid Convergence Index
GMRES	Generalised Minimal RESidual
LDS	Linear Difference Scheme
LES	Large Eddy Simulation
LHV	Lower Heating Value
LoS	Line of Sight
MGT	Micro Gas Turbine
NS	Navier-Stokes
OH	Hydroxyl Radical
PBCGS	Preconditioned Bi-Conjugate Gradient Stabilised
QUDS	Quadratic Upwind Difference Scheme
RANS	Reynolds-Averaged Navier-Stokes
RH	Reaction Heat
RLZ	Realizable
RNG	Renormalization Group
RSM	Reynolds Stress Model
SIMPLE	Semi-Implicit Method for Pressure-Linked Equations
THETA	Turbulent Heat Release Extension of the TAU code
SST	Shear Stress Transport
UDS	Upwind Difference Scheme
UHC	Unburnt Hydrocarbons
URANS	Unsteady Reynolds-Averaged Navier-Stokes
VOCs	Volatile Organic Compounds
VT	Institut für Verbrennungstechnik/ Institute of Combustion Technology, DLR Stuttgart

1. Introduction

1.1. Motivation

Micro **G**as **T**urbine (MGT) , with a power output ranging from 3 to 300 kW, play a crucial role in decentralised power generation. Their reliability and ability to quickly respond to load changes make them an ideal backup option for intermittent renewable energy sources [44, 136]. Furthermore, their compact size, lightweight design, and low installation and maintenance costs further enhance the position of MGTs as power generators in future distributed power systems [137]. Currently, MGTs can run on a variety of fuels, ranging from high-heating value fuels like methane and natural gas to lower-heating value fuels like biogas.

Despite the fuel-flexibility of MGTs offering a wide range of options, concerns regarding greenhouse gas emissions from carbon-based fuels persist. In order to achieve zero net CO_2 emissions in an MGT, considering the difficulties associated with capturing CO_2 due to its low partial pressure [125], the most efficient approach is to utilise carbon-free fuels, such as hydrogen, or carbon-neutral fuels. This transition from the current power generation infrastructure, which predominantly relies on carbon-based fuels, necessitates bridging technologies like fuel-flexible MGTs that can accommodate blended fuels containing high levels of hydrogen [111].

Hydrogen fuel has the potential to significantly contribute to the transition towards a more sustainable and low-carbon energy system in the heat and power generation sector [137]. One advantage of using hydrogen in power generation is its ability to substantially reduce greenhouse gas emissions and improve air quality, as it only emits water vapor during combustion, in contrast to traditional fossil fuels like coal and natural gas, which release harmful pollutants. By utilising hydrogen as an energy storage solution, excess energy generated from renewable sources can be stored and used when renewable sources are not available. This guarantees a consistent and dependable energy supply [140].

1.2. Objectives and Limitations of this work

At the Institute for Combustion Technology (VT) of the German Aerospace Center (DLR), among other things, numerical combustion simulations for combustion chamber systems are developed and optimised.

The primary objectives of this thesis are as follows:

1. To examine the impact of different design modifications on the combustion stability, flame temperatures, operating range, NO_x pollutant emissions, and the formation of recirculation zones in a DLR combustion chamber. These modifications include variations in the pilot stage, such as jet versus swirl stabilisation, as well as the presence or absence of premixing. Additionally, the study will explore the effects of varying the air-fuel compositions.

2. To review relevant literature in order to understand the current trends regarding the use of hydrogen as a sustainable alternative fuel. Furthermore, this literature review will also identify the challenges associated with operating a gas turbine on hydrogen.
3. To carry out a comprehensive study aimed at determining the optimal grid settings and turbulence model that accurately replicate the experimental results.
4. To adhere to best practices for documenting the findings and results, and to provide insights for the development of the combustion chamber.

The limitations of this work are primarily attributed to the computational capabilities of modern supercomputers as it still remains the primary constraining factor for conducting complex flow simulations. Even the most advanced computing centers get fairly taxed with solving basic flow problems involving simple geometries using the fundamental **N**avier-**S**tokes (NS) equations. The main challenge arises from the **D**irect **N**umerical **S**imulation (DNS) approach, which necessitates resolving even the smallest turbulent scales by employing computation grids with sufficiently high resolution. However, refining the grid leads to a disproportionate increase in the number of cells and the required computing time [116]. Given that the computational effort does not directly correspond to the benefit of the simulation, simplifications are introduced to reduce the computing time. These simplifications involve applying averaging methods to the NS equations (see section 2.2), which effectively filter out or partially represent the turbulent spectrum. Consequently, the smallest turbulent scales are often modeled rather than explicitly resolved, allowing for a coarser computation grid and significantly reducing the computing time.

Therefore, the accuracy of the employed models emerges as the primary limiting factor. While averaging and simplifications inevitably result in a loss of information, they ensure that the simulation effort remains proportional to its benefit.

1.3. Previous Work and Literature Study

Both large-scale and small-scale gas turbine units have been the subject of numerous research and development initiatives aiming to address the challenges associated with using pure hydrogen or hydrogen-blended fuels. In 1998, Morris et al. published a paper [41] presenting their findings on incorporating hydrogen into heavy-duty gas turbines originally designed for natural gas. The authors reported that the addition of 10% hydrogen had no significant impact on NO_x emissions, but it did reduce carbon monoxide production.

In a study conducted by Shih et al. [35, 110], Computational Fluid Dynamics (CFD) simulations were run for assessing the combustion characteristics of fuel mixtures with varying hydrogen volumetric fractions (ranging from 0 to 90%) in a can combustor originally designed for natural gas. While a consistent combustion performance was observed for multiple scenarios, the researchers concluded that altering the combustor design weas necessary to address insufficient emissions control [35, 110].

In another investigation by Imteyaz et al. [126], a series of experiments were carried out to examine the combustion behavior of hydrogen-enriched methane fuel in a swirl-stabilised gas-turbine combustor [137]. The researchers gradually increased the hydrogen content in the blended fuel up to 80% by volume and established upper and lower air limits to maintain stable combustion.

Rajpara et al. [127] conducted both experimental and numerical studies to assess the impact of hydrogen injection on a gas turbine equipped with a swirl-stabilised combustor fueled by methane. The study revealed that higher hydrogen content led to smaller flame dimensions but increased NO_x emissions due to elevated flame temperature, along with a decrease in CO emissions [137].

Minakawa et al. [39] developed a prototype of a lean premixed swirling flame combustor for a micro gas turbine operating solely on pure hydrogen. The combustor underwent testing at atmospheric pressure and demonstrated high combustion efficiency and low NO_x emissions. Subsequently, it was installed on a micro gas turbine for evaluation under actual operating conditions. Flashbacks were observed during engine startup, a phenomenon not encountered in previous component tests [137]. By regulating the airflow to the combustor, the occurrence of flashbacks was prevented, enabling the engine to achieve self-sustaining operation. The results affirmed the superior combustion performance of the micro gas turbine, including heat release rate, combustion efficiency, and low NO_x emissions in lean conditions [39].

Cappelletti et al. [119] conducted a study to explore hydrogen combustion in a lean premix burner using both experimental and numerical simulation techniques. The experimental setup was based on an existing burner from a heavy-duty gas turbine, modified to enable variable premixing levels. The study demonstrated that to prevent flame positioning within the premix duct, high flow velocity during hydrogen combustion was necessary. The results indicated the potential for developing combustion technology utilising pure hydrogen fuel while adhering to regulated emission limits [137].

1.4. Considerations and Challenges in Operating an MGT with Hydrogen

The adaptation of a gas turbine, specifically MGTs, for the use of alternative fuels comes with several challenges. The distinct characteristics of hydrogen combustion necessitate modifications to the combustor and other system components to ensure safe and steady operation while complying with emission standards. Designing combustor technology for hydrogen combustion becomes increasingly intricate when aiming to function with both pure hydrogen and hydrogen-blended fuels [137].

The lightweight and wide flammability range of hydrogen molecules make them ideal for application in gas turbine engines. Hydrogen can combust over a wide range of air-fuel ratios, burning in a mixture with an equivalence ratio of 0.1 under lean conditions, and up to 7.1 under rich conditions, enabling varied power outputs. The inclusion of hydrogen has the potential to improve combustion efficiency and stability, as evidenced in research [48, 57, 79, 126, 134]. Studies have shown that an increase in hydrogen concentration leads to a rise in laminar burning velocity [131], which is expected to enhance flame stability and decrease the risk of lean combustion flame-out [139]. The extensive flammability limits, high flame velocities, and low ignition energy requirements of hydrogen contribute to enhanced hydrogen engine efficiency. Researchers have demonstrated that blending hydrogen with hydrocarbon fuels can enhance the ignitability and flammability of lean premixed combustors, potentially enabling stable lean burning at lower temperatures [57, 79]. Combining hydrogen with hydrocarbon fuels shows promise in improving flame stability in lean, low-temperature conditions, which could aid in reducing NO_x emissions [48, 79].

The laminar flame speed, a key indicator of burning rate, significantly influences combustion efficiency and forms the foundation of turbulent combustion. Essentially, the laminar flame speed quantifies the flame front's propagation speed relative to the unburnt mixture. Determining laminar flame speed values can serve as validation targets for chemical kinetic models or for use in turbulent combustion models [134].

Incorporating hydrogen into the fuel mixture leads to changes in the adiabatic flame temperature, increasing as the hydrogen proportion rises [124, 129]. The flame temperature elevates with the equivalence ratio (4) up to a peak point, where it achieves a balance between the heat release rate and heat transfer rate. Which occurs under slightly rich conditions ($\phi = 1.05$). Beyond this point, the adiabatic flame temperature decreases as the mixture becomes richer due to the faster decline in the specific heat value of the combustion products compared to the heat release rate. The introduction of hydrogen into a methane mixture triggers an increase in the adiabatic flame temperature [139] since hydrogen intensifies the reaction rate [132].

The generation of toxic nitrogen oxides, also referred to as thermal NO_x formation, poses a challenge in combustion processes with elevated flame temperatures. Nitrogen molecules in the air oxidise as the fuel combusts at high temperatures, resulting in the creation of NO_x. Studies indicate substantial NO_x formation around $1800\,\mathrm{K}$, with the production rate escalating significantly with further temperature elevation [23].

In gas turbines utilising hydrocarbon-based fuels, the issue of high flame temperatures is mitigated by pre-mixing the fuel with air before ignition, thereby maintaining the flame temperature below a specific threshold without compromising efficiency [30]. This strategy, known as lean premixed burners or dry low NO_x burners, nevertheless encounters various critical challenges during fuel mixing, such as combustion instabilities, flashbacks, extinction, and thermo-acoustic instabilities [101, 130].

The integration of hydrogen or hydrogen-enriched fuels in gas turbines necessitates a reconsideration of combustor design due to the substantial variations in flammability range and reaction rates between hydrogen and hydrocarbons [49]. The rapid ignition of hydrogen pre-mixing with air leads to high flame temperatures, thus fostering NO_x generation.

1.5. THETA Code

The simulations in this study are performed using the DLR in-house combustion CFD code THETA [74, 88] (**T**urbulent **H**eat Release **E**xtension of the **TA**U code). The description of the code in this study is mainly based on the works of Reichling [114].

THETA is based on a three-dimensional **F**inite-**V**olume **M**ethod (FVM) and consists of a dual grid approach, thus allowing the calculation of flows on structured, unstructured and hybrid grids [114]. THETA creates a secondary (dual) grid based on the nodes of the primary grid [114]. This dual grid builds control volumes around the vertices of the primary grid and the variables are stored in the center of the cells and thus uses a cell-centered arrangement [28] of the control volumes. Based on a domain decomposition approach, parallel computations of the flow field can be performed [114].

THETA is built around a pressure-based core solver and was initially developed for incompressible reactive flows [90]. The system of partial differential equations is transformed into algebraic systems of equations via FVM. These are then solved by matrix-free linear solvers, such as the PBCGS (**P**reconditioned **Bi**-**C**onjugate **G**radient **S**tabilised) method [29], the GMRES (**G**eneralised **M**inimal **RES**idual) scheme [21], the Multigrid method [19] and the Jacobi solution algorithm [92]. These are then stored at the grid nodes. The fluxes at the cell faces of the control volumes are determined using the midpoint rule [50]. For further details, please refer [7, 31, 50].

For computing the convective terms of the momentum and scalar equations, four different spatial discretisation schemes for the finite volume formulation of the equations are available: the upwind difference scheme (UDS) which is of first-order accuracy [50], the central difference scheme (CDS), the linear upwind difference scheme (LUDS) and quadratic upwind difference scheme (QUDS) [114]. The CDS and LUDS schemes are of second-order accuracy in space [50]. The spatial accuracy of the QUDS scheme is formally of third order accuracy. However, the midpoint rule used to determine the mass flux at the control volume interfaces, is of second-order accuracy and thus the scheme is formally decreased to an order of $O(2) < O < O(3)$ [114]. The diffusive terms are discretised by means of the second-order CDS scheme. Moreover, different temporal discretisation schemes are incorporated in THETA: the first-order accurate explicit and implicit Euler schemes (EUE and EUI), as well as the second-order accurate three points backward (TPB) and the Crank-Nicolson (CN) schemes [114].

THETA also includes a stiff chemistry solver in conjunction with several combustion models thus capable of calculating both global and detailed chemistry. It is also possible to add further modeling of the convective heat and species transport, turbulence-chemistry interactions, pollutant formation, multiphase flows, gas volume and solid surface heat radiation to the numerical simulation [114]. Additionally, various RANS, hybrid RANS-LES and pure LES turbulence models have been also implemented.

1.6. Structure of this work

The structure of this work is as follows:

Chapter 2 addresses the Fundamentals of Reactive Flows. It covers the fundamental equations, followed by turbulence, combustion modeling and discretisation.

Chapter 3 describes the structure of the Gas Turbine combustion chamber and transitions to flame stabilisation. Additionally, it discusses the relevant phenomena involved in the design of combustion chambers, including adiabatic flame temperature, flashbacks, and auto-ignition. It concludes by exploring the equations involved in pollutant formation, particularly NO_x emissions.

Chapter 4 discusses fuel variations used, with a primary focus on evaluation methods for assessing simulations. It encompasses monitoring convergence, observing values at specific monitor points, and evaluating flow fields. It also covers evaluations using chemiluminescence and heating value.

Chapter 5 delves deeper into the simulation process and the creation of a suitable computational domain. It mentions information about a grid independence study as well. Additionally, it briefly discusses post-processing.

Chapter 6 addresses the verification and validation of the created numerical setup. This chapter also includes a discussion of the results.

Chapter 7 concludes this work with a summary and final conclusions.

2. Fundamentals of Reactive Flows

This section deals with the theoretical basics of a CFD simulation. Initially, the Navier-Stokes equations are discussed. As the scope of this project revolves around incompressible flows, main considerations and assumptions pertaining to the incompressible flow are laid out. The equations are then followed by a section which briefly discusses various turbulence modelling approaches available followed by detailed explanation of turbulence and combustion models of interest. Finally, the section also touches upon the discretisation methods.

2.1. Fundamental Equations

To describe compressible reactive flows, a system of coupled partial differential equations can be established. These are known as the Navier-Stokes equations, comprising balance equations for mass, momentum, and energy of the fluid in enthalpy form. Additionally, transport equations for the respective species mass fractions Y_α need to be solved. The number of transport equations for a fluid is determined by the number of species in the fluid. From a total of N_s species in a fluid, $N_s - 1$ transport equations result. The conservation equations in conservative form are expressed as:

$$\frac{\partial \rho}{\partial t} + \nabla \cdot (\rho \boldsymbol{u}) = 0, \tag{2.1}$$

$$\frac{\partial (\rho \boldsymbol{u})}{\partial t} + \nabla \cdot [(\rho \boldsymbol{u}) \otimes \boldsymbol{u}] + \nabla p = \nabla \cdot \underline{\underline{\boldsymbol{\tau}}} + \rho \boldsymbol{f}, \tag{2.2}$$

$$\frac{\partial (\rho h)}{\partial t} + \nabla \cdot (\rho \boldsymbol{u} h) - \frac{\partial p}{\partial t} - \boldsymbol{u} \cdot \nabla p = \nabla \cdot (\lambda \nabla T) + \underline{\underline{\boldsymbol{\tau}}} : \nabla \boldsymbol{u} + \rho \boldsymbol{u} \cdot \boldsymbol{f}, \tag{2.3}$$

$$\frac{\partial (\rho \boldsymbol{Y_\alpha})}{\partial t} + \nabla \cdot [(\rho \boldsymbol{u}) \otimes \boldsymbol{Y_\alpha}] = -\nabla \cdot \underline{\underline{\boldsymbol{j}}} + \boldsymbol{S_\alpha}. \tag{2.4}$$

The variable $\underline{\underline{\boldsymbol{\tau}}}$ characterises the stress tensor, which is defined by the following formula [45, 64]:

$$\underline{\underline{\boldsymbol{\tau}}} \equiv 2\mu \left[\underline{\underline{\boldsymbol{S}}} - \frac{1}{3} (\nabla \cdot \boldsymbol{u}) \underline{\underline{\boldsymbol{I}}} \right] \text{ with } \underline{\underline{\boldsymbol{S}}} \equiv \frac{1}{2} \left[\nabla \boldsymbol{u} + (\nabla \boldsymbol{u})^T \right]. \tag{2.5}$$

where $\underline{\underline{\boldsymbol{S}}}$ denotes the strain rate tensor. The variable μ describes the dynamic viscosity and is obtained using a weighted mean of the pure species viscosity values [74].

Also, λ represents the thermal conductivity, T is the temperature, and the term $\underline{\underline{\boldsymbol{\tau}}} : \nabla \boldsymbol{u}$ describes the volumetric work per unit time. It is the Frobenius scalar product of the matrices $\underline{\underline{\boldsymbol{\tau}}}$ and $\nabla \boldsymbol{u}$, resulting in a scalar term [118]. Applying the divergence operator $\nabla \cdot (...)$ to a dyadic product of two vectors (a matrix), represented by the operator $\otimes$, yields a column vector. Thus, for the two convective terms $\nabla \cdot [(\rho \boldsymbol{u}) \otimes \boldsymbol{u}]$ and $\nabla \cdot [(\rho \boldsymbol{u}) \otimes \boldsymbol{Y_\alpha}]$, and the stress tensor $\nabla \cdot \underline{\underline{\boldsymbol{\tau}}}$, a column vector is obtained for each.

The diffusion mass flux can be described according to Fick's law against the concentration gradient by the approach

$$\underline{\underline{\boldsymbol{j}}} = -\underline{\underline{\boldsymbol{D}}} \cdot \nabla \boldsymbol{Y_\alpha} \tag{2.6}$$

where $\underline{\underline{\boldsymbol{D}}}$ stands for the diffusion coefficients [97].

Since all equations are applied to a 3-dimensional computational domain, the balance Equation (2.2) has the dimension $\dim = 3$. The dimension of the transport equation for the species mass fractions (2.4) arises from the number of species N_s. The vector $\boldsymbol{Y}$ includes for $\alpha = 1, 2, \ldots, N_s - 1$ species the entries of the mass fractions Y_α [80, 114, 123]. Additionally, for the sum of mass fractions, the relationship

$$\sum_{\alpha=1}^{N_s} Y_\alpha = 1 \tag{2.7}$$

holds.

The above equations include the flow quantities pressure p, density ρ, enthalpy h, and velocity $\boldsymbol{u}$. The consumption or production of a respective species α, through a chemical reaction, is described in Equation (2.4) by the chemical source term $\boldsymbol{S_\alpha}$ [56]. If the fluid used is a chemically-reactive ideal gas, the pressure p and density ρ are related to each other via the thermal equation of state. Based on the ideal gas law, the density can be calculated depending on the pressure, temperature, and the specific gas constant of the mixture R as

$$\rho = \frac{p_{\text{abs}}}{RT}. \tag{2.8}$$

where p_{abs} is the absolute pressure, which is composed of the ambient pressure p and the reference pressure p_{ref}. The specific gas constant can be expressed via the universal gas constant R_m, the mass fractions of the species Y_α, and their molar masses M_α.

Thus, for the density, we have

$$\rho = \frac{p_{\text{ref}} + p}{RT} \text{ with } R \equiv R_m \sum_{i=1}^{N_s} \frac{Y_\alpha}{M_\alpha}. \tag{2.9}$$

Considering the flowing fluid as incompressible, the density is independent of hydrodynamic pressure changes in the flow field and is merely a function of the mean thermodynamic pressure [20, 56, 62, 64]. From this, it follows that the dissipation term $\underline{\underline{\boldsymbol{\tau}}} : \nabla \boldsymbol{u}$ and the pressure fluctuation term $Dp/Dt = \partial p/\partial t + \boldsymbol{u} \cdot \nabla p$ in Equation (2.3) can be neglected [114]. Under the assumption of an ideal gas, the enthalpy h balanced in Equation (2.3) consists of thermal enthalpy and formation enthalpy, given by

$$h = \int_{T_0}^{T} c_p \, dT + \sum_{\alpha=1}^{N_s} \Delta h_{f,\alpha}^{0} Y_\alpha. \tag{2.10}$$

and thus depends on the contributions of individual gas components [56, 117].

The vector $\boldsymbol{f}$ on the right side of the momentum and energy equations accounts for body forces such as gravitational force. Since only minor height differences are considered in gas turbines and the influence of the gravitational force is negligible compared to pressure gradients or convection, body forces can be disregarded [97].

2.1.1. Spatial and Temporal Scales in Turbulence

The energy cascade theory of turbulence, proposed by Richardson [71], is widely used to analyse the magnitude of turbulent flow. According to the energy cascade theory, in a homogeneous and isotropic turbulence, the large-scale eddies obtain energy from the mean flow through vortex stretching [72]. Subsequently, these large eddies, also known as integral scale eddies (l_t), cascade down to smaller eddies called Kolmogorov eddies (l_η). In the Kolmogorov regime, molecular diffusion begins to play a crucial role as the scales can be estimated based on both molecular diffusion and the turbulent dissipation rate (ε). Here, ε is defined as the rate at which viscosity converts turbulent kinetic energy (TKE) into thermal energy. According to the Kolmogorov hypothesis, the energy dissipation rate remains constant until it reaches the minimum Kolmogorov size [24]. Figure 2.3 demonstrates that larger eddies tend to possess higher energy, which they transfer to successively smaller eddies.

Through scaling analysis, various length and time scales, along with non-dimensional numbers, are summarised ahead. Firstly, the integral scales are discussed in detail. The integral length scale (l_t) is estimated by integrating the velocity autocorrelation function f, as defined in Equation (2.11). The velocity scale is obtained based on the definition of turbulent kinetic energy (TKE) per unit mass (Equation (2.12)). The time scale is derived by scaling l_t with the fluctuating velocity (u'), as defined in Equation (2.13). Additionally, the Reynolds number specific to the integral length scale is mentioned in Equation (2.14).

$$\text{Length:} \quad l_t = \int_0^\infty f \, dr \tag{2.11}$$

$$\text{Velocity:} \quad u' = \sqrt{2k} \tag{2.12}$$

$$\text{Time:} \quad t_f = \frac{l_t}{u'} \tag{2.13}$$

$$\text{Non-dimensional:} \quad Re_{l_t} = \frac{u' l_t}{\nu} \tag{2.14}$$

Next, the scales in the Kolmogorov range are considered. Due to the significant diffusive and dissipative nature of turbulent flows, scales in the Kolmogorov range are developed based on the dimensions of diffusion $\left(L^2/T\right)$ and dissipation $\left(L^2/T^3\right)$. Using these dimensions, length, velocity, and time scales (equations (2.15), (2.16), and (2.17)) are constructed. Similar to the integral scale, a specific Reynolds number is defined for the Kolmogorov scale in Equation (2.18). This Reynolds number is equal to unity since both the inertial and viscous terms are equal in the Kolmogorov scale [75].

$$\text{Length:} \quad l_\eta = \left(\frac{\nu^3}{\varepsilon}\right)^{1/4} \tag{2.15}$$

$$\text{Velocity:} \quad u'_\eta = (\nu\varepsilon)^{1/4} \tag{2.16}$$

$$\text{Time:} \quad t_\eta = \left(\frac{\nu}{\varepsilon}\right)^{1/2} \tag{2.17}$$

$$\text{Non-dimensional:} \quad Re_\eta = \frac{u'_\eta l_\eta}{\nu} = 1 \tag{2.18}$$

2.2. Turbulence Modeling

Flows of any kind can be roughly divided into laminar and turbulent flows based on the Reynolds number. The Reynolds number Re describes the ratio of inertial to viscous forces or the ratio of specific momentum convection to momentum diffusion. It is defined as:

$$Re = \frac{u \cdot L}{\nu} \tag{2.19}$$

where u is the characteristic velocity, L is the characteristic length, and ν is the kinematic viscosity.

The transition point from laminar to turbulent flow is determined by the critical Reynolds number, which is about $\mathrm{Re}_{\mathrm{crit}} \approx 2300$ for flow in straight pipes [113]. Figure 2.1a showcases a laminar current while Figure 2.1b shows a turbulent flow [98].

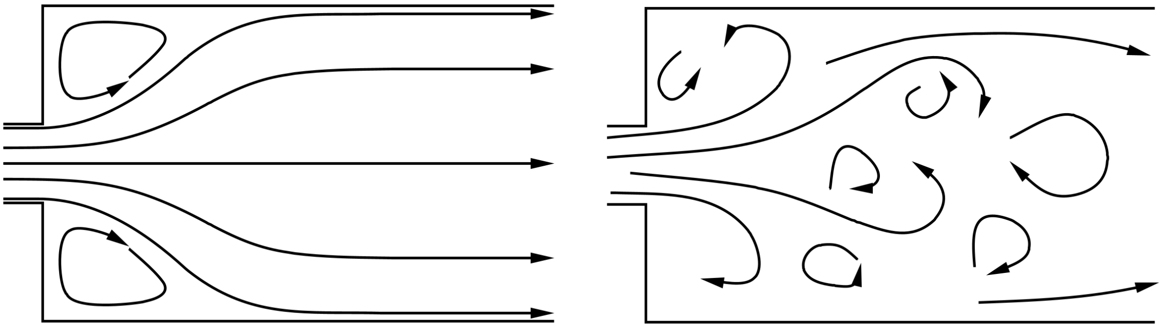

(a) Laminar flow

(b) Turbulent flow

Figure 2.1.: Comparison of laminar and turbulent flows in a pipe with cross-sectional expansion [98]

Turbulent flow is characterised by random, chaotically distributed velocity fluctuations superimposed on the main flow of the fluid. The cause of these fluctuations is the formation of vortices of varying length and time scales. The occurrence of high velocity gradients leads to the formation of large, turbulent vortices that extract kinetic energy from the main flow. The largest vortex structures interact with and extract kinetic energy from the main flow, breaking down into smaller vortices. Kinetic energy is transported from large vortices through so-called energy cascades across the entire vortex spectrum. Due to the rapid decline of energy in a cascade process, the smallest vortices possess the lowest kinetic energy until it is dissipated and converted into internal thermal energy (to overcome the viscous stress of the fluid). This dissipation leads to an increased energy loss associated with turbulent flow [72].

Direct **N**umerical **S**imulation (DNS) is the most accurate method to solve the transport equations (2.1) - (2.3) without statistical averaging and thereby calculate turbulent flow. However, it places the highest demands on the numerical method and computational power, as the smallest turbulent scales must be resolved both spatially and temporally [93]. The CPU requirements for this, however, exceed the computational capacities available today.

As a result, averaging methods are applied to the Navier-Stokes equations to filter out and model parts of the turbulent spectrum.

The most widely used is the **R**eynolds **A**veraged **N**avier-**S**tokes (RANS) method, where the conservation equations from Section 2.1 are subjected to statistical averaging. This results in the vortex structures from turbulence no longer being resolved in time and space, leading to a significant reduction in computation time and memory requirements. It allows for the numerical simulation of technically relevant flow cases with high Reynolds numbers. The turbulence model estimates the velocity and length scales of the large, energy-carrying turbulence elements, which are represented by dashed lines in Figure 2.2 [98].

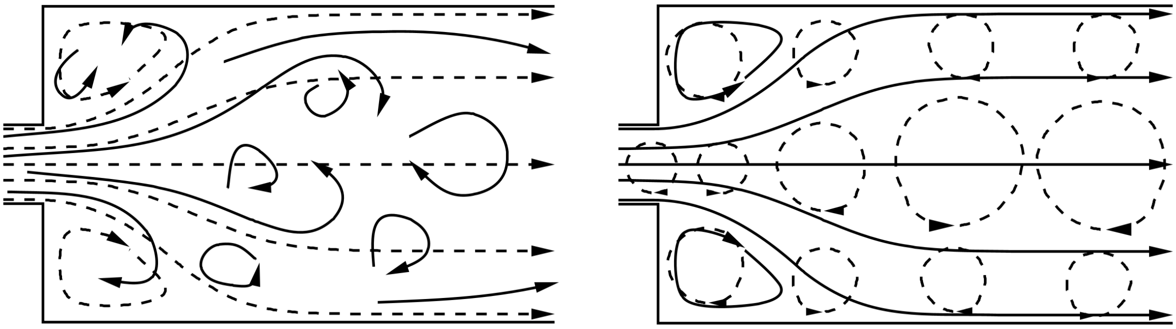

(a) Original flow

(b) Reynolds-averaged flow

Figure 2.2.: Comparison of the original and Reynolds-averaged flow in a pipe with cross-sectional expansion [98]

The basis of the RANS method is the Reynolds decomposition [38], where a flow quantity is divided into a mean value and a fluctuation [103]. This leads to the derived RANS equations, in which the fluctuation is no longer explicitly described:

$$\frac{\partial\bar{\rho}}{\partial t} + \nabla\cdot(\bar{\rho}\tilde{\boldsymbol{u}}) = 0, \tag{2.20}$$

$$\frac{\partial(\bar{\rho}\tilde{\boldsymbol{u}})}{\partial t} + \nabla\cdot[\bar{\rho}(\tilde{\boldsymbol{u}}\otimes\tilde{\boldsymbol{u}})] + \nabla\bar{p} = \nabla\cdot[\underline{\underline{\boldsymbol{\tau}}} - \bar{\rho}(\widetilde{\boldsymbol{u}''\otimes\boldsymbol{u}''})], \tag{2.21}$$

$$\frac{\partial(\bar{\rho}\tilde{h})}{\partial t} + \nabla\cdot(\bar{\rho}\tilde{\boldsymbol{u}}\tilde{h}) - \frac{Dp}{Dt} = \nabla\cdot\left[\frac{\lambda}{c_p}\nabla\tilde{h} + \bar{\rho}\widetilde{\boldsymbol{u}''h''}\right] + \overline{\underline{\underline{\boldsymbol{\tau}}} : \nabla\boldsymbol{u}}, \tag{2.22}$$

$$\frac{\partial(\bar{\rho}\widetilde{Y_\alpha})}{\partial t} + \nabla\cdot[\bar{\rho}(\tilde{\boldsymbol{u}}\otimes\widetilde{Y_\alpha})] = \nabla\cdot[\underline{\underline{\boldsymbol{D}}}\cdot\nabla\widetilde{Y_\alpha} + \bar{\rho}(\widetilde{\boldsymbol{u}''\otimes Y_\alpha''})] + \overline{S_\alpha}. \tag{2.23}$$

In Equation (2.22), the heat flux is transformed according to Fourier's law to:

$$\lambda\nabla T = \frac{\lambda}{c_p}h. \tag{2.24}$$

The flow quantities in the equations (2.20) to (2.23) are divided into Reynolds-averaged quantities (denoted by $\overline{(...)}$) and Favre-averaged quantities (denoted by $\widetilde{(...)}$). The respective fluctuation quantities are represented by $(...)''$ [120].

The averaging process [56] leads to unclosed terms, which must be modeled by appropriate turbulence models. This averaging also involves a loss of information. The unclosed terms include the chemical source term $\overline{S_\alpha}$, the component fluxes $\widetilde{\boldsymbol{u}''\otimes Y_\alpha''}$, the enthalpy fluxes $\bar{\rho}\widetilde{\boldsymbol{u}''h''}$ and the Reynolds stresses $\widetilde{\boldsymbol{u}''\otimes\boldsymbol{u}''}$.

Using the gradient diffusion hypothesis, both the Reynolds energy flux and the component flux can be transformed as follows [5, 63]:

$$\bar{\rho}\widetilde{\boldsymbol{u}''h''} \approx -\frac{\mu_t}{P_{rt}}\nabla\tilde{h} \quad \text{and} \quad \bar{\rho}(\widetilde{\boldsymbol{u}''\otimes Y''_\alpha}) \approx -\frac{\mu_t}{S_{ct}}\nabla\widetilde{Y}_\alpha. \tag{2.25}$$

Here, μ_t denotes the turbulent viscosity, $Pr_t = (\mu_t c_p)/\lambda_t$ the turbulent Prandtl number, and $Sc_t = \mu_t/(\bar{\rho}D_t)$ the turbulent Schmidt number. The ratio of Schmidt to Prandtl number is known as the Lewis Number $Le_t = \lambda_t/(c_p\bar{\rho}D_t)$. λ_t represents the turbulent thermal conductivity, and D_t is the turbulence-induced diffusion coefficient [120].

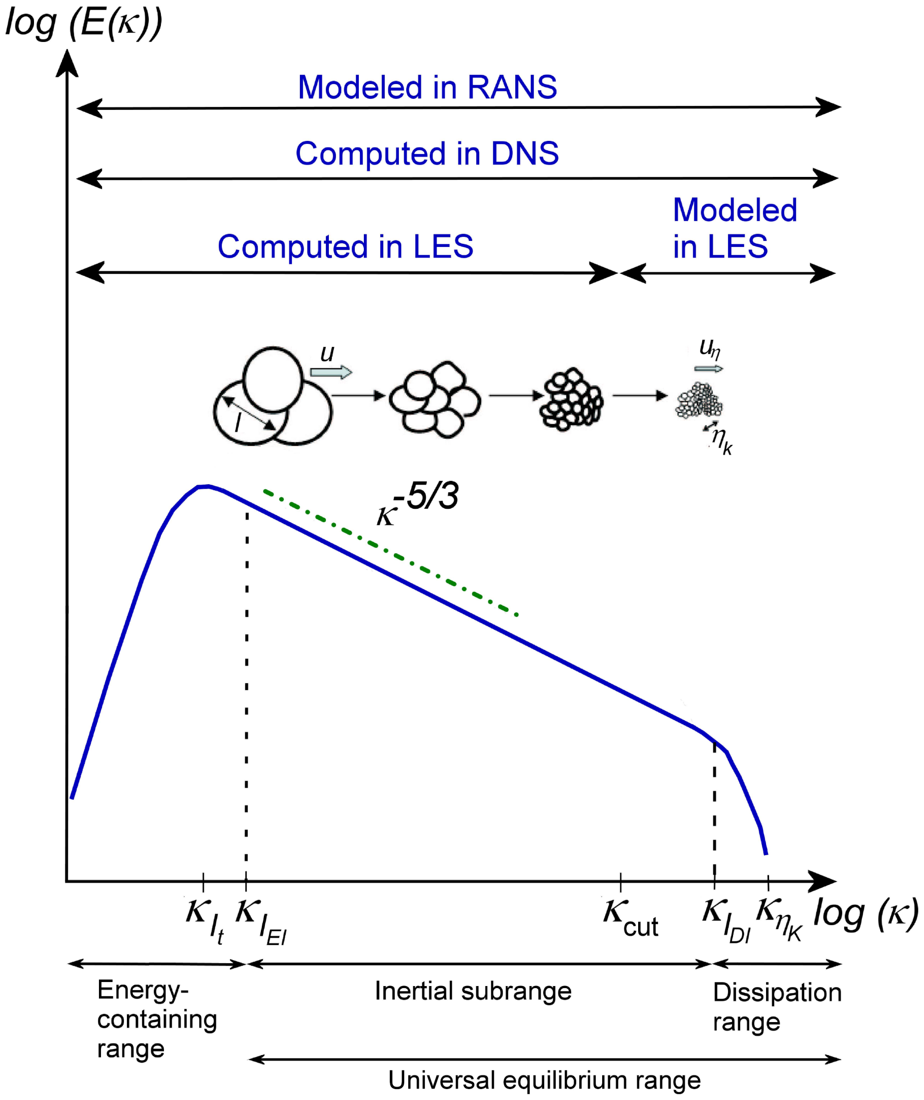

Figure 2.3.: Turbulent kinetic energy spectrum vs. Wave number and the level of computed and modeled scales in RANS, DNS, and LES. Adapted from [66, 99].

The Reynolds stresses in RANS models are closed using the linear eddy viscosity hypothesis of Boussinesq [1]. The basis of this approach is the assumption that a turbulent flow exists and the Reynolds stresses are proportional to the velocity gradients of the mean main flow. This leads to the following expression for the

Reynolds stresses:

$$-\bar{\rho}(\widetilde{\boldsymbol{u}'' \otimes \boldsymbol{u}''}) \approx \mu_t \left[\nabla\tilde{\boldsymbol{u}} + (\nabla\tilde{\boldsymbol{u}})^T - \frac{2}{3}(\nabla\cdot\tilde{\boldsymbol{u}})\boldsymbol{I}\right] - \frac{2}{3}\bar{\rho}k \tag{2.26}$$

where $k = \frac{1}{2} \cdot (\widetilde{\mathbf{u}'' \cdot \mathbf{u}''})$ represents the turbulent kinetic energy and $\boldsymbol{I}$ is the identity matrix [97]. The modeling of Reynolds stresses in RANS models is thus reduced to the calculation of the turbulent viscosity. Unlike molecular viscosity μ, turbulent viscosity is not a material property but a function of the turbulence. A variety of models for determining turbulent viscosity are proposed in the literature [117]. The approaches used in this work for turbulence description are explained in the following sections 2.2.1 and 2.2.2.

To calculate unsteady flows, **U**nsteady **R**eynolds **A**veraged **N**avier-**S**tokes (URANS) simulations are often used. The turbulence models derived for steady-state RANS conditions are applied to the averaged, unsteady conservation quantities. However, this approach can only resolve flow fluctuations within the range of integral length and time scales [86].

In the approach known as **L**arge **E**ddy **S**imulation (LES), only the large and energy-carrying vortices are directly resolved. The influence of smaller, anisotropic scales (fine vortex structures), whose spatial extent is less than the spatial resolution of the computational grid, is modeled. This requires a decomposition of the turbulent flow field into fine and coarse structures. LES thus resolves all turbulence elements that are larger than a chosen spatial filter width. This filtering is graphically represented in Fig. 2.2. Due to the finer temporal and spatial discretisation and the fact that only the effect of the filtered out, smaller turbulence elements on the resolved flow is approximated, the computational effort of LES increases significantly compared to RANS simulations [98, 112].

Figure 2.3 provides an overview of the resolution degree of turbulent structures in the mentioned methods. Since this study is conducted using two-equation RANS models, they have been discussed as follows.

2.2.1. The $k-\varepsilon$ Turbulence Model

All k-ε models are two-equation models, which are frequently used in industrial flow simulations. These models solve two transport equations and model the Reynolds stresses through the linear eddy viscosity approach of Boussinesq, as mentioned in Section 2.2 [53]. Their robustness, cost-effectiveness, and reasonable accuracy explain the frequent use of these models in industrial flow and heat transfer simulations. However, some k-ε models have limitations, such as insensitivity to adverse pressure gradients and boundary layer separation. They often calculate a delayed and reduced separation compared to visual experiments [72].

The Standard k-ε Model

For turbulent flows with high Reynolds numbers, the k-ε model established by Launder and Spalding [9] remains one of the most used turbulence models in CFD simulations, often referred to as the Standard k-ε Model. The theoretical descriptions of the following k-ε models are based on the works of Schwarze [98] and Kunz [53], with detailed descriptions available in the references by Launder et al. [9, 11].

The turbulent stresses are attributed to gradients in the main flow. The production P_k and diffusion D_k of turbulent kinetic energy, due to velocity gradients in the flow, are approximated in the transport equations for turbulent kinetic energy k as follows:

$$P_k = \mu_t \nabla\boldsymbol{u} \cdot [\nabla\boldsymbol{u} + (\nabla\boldsymbol{u})^T] \tag{2.27}$$

$$D_k = \nabla \cdot \left(\mu \nabla k + \frac{\mu_t}{\sigma_k} \nabla k \right) = \nabla \cdot \left[\left(\mu + \frac{\mu_t}{\sigma_k} \right) \nabla k \right] \tag{2.28}$$

Using the turbulent kinetic energy k and dissipation rate ε, the velocity scale U_t and time scale L_t (characteristic scales of turbulence) can be estimated as

$$U_t = \sqrt{k} \quad \text{and} \quad L_t = \frac{k^{1.5}}{\varepsilon} \tag{2.29}$$

The transport equations for the turbulent kinetic energy k and the turbulent dissipation rate ε are as follows:

$$\frac{\partial(\bar{\rho} k)}{\partial t} + \nabla(\bar{\rho} \boldsymbol{u} k) - \nabla \cdot \left[\left(\mu + \frac{\mu_t}{\sigma_k} \right) \nabla k \right] = \tilde{P}_k - \bar{\rho} \varepsilon \tag{2.30}$$

$$\frac{\partial(\bar{\rho} \varepsilon)}{\partial t} + \nabla(\bar{\rho} \boldsymbol{u} \varepsilon) - \nabla \cdot \left[\left(\mu + \frac{\mu_t}{\sigma_\varepsilon} \right) \nabla \varepsilon \right] = C_1 \tilde{P}_k \frac{\varepsilon}{k} - C_2 \bar{\rho} \frac{\varepsilon^2}{k} \tag{2.31}$$

The modeling in Equation (2.31) is based on the assumption that the production and decay of ε are proportional to their respective terms in Equation 2.30. The proportional factors in Equation 2.31 are the terms $C_1 \tilde{P}_k \varepsilon / k$ and $C_2 \bar{\rho} \varepsilon^2 / k$. In this case, the turbulent viscosity is calculated as $\mu_t = C_\mu \bar{\rho} k^2 / \varepsilon$, where it is simplistically treated as a scalar. The transport equations contain constants, which for the Standard k-ε model are usually proposed as shown in Table 2.1 [6, 10].These values have been adapted for a wide range of flow conditions and are based on the analysis of canonical flows using the Standard k-ε Model. Canonical flows refer to simplified flow configurations such as boundary layer or free jet flows. In combination, these can represent key properties of complex flows [98].

Table 2.1.: Constants of the Standard k-ε Model.

C_μ	σ_k	σ_ε	C_1	C_2
0.09	1.0	1.3	1.44	1.92

The model is well-suited for the calculation of flows, such as fully turbulent pipe flow, and is often used to analyse flow processes where the global flow structures are to be determined. However, in complex flows or near-wall regions, where fully developed turbulence cannot be assumed, the model sometimes yields poor quantitative and qualitative results [98]. To compensate for this disadvantage, special models, such as Low-Reynolds or wall functions, are used. As THETA Solver does not natively support RNG k-ε and Realizable k-ε models, please refer to Appendix A.1 for their detailed descriptions.

2.2.2. The $k - \omega$ Turbulence Model

In addition to the various k-ε models, turbulence models that incorporate the characteristic turbulent frequency ω of the energy-carrying vortices are increasingly used. The turbulent frequency is defined as

$$\omega = \frac{\varepsilon}{k} \left(= \frac{U_t}{L_t}\right) \tag{2.32}$$

The Standard k-ω Model by Wilcox [25] is a two-equation turbulence model that also relies on the eddy viscosity principle. The foundation of these eddy viscosity models is the assumption that turbulence results in an increase in viscosity. The laminar and turbulent viscosities are added together, thereby affecting the flow.

The k-ω model is defined by a transport equation for the turbulent kinetic energy k and for the turbulent frequency ω [97]:

$$\frac{\partial(\bar{\rho}k)}{\partial t} + \nabla(\bar{\rho}\boldsymbol{u}k) - \nabla \cdot \left[\left(\mu + \sigma^* \frac{k}{\omega}\right)\nabla k\right] = \tilde{P}_k - \beta^* \bar{\rho}\omega, \tag{2.33}$$

$$\frac{\partial(\bar{\rho}\omega)}{\partial t} + \nabla(\bar{\rho}\boldsymbol{u}\omega) - \nabla \cdot \left[\left(\mu + \sigma \frac{k}{\omega}\right)\nabla \omega\right] = \tilde{P}_k \frac{\alpha}{\nu_t} - \beta \bar{\rho}\omega^2. \tag{2.34}$$

The turbulent kinematic viscosity is calculated as $\nu_t = k/\omega$. For the excitation term $\tilde{P}_k$ on the right side of equations (2.33) and (2.34), we have:

$$\tilde{P}_k = \min\left(\mu_t \nabla \boldsymbol{u} \cdot [\nabla \boldsymbol{u} + (\nabla \boldsymbol{u})^T], 10 \cdot \beta^* \bar{\rho} k \omega\right) \tag{2.35}$$

$\tilde{P}_k$ is understood as a limiter to restrict the production of turbulence in stagnation areas [105]. The remaining constants are listed in Table 2.2.

Table 2.2.: Constants of the Standard k-ω Model [25].

$\boldsymbol{\alpha}$	$\boldsymbol{\beta}$	$\boldsymbol{\beta^*}$	$\boldsymbol{\sigma}$	$\boldsymbol{\sigma^*}$
5/9	3/40	0.09	0.5	0.5

This model provides a much better description of the mean turbulence and thus the overall mean flow field in the near-wall region compared to the Standard k-ε Model. However, in free outer flows and shear layers, the turbulence and flow modeling perform significantly poorer [69, 98].

The k-ω SST Model

The Shear-Stress-Transport (SST) Model, developed by Menter [33], is based on the k-ω Model by Wilcox and combines the advantages of both the k-ε and k-ω models [55]. The k-ω SST Model employs a hybrid approach with two different model equations for ω. Near the wall, the k-ω Model is used to calculate the mean turbulence and flow quantities. In the free field, blending functions transition to the k-ε Model. The theoretical description of the k-ω SST Model is based on the works of Reichling [114] and Grimm [120]. The transport equations for k and ω in this model are as follows:

$$\frac{\partial(\bar{\rho}k)}{\partial t} + \nabla(\bar{\rho}\boldsymbol{u}k) - \nabla \cdot [(\mu + \sigma_k \mu_t)\nabla k] = \tilde{P}_k - \beta^* \bar{\rho}\omega, \tag{2.36}$$

$$\frac{\partial(\bar{\rho}\omega)}{\partial t} + \nabla(\bar{\rho}\boldsymbol{u}\omega) - \nabla \cdot [(\mu + \sigma_\omega \mu_t)\nabla \omega] = \tilde{P}_k \frac{\alpha}{\nu_t} - \beta \bar{\rho}\omega^2 + 2(1 - F_1)\frac{\bar{\rho}\sigma_{\omega 2}}{\omega}(\nabla k \nabla \omega). \tag{2.37}$$

The blending function F_1 is defined as:

$$F_1 = \tanh\left\{\left\{\min\left[\max\left(\frac{k}{\beta^* \omega y}, \frac{500\nu}{y^2 \omega}\right), \frac{4\bar{\rho}\sigma_{\omega 2} k}{CD_{k\omega} y^2}\right]\right\}^4\right\}. \tag{2.38}$$

where y is the distance to the wall, ν is the kinematic viscosity, and $CD_{k\omega}$ is the cross-diffusion term, defined as:

$$CD_{k\omega} = \max\left(2\bar{\rho}\sigma_{\omega 2}\frac{1}{\omega}(\nabla k \nabla \omega), 10^{-10}\right) \tag{2.39}$$

In the far-field, the blending function F_1 from Equation (2.38) approaches zero and takes the value of one within the boundary layer. The turbulent kinematic viscosity in this model is calculated as:

$$\nu_t = \frac{a_1 k}{\max(a_1 \omega, F_2 \sqrt{2S_{ij}} \cdot S_{ij})} \tag{2.40}$$

The excitation term $\tilde{P}_k$ was already introduced and defined in Section 2.2.2, and the shear rate S_{ij} earlier in Section 2.2.1. F_2 in Equation (2.40) is another blending function, defined as:

$$F_2 = \tanh \left\{ \left[\max \left(\frac{2\sqrt{k}}{\beta^* \omega y}, \frac{500\nu}{y^2 \omega} \right) \right]^2 \right\}. \tag{2.41}$$

If we consider ν as a vector comprising the entries α, β, and σ, the constants without subscript can be expressed through the blending functions as:

$$\nu = F_1 \nu_1 - (1 - F_1)\nu_2 \quad \text{with} \quad \nu = [\alpha\ \beta\ \sigma]^T \tag{2.42}$$

The constants for the k-ω SST Model are presented in Table 2.3.

Table 2.3.: Constants of the k-ω SST Model [114].

a_1	α_1	α_2	β_1	β_2	β^*	σ_{k1}	σ_{k2}	$\sigma_{\omega 1}$	$\sigma_{\omega 2}$
0.31	$0.\bar{5}$	0.44	0.075	0.828	0.09	0.85	1	0.5	0.856

Within the flow field, ω generally takes small values, which, however, increase drastically in the very near-wall area. This implies that the k-ω SST Model requires a correspondingly fine wall resolution in the boundary layer, becoming especially relevant in specific applications where flow separation occurs.

By combining the k-ω and k-ε models, the k-ω SST Model leverages the advantages of both models and can even compensate for the respective disadvantages of each model [98].

2.3. Turbulent Premixed Combustion

Turbulent phenomena are leveraged in combustion to improve reactivity, mixing and efficiency. The laminar flame structure get replaced by turbulent regimes when the flame encounters a turbulent flow. Loads of chemical reactions occurring within the flow results in a wide range of temporal scales, spanning from nanoseconds to seconds, in addition to turbulence's temporal and spatial scales [102].

Borghi and Peters have classified turbulent flame regimes based on non-dimensional numbers obtained through scaling analysis [17, 47]. The flow scales are defined in Section 2.1.1 and chemical time scales used for the scaling analysis are defined further in this section. As the identification of an appropriate regime is crucial for modeling the reaction process, diagrams are constructed under few assumptions. Following assumptions are made: isotropic turbulence, adiabatic conditions, unit Lewis and Schmidt number and concept relies on the size of eddies and flame thickness (δ_f). Eddies larger than δ_f cannot penetrate the flame and instead stretch and wrinkle it. This concept, also known as the flamelet concept, models the turbulent flame as a collection of stretched laminar flamelets with a local flame speed S_L^0. On the contrary, eddies smaller than the flame thickness will penetrate the reaction zone, thereby distorting the flame as well as the timescale [138]. This is also identified as the non-flamelet region. The line between these regions is based on the criterion proposed by Klimov and Williams [13].

The interaction between the flame front and turbulence is represented by Damköhler number (Da) and Karlovitz number (Ka). Da number is defined as the ratio of turbulent integral time scale to chemical time scale [138]. A second Damköhler number (Da_η) is also defined similarly based on Kolmogorov time scale. The Karlovitz number is simply the reciprocal of Da_η as seen in the equations below:

$$\text{Length:} \quad \delta_f = \frac{\nu}{S_L^0} \tag{2.43}$$

$$\text{Velocity:} \quad S_L^0 \tag{2.44}$$

$$\text{Time:} \quad t_{chemical} = \frac{\nu}{S_L^0} \tag{2.45}$$

$$\text{Non-dimensional:} \quad Da_{l_t} = \frac{t_f}{t_c}; \quad Da_{l_\eta} = \frac{t_\eta}{t_f} = \frac{1}{Ka} \tag{2.46}$$

$$\frac{t_{l_t}}{t_\eta} = {Re_{l_\eta}}^{1/2} = DaKa; \quad Ka = \left(\frac{\delta_f}{l_\eta}\right)^2; \quad Re_t/Da_t = \left(\frac{u'}{S_L^0}\right)^2; \quad Re_t Da_t = \left(\frac{l_t}{\delta_f}\right)^2$$

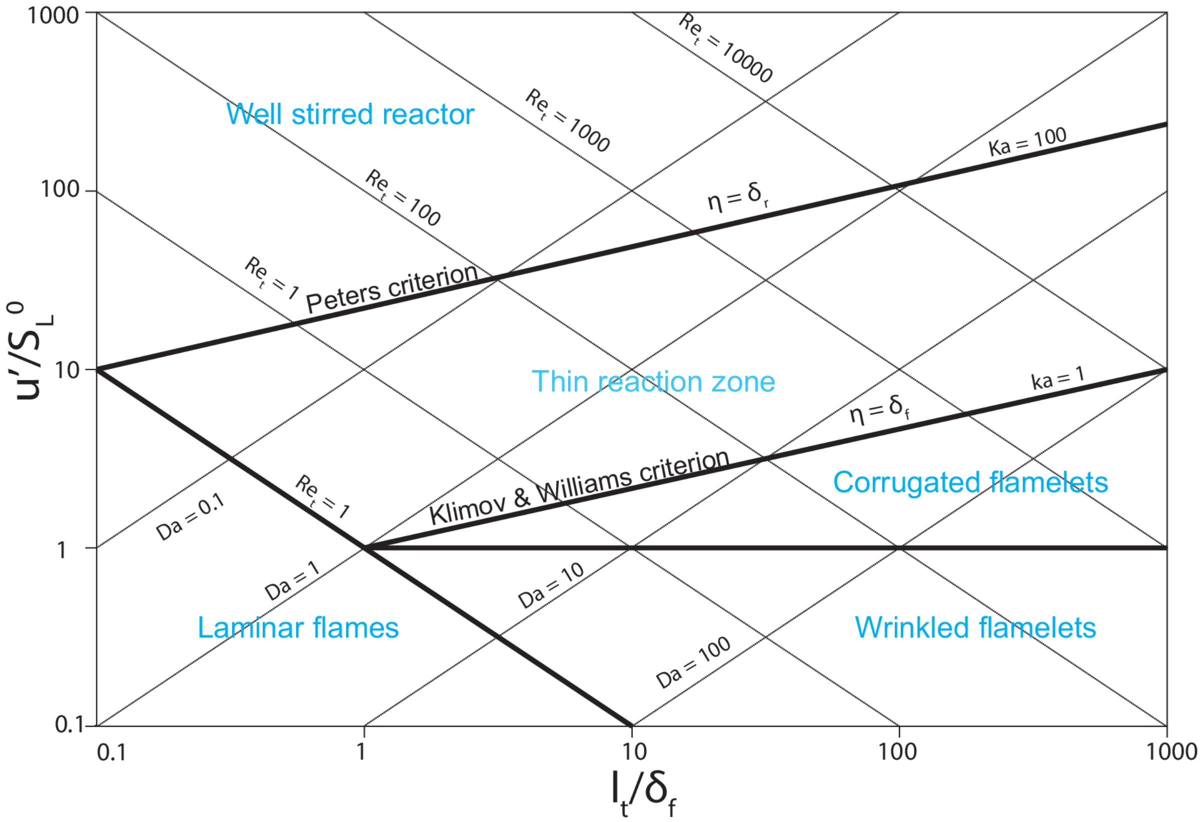

Figure 2.4.: Borghi's and Peter's combustion regime diagram, adapted from [17, 61, 138].

Later, Peters postulated that, the eddies will enter into the preheat zone and expand it, even if they are smaller than δ_f [47]. Based on the same hypothesis, a different regime where the broad preheat zone exists is known as the thin reaction zone. The boundary separating a well-stirred reactor and thin reaction zone is known as Peters criterion $Ka_{\delta_r} = 1$, this also corresponds to $Ka = 100$. Ka_{δ_r} is defined as the ratio of reaction zone thickness to the Kolmogorov length scale [138]. The Borghi-Peters diagram is used to characterize different combustion regimes as depicted in Figure 2.4.

Combustion regimes of turbulent premixed combustion are summarised as follows [138]:

- **For $Ka < 1$ (Flamelets):**
  - Flame thickness is smaller than turbulent eddies, and they can't penetrate into the flame. This flamelet region is further divided into:
    - Wrinkled flamelets ($u' \approx S_L^0$)
    - Corrugated flamelets ($u' > S_L^0$)
- **For $Ka > 1$ (Thin reaction zones):**
  - Small-scale turbulent eddies penetrate into the preheat zone and enlarge the flame thickness.
- **For $Ka > 100$ (Broken reaction zones):**
  - Reaction is the rate-limiting step since turbulence is much faster than reaction. Turbulence mixes like a well-stirred reactor.

2.4. Combustion Modeling

Combustion is generally understood as the rapid, self-sustaining oxidation of fuels. This process is characterised by the release of heat, light, and volatile substances, and is referred to as an exothermic reaction. The flame is the area where the majority of the chemical transformation takes place, while the narrow zone between the reactants and products is known as the flame front. The state of the fuel and oxidiser mixture upon entering the combustion chamber can vary, with a distinction between a homogeneous premixed state, a separate state, or immediate mixing before the chemical reaction [65]. If the combustion completely converts both fuel and oxidiser into reaction products, the mixture is considered stoichiometric. To accurately describe the combustion process, the air-fuel ratio λ and the equivalence ratio ϕ are introduced. For an air/fuel mixture, the equivalence ratio is defined as [65]

$$\phi = \frac{1}{\lambda} = \frac{(\dot{m}_{\text{Air}}/\dot{m}_{\text{Fuel}})_{\text{stoich}}}{(\dot{m}_{\text{Air}}/\dot{m}_{\text{Fuel}})}, \tag{2.47}$$

where $\dot{m}_{\text{Air}}$ and $\dot{m}_{\text{Fuel}}$ are the air and fuel mass flow rates, respectively. The air-fuel ratio λ represents the relationship of a fuel-air mixture to its stoichiometric mixture. This classification determines whether combustion is rich, stoichiometric, or lean. For $\lambda < 1$, a rich mixture is present, indicating an excess of fuel that is not completely burned. A lean mixture, characterised by $\lambda > 1$, indicates an excess of oxidiser. A stoichiometric mixture is achieved for $\lambda = 1$.

2.4.1. Chemical Reaction Kinetics

Combustion processes are essentially chemical redox reactions, which can be represented by reaction equations. The main objective of this study is to numerically characterise the combustion of a lean hydrogen mixture in terms of various design configurations and equivalence ratios. To describe these mechanisms, the interplay of several hundred to a thousand elementary reactions must be taken into account [102]. These reactions collectively form a detailed reaction mechanism and define the combustion process. Consequently, a large number of additional transport equations need to be solved, resulting in a significantly higher demand for resources [100]. Generally, a reaction mechanism consisting of $r \in \{1, 2, \ldots, N_r\}$ elementary reactions and $\alpha \in \{1, 2, \ldots, N_s\}$ species can be described by the relation [97]

$$\sum_{\alpha=1}^{N_s} \nu'_{\alpha r} M_\alpha \underset{k_{br}}{\overset{k_{fr}}{\rightleftharpoons}} \sum_{\alpha=1}^{N_s} \nu''_{\alpha r} M_\alpha. \tag{2.48}$$

In Equation (2.48), the arrows indicate the direction in which a respective reaction proceeds. M_α represents the molecular weight of a species α involved in the reaction. The factors $\nu'_{\alpha r}$ and $\nu''_{\alpha r}$ represent the stoichiometric coefficients of the respective reactants and products. k_{fr} and k_{br} are the rate constants for the forward and reverse reactions, interpreted as the probability of molecular collisions. These rate constants describe the speed at which reaction r occurs [100]. At least one of these values can typically be calculated using the extended Arrhenius approach:

$$k_{i,r} = A_r T^{\beta_r} \exp\left(-\frac{E_{a,r}}{R_m T}\right), \quad \text{for } i \in [f, b], \tag{2.49}$$

where the constants A_r and β_r describe the collision frequency of the molecules. $E_{a,r}$ stands for the activation energy of the reaction and R_m is the universal gas constant [56, 58].

2.4.2. Modeling of the Chemical Source Term

Reactive flows are controlled by the fundamental equations (2.1) to (2.4). To simulate reactive, turbulent flows, it is necessary to use the averaged Navier-Stokes (NS) equations (2.20) to (2.23). Various methods for modeling these equations have been introduced in earlier chapters. However, we still need an approach to model the averaged chemical source term $\bar{S}_\alpha$ from Equation (2.23) in order to fully address the closure problem of the averaged NS equations. Therefore, the key to combustion modeling lies in describing the chemical source term and approximating the interactions between turbulent fluctuations and chemical kinetics.

As mentioned earlier in Section 2.4.1, chemical transformations in combustion processes are described using chemical reaction mechanisms. For instance, a detailed description of hydrogen combustion involves dozens of reaction steps [97, 117], which significantly increases the number of component transport equations and computational power required. In addition, complex reaction schemes have large differences in chemical time scales, leading to a stiff numerical system that requires sophisticated solution method [109]. To maintain reasonable computation times, simplified treatments of chemical reactions are used to calculate the averaged source term. Combustion models are generally categorised into component transport models and models based on tabulated chemistry [97, 120]. The following chapters will focus exclusively on the component transport models utilised in this study.

The Eddy Dissipation Model

The **E**ddy **D**issipation **M**odel (EDM) is a robust, mixing-controlled model suitable for both premixed and non-premixed combustion modeling. Originally introduced by Magnussen [14, 15] as an extension of the Eddy Break-Up model by Spalding [4], EDM is a vortex decay model, where the determining timescale corresponds to the turbulent mixing time. It assumes very fast chemical reactions compared to the turbulent mixing of fuel and oxidiser, as well as chemical equilibrium. Thus, the model presumes infinitely fast chemistry, reducing the problem of solving the chemical source term to a problem of turbulent mixing [65]. The mixing timescale in CFD-RANS is also described as the integral timescale of turbulence:

$$\tau_t = \frac{k}{\varepsilon} = \frac{1}{\beta^* \omega} \tag{2.50}$$

where β^* is a constant of the $k - \omega - SST$ Model introduced in Section 2.2.2. The reaction rate RR of a species α in the EDM approach is calculated as:

$$\overline{RR}_r^{\text{EDM}} = A \frac{\rho}{\tau_t} \left[\min \left(\min_{e,\nu'_{e,r} \neq 0} \frac{Y_e}{\nu'_{e,r} M_e}, B \frac{\sum_p Y_p}{\sum_p \nu''_{p,r} M_p} \right) \right]. \tag{2.51}$$

The empirical constants $A = 4$ and $B = 0.5$ were determined experimentally. The indices e and p denote reactant and product properties, respectively. Thus, Equation (2.51) determines the reaction rates of a global reaction r for the EDM [120].The chemical source term is then derived from the sum over all reactions as:

$$\overline{SS}_\alpha^{\text{EDM}} = M_\alpha \sum_{r=1}^{N_r} (\nu''_{\alpha r} - \nu'_{\alpha r}) \overline{RR}_r^{\text{EDM}} \tag{2.52}$$

where the summation is over all reaction rates N_r. The EDM checks whether the mixing occurs in a rich or lean area, coupling the turbulent mixing with the chemical reaction and deciding on the complete or partial conversion of the fuel. A drawback of the EDM is its tendency to overestimate reaction rates and inaccuracies in descriptions, especially when non-equilibrium effects are present. By coupling EDM with a chemistry-dominated model, these weaknesses can be partially improved. EDM is often used in combination with the **F**inite **R**ate **C**hemistry (FRC) Model, allowing for correction of overpredicted reaction rates [65, 117]. The FRC Model will be described subsequently in Section 2.4.2.

The Finite Rate Chemistry Model

The **F**inite **R**ate **C**hemistry (FRC) Model, in contrast to the EDM, considers chemical reactions occurring at a finite rate. In this model, reaction rates are determined based on velocity coefficients, calculated under the assumption of laminar chemistry. The FRC Model also accounts for the possibility of reverse reactions [65]. In a mixture consisting of N_r elementary reactions, the reaction rate RR for a reaction r can be calculated as follows [56]:

$$\overline{RR}_r^{\text{FRC}} = k_{f,r} \prod_{\alpha=1}^{N_s} [\alpha]^{\nu'_{\alpha r}} - k_{b,r} \prod_{\alpha=1}^{N_s} [\alpha]^{\nu''_{\alpha r}} \tag{2.53}$$

In Equation (2.53), the concentration of species α is given by $[\alpha] = (\rho Y_\alpha)/M_\alpha$. The velocity coefficients $k_{f,r}$ for the forward and $k_{b,r}$ for the backward reaction can be calculated using the Arrhenius approach (2.49), as described in Section 2.4.1. Equations (2.49) and (2.53) show that the reaction rate $\overline{RR}_r^{\text{FRC}}$ is a highly nonlinear function, dependent only on temperature and species concentration. The source term for the component equations, similar to EDM, is given by [120]:

$$\overline{S}_\alpha^{\mathrm{FRC}} = M_\alpha \sum_{r=1}^{N_r} (\nu''_{\alpha r} - \nu'_{\alpha r}) \overline{RR}_r^{\mathrm{FRC}} \tag{2.54}$$

The FRC Model is advantageous in laminar flows with slow chemical timescales, where the chemical timescale is larger than the mixing duration. In mixing processes, areas with laminar structures coexist with regions of intensive mixing and strong turbulence. Therefore, a combination of the EDM and FRC Models is often employed. In this approach, both reaction rates are determined for each cell, and the minimum of the two is used as the technically relevant reaction rate [65].

The Eddy Dissipation Concept Model

The **E**ddy **D**issipation **C**oncept (EDC) Model, developed by Magnussen [15], is an extension of the EDM, allowing for the inclusion of detailed reaction mechanisms in the modeling of turbulent flows [36]. The EDC Model is analogous to the concept of energy cascades and vortex decay in turbulent flow. It is based on the transport of turbulent energy from large turbulence structures to dissipation in the smallest structures. The EDC Model divides the entire flow domain into a reaction zone and the surrounding fluid, assuming that reactions occur only in the smallest turbulent structures, the so-called fine-scales. These fine-structures are treated as homogeneously mixed reactors, based on the assumption that the mixing speed within the fine-structures is significantly higher than the transfer rate between the fine-structures and the surrounding fluid. This transfer rate M^*_{tr} is calculated from the dissipation rate ε and the kinematic viscosity ν as [59, 78]:

$$M^*_{\mathrm{tr}} = \frac{1}{C_\tau} \sqrt{\frac{\varepsilon}{\nu}} \tag{2.55}$$

where $C_\tau = 0.4082$ is a constant of the characteristic residence time, which can be directly calculated from the transfer rate as:

$$\tau^* = \frac{1}{M^*_{\mathrm{tr}}} = C_\tau \sqrt{\frac{\nu}{\varepsilon}} \tag{2.56}$$

To quantify the proportion of the fine-structures in the total mass, it is assumed that the fine-structures concentrate in regions of constant energy. The proportion ζ^* of the fine-structures is modeled by the expression:

$$\zeta^* = C_\zeta \cdot \sqrt[4]{\frac{\nu\varepsilon}{k^2}} \tag{2.57}$$

where $C_\zeta = 2.1377$ is another constant, and the mass fraction is derived from Equation 2.57 as $(\zeta^*)^3$.

The mass transfer rate $\dot{R}_\alpha$ of a species α between the surrounding fluid and the fine-structures is calculated as:

$$\dot{R}_\alpha = \frac{\rho(\zeta^*)^2}{\tau^* \left[1 - (\zeta^*)^3\right]} \left(Y^*_\alpha - Y_\alpha\right) \tag{2.58}$$

Here, Y^*_α and Y_α denote the species mass concentrations within the fine-structures and in the surrounding fluid, respectively [78]. The chemical source term resulting from the EDC Model corresponds to the mass transfer rate determined in Equation 2.58 and is thus given by $\overline{S}_\alpha^{\mathrm{EDC}} = \dot{R}_\alpha$.

The EDC Model enables the inclusion of detailed reaction mechanisms in the modeling of turbulent flows. While the use of the EDC Model allows for the incorporation of detailed reaction mechanisms, the resulting numerical system becomes very stiff, requiring high computational power. Therefore, the model should only be used when the assumption of fast chemistry is invalid.

2.5. Discretisation

For the equations introduced in Section 2.1 for the complete description of reactive flows, there are no analytical solutions. To solve these differential transport equations using numerical methods, they are transformed into algebraic equations through a process known as discretisation.

Discretisation can be broadly categorised into two types: spatial and temporal. Given the scope of this work, as the simulations are conducted under the assumption of steady-state conditions, this section mainly focuses on spatial discretisation techniques and notably, the Finite Volume method (FVM) [72].

Spatial discretisation involves segmenting the computational domain into subdomains. This process reduces the infinite degrees of freedom in continuous equations to a finite number, making them computationally manageable.

Consider a generic, mass-related balance equation ϕ, with given values ϕ_1, ϕ_2, and ϕ_3 at positions x_1, x_2, and x_3. This leads to the general equation system [56]:

$$\frac{\partial \phi}{\partial t} + \frac{\partial (\boldsymbol{F}_k - \boldsymbol{F}_{\nu k})}{\partial x_k} = \boldsymbol{P}. \tag{2.59}$$

In this equation, ϕ is the variable vector, $\boldsymbol{P}$ the source vector, and $\boldsymbol{F}_k$ and $\boldsymbol{F}_{\nu k}$ with $k = 1, 2, 3$ represent the vectors of convective and diffusive fluxes in all three spatial directions.

The derivatives of ϕ are approximated using finite differences, derived from Taylor series expansions truncated after an n-th order term, resulting in a truncation error of (n+1)-th order. Issues arise if the solution functions are not differentiable to the required degree [78].

The resultant system of equations can be solved using various methods. One of the most popular methods and the one used in this work is described below:

2.5.1. Finite Volume Method (FVM)

The **F**inite **V**olume **M**ethod (FVM) is a conservative method, meaning that converged solutions invariably satisfy the balance equation [31]. Like the Finite Difference Method (FDM), derivatives can be defined as difference quotients. The computational domain is directly divided into individual volume elements in physical space. Balance equations must be established and solved for each generated volume. Since a flux leaving one cell directly enters the adjacent cell, conservation is inherently assured. Equations are integrated over a control volume, making FVM particularly suitable for conservation laws and balance equations [78]. In finite volume formulation, the general balance Equation (2.59) is transformed into [56]:

$$\frac{\partial}{\partial t} \int_V \phi \, dV + \oint_\Omega (\boldsymbol{G}_\Omega - \boldsymbol{G}_{\nu\Omega}) \, d\Omega = \int_V \boldsymbol{P} \, dV. \tag{2.60}$$

In Equation (2.60), V represents the cell volume, Ω the cell surface, and $\boldsymbol{G}_\Omega$ and $\boldsymbol{G}_{\nu\Omega}$ are the convective and diffusive fluxes through the surface. This formulation does not initially require continuously differentiable variables. Numerical solution methods typically require manageable cell structures. Therefore, although Equation (2.60) is valid for any volume, the computational domain is generally divided into rectangles or triangles for two-dimensional simulations and into hexahedra or tetrahedra for three-dimensional simulations. This division is graphically represented in Figure 2.5. The surface integral from Equation (2.60) can be replaced by the sum over all cell sides due to the transition to simple cell geometries. For a cell z with a constant temporal cell volume V, cell side k, and areas Ω_k, the following expression is obtained:

$$\frac{\partial \phi}{\partial t} + \frac{1}{V} \sum_{k=1}^{z} (\boldsymbol{G}_k - \boldsymbol{G}_{\nu k}) \Omega_k = \boldsymbol{P}, \tag{2.61}$$

with the mean convective flux vector $\boldsymbol{G}_k$ and the mean diffusive flux vector $\boldsymbol{G}_{\nu k}$.

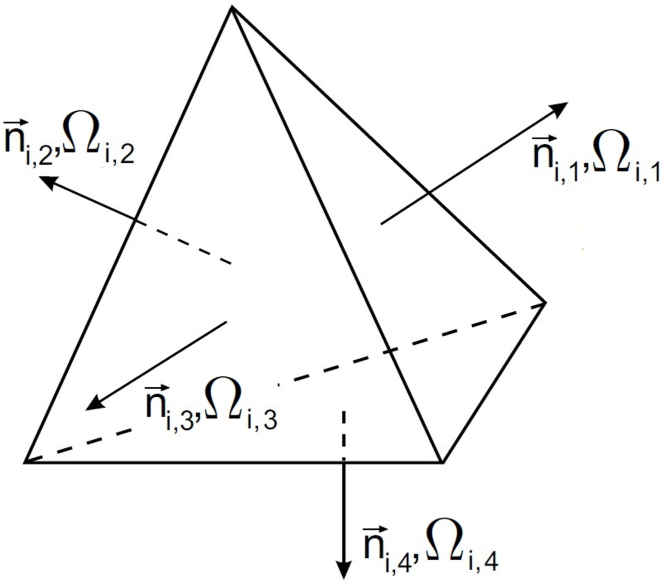

Figure 2.5.: Control Volume for the Finite Volume method. Shown is a control volume V_i with the surfaces $\Omega_{i,k}$ and the surface normal vectors $\vec{n}_{i,k}$. Adapted from [78].

When calculating the source and flux vectors, truncation and discretisation errors can occur. These depend on the discrete location of the variable vector. The calculated fluxes of a cell side are subject to a certain spatial accuracy order if, for example, the variables are located at the cell center. Thus, the FVM can work with arbitrary volumes, allow local adaptation of the computational grid, and show advantages in metric singularities. Due to these benefits, the FVM is used much more frequently than the FDM [56].

3. FLOX® Based Gas Turbine Combustor

The ATM-Combustor (name used interchangeably with atmospheric combustion chamber) used in this study is a two-stage combustor used for Turbec T100 MGT (Refer to [115] for details about the MGT). The primary stage consists of ten air/fuel nozzles arranged in a circle. The fuel is coaxially introduced with the air and mixes in the subsequent premixing section before entering the combustion chamber. This coaxial fuel delivery creates a high impulse of the air/fuel mixture at the entrance to the combustion chamber, resulting in a jet-stabilised flame. A significant recirculation zone, typical for FLOX® combustors, forms in the center of the circularly arranged nozzles, where hot exhaust gas recirculates back to the nozzle, heating the unburnt gas and stabilising combustion.

An additional pilot stage is located deeper in a cylindrical pilot area, precisely on the combsutor's axis of symmetry. Depending upon the configuration and the variant, the air/fuel mixture in these stages is premixed before entering the combustion chamber. For the swirl-based configuration, the air is introduced radially to the fuel through a swirl generator, creating a swirl-stabilised flame. The swirling pilot flame allows radially expanding combustion gases at the end of the pilot stage to mix with the unburnt air/fuel mixture from the primary stage, further heating and stabilising the primary stage combustion.

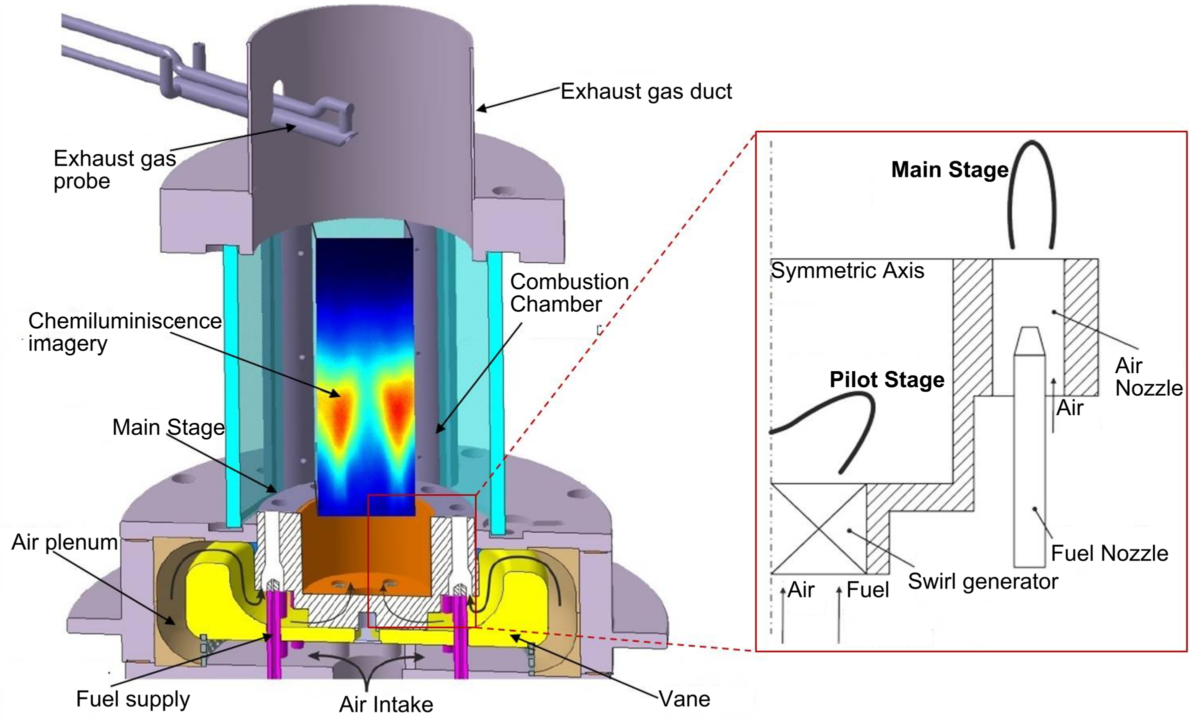

Figure 3.1.: Schematic of an atmospheric combustor. Shown is a sectional view (left) of the entire ATM-combustor and a detailed view (right) of the fuel injection for the swirl-stabilised pilot stage. Inspired from [106, 115].

Figure 3.1 illustrates the chamber's and the test bench structure for clarity. The atmospheric test rig combustor has a hexagonal shape and is equipped with quartz glass windows for optical access to the combustion chamber, crucial for OH*-chemiluminescence recordings and high-resolution imaging. The quartz glass panes are held in place by metal frames and are arranged so that the first nozzle is directly behind the first pane. A camera, positioned perpendicular to the pane, thus looks directly at the first nozzle. Due to the nozzle arrangement, the sixth nozzle can also be observed as it lies on a line with the first nozzle. The camera's viewing direction is graphically represented in Figure 3.2. The position and size of the measurement volume for OH*-chemiluminescence recordings are essential for later comparison with simulation results. This technique measures the frequency of OH* radicals, which are short-lived and only appear in the reaction zone of the flame, making it suitable for determining flame lift-off height or shape [83].

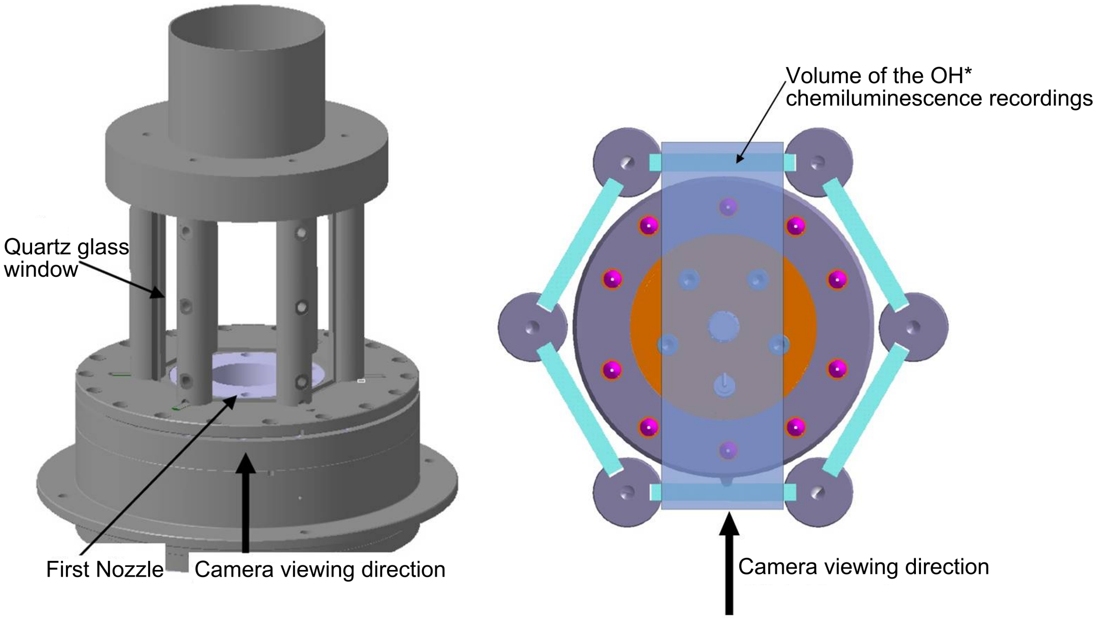

Figure 3.2.: Camera viewing direction for the ATM-combustor. Presented is an isometric view (left) as well as a top view (right), in which the camera viewing direction and the measurement volume for OH*-chemiluminescence recordings are indicated. Inspired from [106, 115].

The necessary combustion air is supplied separately and preheated via an air heater. As shown in Figure 3.1, it is introduced from below through an air inlet and redirected in the air plenum to the pilot burner and the main stage nozzles. The mixing with the unheated fuel occurs in the nozzles. The test setup primarily focuses on characterising the flame in different operating points with various fuels. The hot exhaust gas is thus led away via an exhaust tract and not further used, but additional exhaust gas and noise measurements are conducted during burner operation.

3.1. Flame Stabilisation

To comply with current emission regulations, modern gas turbines for the combustion of gaseous fuels operate with lean premixed combustion systems. This means that the fuel is burned with a local excess of air. As a result, flame temperatures are reduced, thereby lowering pollutant emissions [128]. This is particularly effective in significantly reducing nitrogen oxide (NO_x) emissions. However, under these conditions, the flame speed is reduced. The desire for high power densities also results in high flow velocities within the combustion chamber [128]. In the highly turbulent flow, stabilisation of the flame solely through diffusive transport processes is insufficient, as not enough heat and free radicals from the reaction zone can be transported into the still unburned air-fuel mixture. It is therefore necessary to influence the flow field within the combustion chamber in such a way that one or more recirculation zones are formed [128]. These recirculation areas cause an additional convective back transport of hot exhaust gases and the radicals contained within them towards the burner exit. The mixing of these gases with the unburnt air-fuel mixture increases reactivity and allows for stable, low-emission combustion even at high flow velocities. The achievable power densities also allow for a very compact combustion chamber design [128].

To ensure stable combustion across a wide operating range, it is usually sensible to design the combustion chamber with several burner stages. Typically, a pilot stage is combined with a main stage. The pilot stage is used during ignition and to stabilise the main stage, especially in lean partial load operation. Much better flame stabilisation can be achieved through swirl or jet stabilisation [128], both stabilisation concepts are described in more detail below.

3.1.1. Swirl-Stabilised Combustion

In swirl-stabilised combustion chamber systems, a swirl is imparted to the air or air-fuel mixture before it enters the combustion chamber [128]. In its simplest form, this is done using a swirl generator, while in more complex designs, multiple swirl generators can be combined. The swirl creates a pressure field in the combustion chamber, leading to a strong recirculation zone near the combustor axis.

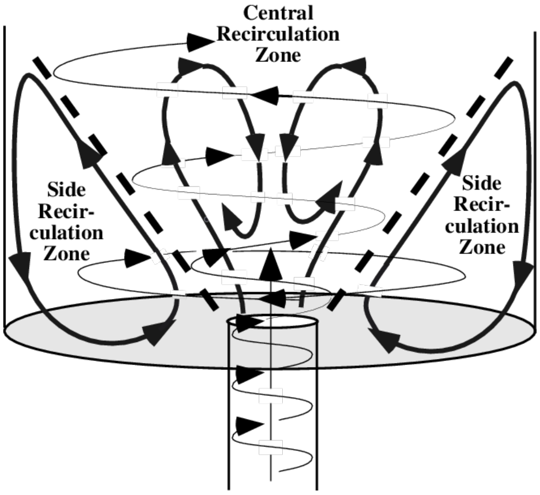

Figure 3.3.: Swirl-stabilised combustor schematic. Inspired from [51].

In the highly turbulent shear layers of these recirculation areas, a flame front can stabilise despite high flow velocities [128]. Due to the flow field, the compact reaction zone in swirl burners typically takes on a V-shape.

Swirl flames are characterised by high power density and a broad operable range with low NO_x and wherever applicable; CO emissions [128]. They are therefore widely used in industrial combustion chambers. The basic structure is similar in all designs, with differences mainly in the premixing of the fuel. Figure 3.3 illustrates the schematic of a Swirl-stabilised Combustor.

3.1.2. Jet-Stabilised Combustion

In jet-stabilised combustion chamber systems, the air-fuel mixture is injected into the combustion chamber through typically circularly arranged nozzles with high axial momentum [128]. This action creates a strong recirculation zone along the combustor axis, as demonstrated in Figure 4.2. The unswirled, partially premixed fresh gas jets enter the combustion chamber with significant axial momentum. This momentum generates the illustrated recirculation area, which transports hot exhaust gases from behind the reaction zone back to the burner exit [128, 142]. The mixing of the unburnt air-fuel mixture with the recirculating exhaust gases occurs in the turbulent shear layers of the jet flow.

The high recirculation rates and the associated transport of heat and radicals result in effective flame stabilisation. At the same time, the dilution of fresh air also lowers the reaction rates [91]. Consequently, the reaction zone expands more and occupies a larger volume in the combustion chamber. This leads to a homogeneous temperature field in the combustion chamber, where the temperature peaks slightly exceed the adiabatic flame temperature of the global mixture [142]. This homogeneous temperature field is the basis for the low NO_x emissions of this combustor type, as the dominant formation of nitrogen oxides through the thermal pathway is strongly influenced by the combustion temperature [67, 142].

3.2. Relevant Phenomena for the Design of Combustion Chambers

In the concept phase of developing a combustion chamber, particular attention should be paid to certain phenomena in combustion. This includes the early consideration of expected adiabatic flame temperatures and the risk of flame flashback and auto-ignition, especially in premixed combustion concepts. Through such an evaluation, the assessment of various concepts can be supported early on with simple means.

3.2.1. Adiabatic Flame Temperature

The calculation of the adiabatic flame temperature is a method for estimating the potential flame temperatures within a combustion chamber [102]. This approach considers only a few stable reaction products and complete reactions. Dissociation of the reaction products and pollutants are not explicitly included. Typically, adiabatic flame temperatures for a specific fuel and oxidiser are calculated at various equivalence ratios. With the temperature dependence of the molar enthalpy

$$H_{m,\alpha}(T) = H^0_{m,f,\alpha} + \int_{T_0}^{T} C_{m,p,\alpha}(\vartheta) d\vartheta, \tag{3.1}$$

the adiabatic flame temperature T_{ad} can be calculated for isobaric processes and the corresponding relationship between enthalpy and energy exchange $\Delta Q = 0 = \Delta H$ with

$$0 = \sum_{\alpha=1}^{N_k} \nu''_{\alpha} H''_{m,\alpha}(T_{\mathrm{ad}}) - \sum_{\alpha=1}^{N_k} \nu'_{\alpha} H'_{m,\alpha}(T_1). \tag{3.2}$$

In addition to the standard formation enthalpy $H^0_{m,f,\alpha}$ of the considered species α (with $\alpha = 1, 2, ..., N_k$) in Equation (3.1), knowledge of the temperature-dependent, molar heat capacity $C_{m,p,\alpha}(\vartheta)$ of the respective species is also required. The temperature T_1 in Equation (3.2) refers to the temperature of the reactants before the reaction of the considered mixture. The stoichiometric coefficients for the product species ν'' and for the reactant species ν' in Equation (3.2) are derived from the reaction equation considered for the calculation, such as $2H_2 + O_2 \rightarrow 2H_2O$. Considering the threshold temperature from Section 3.3, above which the formation rate of thermal nitrogen oxides significantly increases, a statement about the preferred mixture formation (premixed/non-premixed) in a combustion chamber can be made based on the absolute value and trend of the adiabatic flame temperature over the equivalence ratio φ. Furthermore, the calculated adiabatic flame temperatures allow for an estimation of the thermal load on components within the combustion chamber.

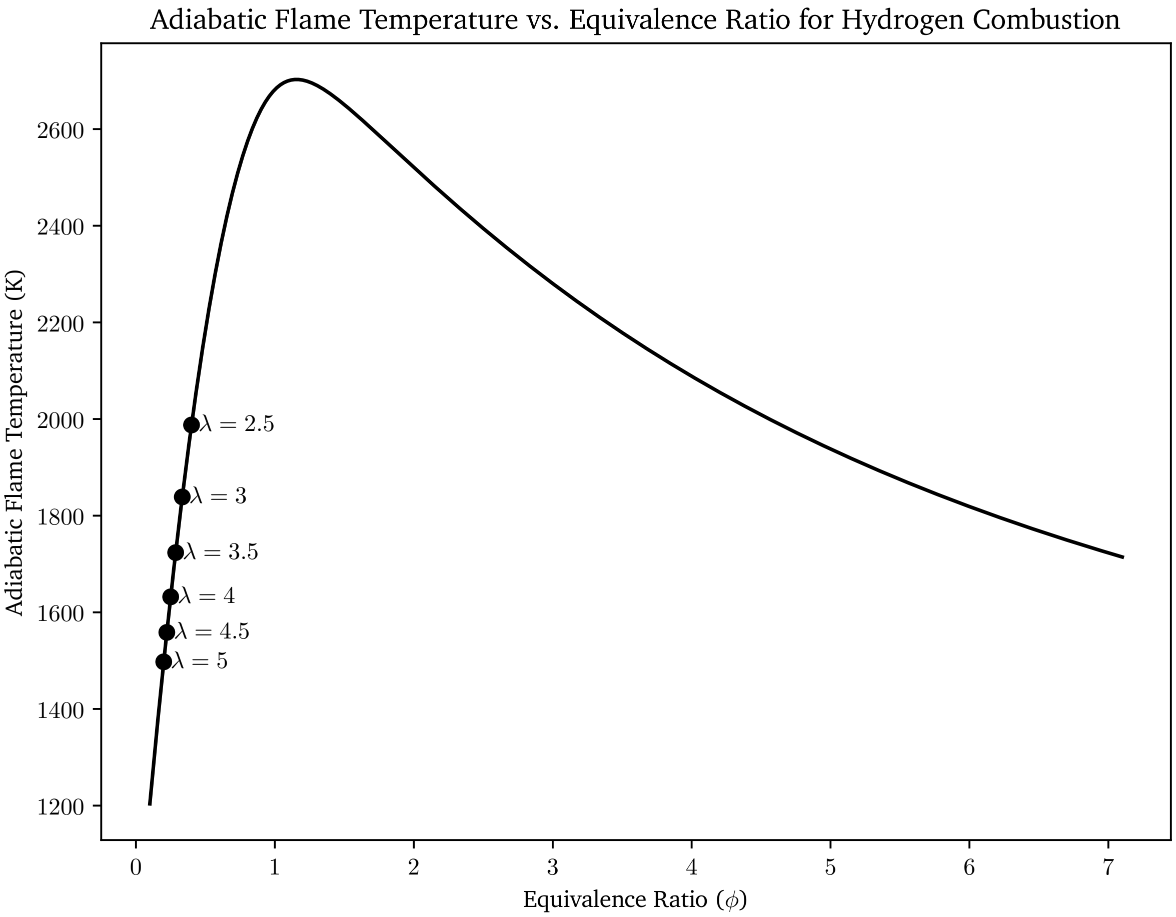

Figure 3.4.: Variation in Adiabatic Flame Temperature with respect to the equivalence ratio ϕ. Since the operating points were defined on the basis of air-fuel ratio λ, they have been marked in the plot as well.

Figure 3.4, displays the relation between Adiabatic Flame and the equivalence ratio ϕ. The plot is based on the DC1S30N18 [135], an in-house DLR fuel surrogate mechanism. Please refer to Section A.3 for the code containing the calculation and the parameters used.

Additionally, since the study was done by varying the air mass flow rate, keeping in mind the air-fuel ratio(λ), these values of (λ) have also been labelled on the plot.

3.2.2. Flame Flashback

Flame flashback refers to the unwanted ignition of the flame moving from the designated combustion zone back into the area where the mixture formation occurs in premixed combustion concepts. The risk of flame flashback lies in the potential damage to components, such as the fuel injector, leading to the malfunction of the entire combustion chamber. In the literature, mainly three different mechanisms for flame flashback are mentioned, with a fourth mechanism reported for swirl-stabilised combustion chambers [16, 82, 87, 121].

- **Turbulent Flame Propagation:** Flame flashback within a turbulent core flow of a fuel-air mixture refers to the advancement of a flame in the opposite direction of the flow. This occurs when the laminar or turbulent flame speeds exceed the local flow velocities themselves [16, 76]. Since the flow velocities in typical gas turbine combustion chambers are generally very high, this type of flame flashback usually plays a minor role [121].

- **Flame flashbacks due to Thermo-Acoustics:** Thermo-acoustic combustion instabilities can cause velocity fluctuations on the order of the main flow [121]. The consequence of periodically stagnating main flow is a flame flashback, which either occurs oscillating with the thermo-acoustic frequency or leads to a permanent stabilisation of the flame at a different location upstream of the combustion chamber [122].

- **Flame Propagation in the Boundary Layer:** Since the flow velocity directly at a wall must necessarily go to zero, there is a risk of flame flashback in this boundary layer [122]. This is referred to as boundary layer-induced flame flashback [82, 95]. Until a few years ago, this type of flame propagation was assumed to be exclusively a phenomenon based on the equilibrium between the flow velocity in the boundary layer and the local flame speed. In other words, flame flashback occurs when a critical velocity gradient at the wall is undercut. Eichler and Sattelmayer hypothesised that neglecting the effects of a flame on the upstream flowing mixture does not consider all relevant physical processes [94]. Accordingly, the pressure increase in front of a flame and the low momentum in the boundary layer create a small recirculation zone, which favors upstream flame propagation along the boundary layer.

- **Combustion-Induced Vortex Breakdown:** In swirl-stabilised combustion chambers, a fourth mechanism for flame flashback occurs that is independent of the specific combustion chamber design [46, 70]. This type of flame flashback is predominant in swirl-stabilised combustion chambers. The driving mechanism here is a negative gradient of the azimuthal vorticity of the swirled flow, which exerts a negative axial moment on the recirculation zone, transporting it upstream [87]. This azimuthal vorticity in swirled flows is a measure of the stability of the flow field [87]. Analogous to boundary layer-induced flame flashback, the flame then follows the upstream transported vortex.

  Fritz et al. [46] recognised early on that beyond a critical swirl number, the recirculation zone of a non-reacting flow can extend upstream. Since they observed that this effect can still be induced by a chemical reaction at optimal swirl numbers, this phenomenon is also referred to as **C**ombustion-**I**nduced **V**ortex **B**reakdown (CIVB) [96]. This phenomenon becomes more pronounced both with enrichment of the mixture composition and with the addition of hydrogen in swirl-stabilised combustion chambers [87].

Due to the high inflammability nature of hydrogen, flame flashbacks can be expected, especially in the premixed variants. Figure 3.5 shows the laminar flame speeds of various fuels over the combustion air-fuel ratio λ.

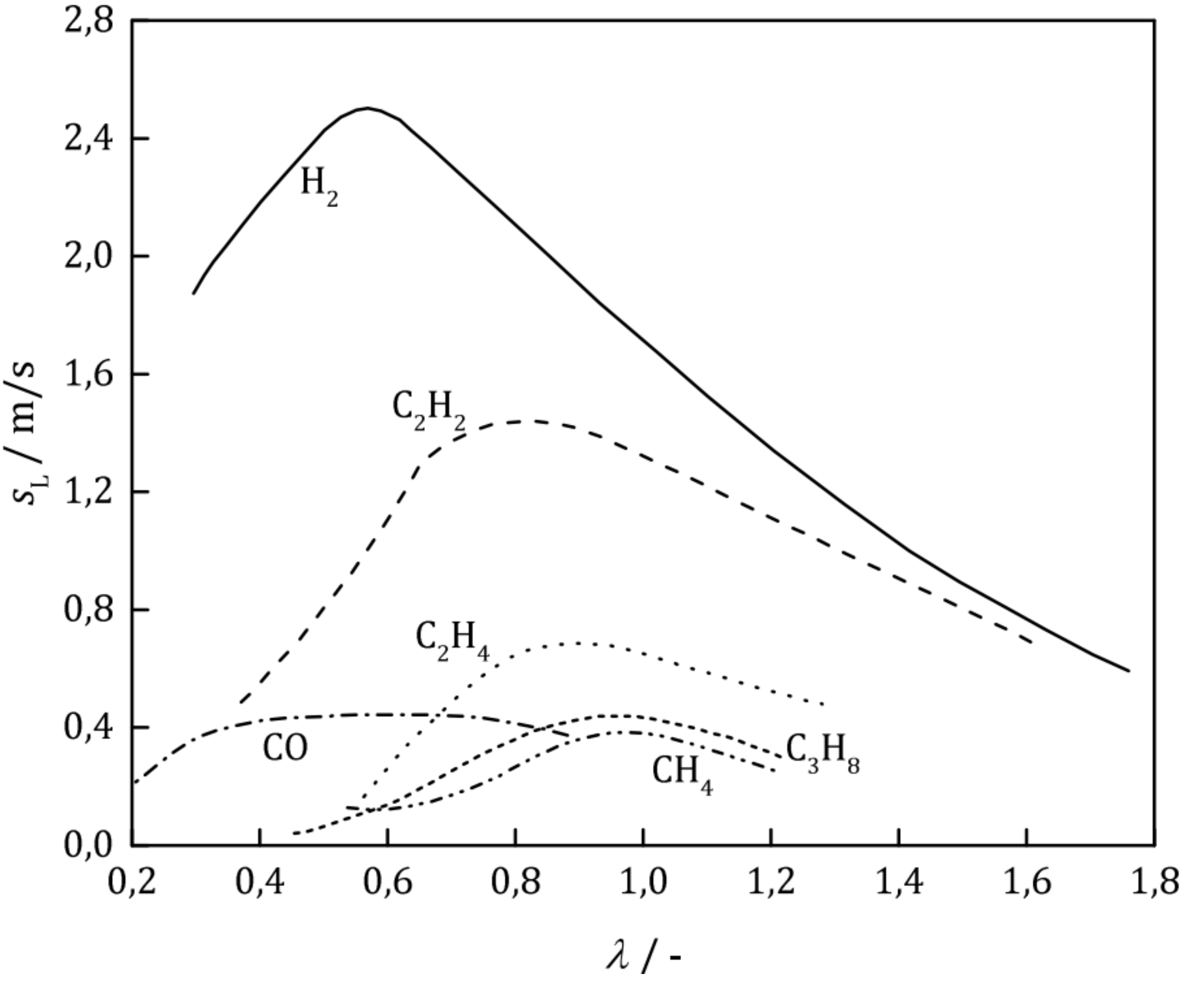

Figure 3.5.: Flame speeds of various fuels mixed with air under ambient conditions, over a range of air-fuel ratios λ [104].

It is evident that hydrogen, compared to methane, has a significant impact on the maximum laminar flame speeds, which is why special attention is paid to the Hydrogen or fuels with hydrogen content.

3.2.3. Auto-Ignition

Auto-ignition generally refers to the transition of a fuel-air mixture from a non-reacting or slowly reacting state to a self-sustaining combustion [3]. A spark or a hot surface as an energy source represents an external means to provoke ignition, hence referred to as external ignition or induced ignition [65]. For so-called spontaneous ignition or auto-ignition to occur without an explicit ignition source, a combustible fuel-air mixture must be present at temperatures higher than the auto-ignition temperature [108]. During auto-ignition, an induction time τ_{ign} can be observed, preceding the actual ignition in terms of fuel conversion. This so-called ignition delay time τ_{ign} is a characteristic phenomenon in chemical reactions, involving a multitude of elementary reactions each assignable to a so-called radical chain mechanism [102].

Chain mechanisms can be differentiated into chain initiation, chain branching, chain propagation, and chain termination. Together, these mechanisms form a so-called reaction mechanism. The individual radical chain mechanisms are explained using the hydrogen-oxygen system as an example. At the beginning of a reaction, only the reactants H_2 and O_2 are available. During chain initiation,

$$H_2 + O_2 \rightarrow HO_2 + H, \tag{3.3}$$

reactive species HO_2 and H are formed from the stable reactants H_2 and O_2 [102]. In the chain branching reactions of Equations (3.4) and (3.4), one reactive and one stable molecule form two reactive molecules each [102],

$$H + O_2 \rightarrow OH + O, \tag{3.4}$$

$$O + H_2 \rightarrow OH + H. \tag{3.5}$$

In the hydrogen system, a reactive H particle is transferred through the two branching reactions in Equations (3.4) and (3.5), resulting in the formation of two OH radicals. Although the chain branching in Equation (3.5) occurs very slowly at low temperatures due to its endothermic nature, it simultaneously represents one of the most critical elementary reactions in combustion [18, 26, 34, 89]. On the other hand, the so-called chain propagation

$$OH + H_2 \rightarrow H_2O + H \tag{3.6}$$

is characterised by one reactive particle (OH) reacting with a stable molecule to form another reactive particle (H) [102].

The total sum of reactive particles, also called radicals, remains constant through these types of reactions. The OH radicals generated from the previous chain branching are also converted to H radicals through chain propagation as shown in Equation (3.6). In total, chain branching and propagation lead to an increase in H radicals. The rate-determining reaction is Equation (3.4), whose reactants in the hydrogen system, along with a neutral third body M, also form the trimolecular collision reaction

$$H + O_2 + M \rightarrow HO_2 + M, \tag{3.7}$$

referred to as chain termination, as the reactive species H is consumed to form the molecule HO_2. Here, the neutral third body M represents any molecule in the reaction system that is available as a collision partner. Although HO_2 is not a stable molecule according to the definition of chain termination by Warnatz [102], its reactivity is significantly lower than that of an H atom. This buffering of reactive H radicals increases the ignition delay time. With increasing pressure under otherwise identical thermodynamic conditions, the reactivity of the hydrogen system decreases due to the pressure-dependent termination reaction in Equation (3.7). Furthermore, the HO_2 radical is partially converted into H_2O_2. The thermally unstable HO_2 and H_2O_2 molecules decompose very quickly upon slight changes in conditions to H and OH radicals, eventually igniting the mixture [84]. Consequently, the hydrogen peroxide molecule H_2O_2 must be taken into account when describing auto-ignition processes using reaction mechanisms [81].

3.3. Pollutant Formation - NO$_x$ emissions

An important optimisation goal in the development of combustor systems is the minimisation of pollutants generated during the combustion process. While pollutants like carbon dioxide (CO_2), carbon monoxide (CO), **U**nburnt **H**ydro**c**arbons (UHC), and **V**olatile **O**rganic **C**ompounds (VOCs) are also significant, in this study focusing on pure hydrogen operation, nitrogen oxides (NO_x) are primarily relevant.

Nitrogen oxides NO and NO_2 play a crucial role in the creation of environmentally and health-damaging ozone in the troposphere, thus leading to the terminology ”photochemical smog” [22]. Moreover, these nitrogen oxides contribute to the depletion of the crucial ozone layer in the upper stratosphere [27]. For these reasons, nitrogen oxides are deemed notably impactful pollutants in combustion [102]. The most notable pathways are thermal NO and NO produced via the dinitrogen oxide (N_2O) mechanism [102]. The prompt NO (Fenimore NO) mechanism or the conversion of fuel-bound nitrogen to NO, which is relevant for many solid fuels, can be disregarded in this study since only Hydrogen is under examination.

3.3.1. Thermal NO (Zeldovich-NO)

The formation of so-called Zeldovich-NO [2] is described by the elementary reactions [32]:

$$O + N_2 \xrightarrow{k_1} NO + N, \tag{3.8}$$

$$N + O_2 \xrightarrow{k_2} NO + O, \tag{3.9}$$

$$N + OH \xrightarrow{k_3} NO + H. \tag{3.10}$$

Since the activation energy of the first reaction in Equation (3.8) is very high due to the strong N_2 triple bond, it only proceeds rapidly at very high temperatures [102]. The Zeldovich-NO produced is therefore also referred to as thermal NO. The elementary reaction from Equation (3.8) is the rate-determining step of thermal nitrogen oxide formation due to its relatively low reaction rate [65]. The formation rate of thermal NO can be expressed by establishing the time law for elementary reactions (3.8)-(3.10) and a quasi-steady consideration of the atomic nitrogen concentration [N] with the simple relation

$$\frac{d[\mathrm{NO}]}{dt} = 2k_1[\mathrm{O}][N_2]. \tag{3.11}$$

From Equation (3.11), it is apparent that there are exactly four possibilities to minimise thermal NO. Firstly, the significant rate coefficient k_1 can be reduced by lowering the temperature. Two additional possibilities involve reducing the concentration of atomic oxygen or molecular nitrogen. The atomic oxygen concentration could, for example, be lowered by external or internal exhaust gas recirculation, where the reduction of the molecular oxygen concentration contributes to the desired effect. A reduction in nitrogen concentration, on the other hand, can be achieved by using pure oxygen as the oxidiser, which, however, is not feasible in air-breathing combustion concepts. The only remaining option besides temperature and exhaust gas recirculation to reduce thermal nitrogen oxide emissions according to Equation (3.11) is to reduce the time span dt, i.e., the residence time available for the formation of thermal NO.

3.3.2. NO Produced via Dinitrogen Oxide (N_2O)

In the so-called dinitrogen oxide mechanism

$$N_2 + O + M \rightarrow N_2O + M, \tag{3.12}$$

molecular oxygen and atomic oxygen react together with an inert collision partner M to form Dinitrogen oxide [65]. This reaction in Equation (3.12) occurs more frequently at higher pressures since it involves a collision reaction and reduces the number of resulting molecules [8]. In a subsequent reaction with O atoms

$$N_2O + O \rightarrow NO + NO, \tag{3.13}$$

N_2O reacts to NO [12]. This formation mechanism plays a particularly important role under lean conditions and low temperatures. Under such conditions, the Zeldovich mechanism introduced in the previous sections contribute very little to NO formation [65]. It follows that in gas turbine combustors with high pressures and a very lean premixing, this dinitrogen oxide mechanism dominates the formation of NO.

While CO emissions are not relevant for our work, Figure 3.6 illustrates the impact of temperature on CO and NO_x emissions.

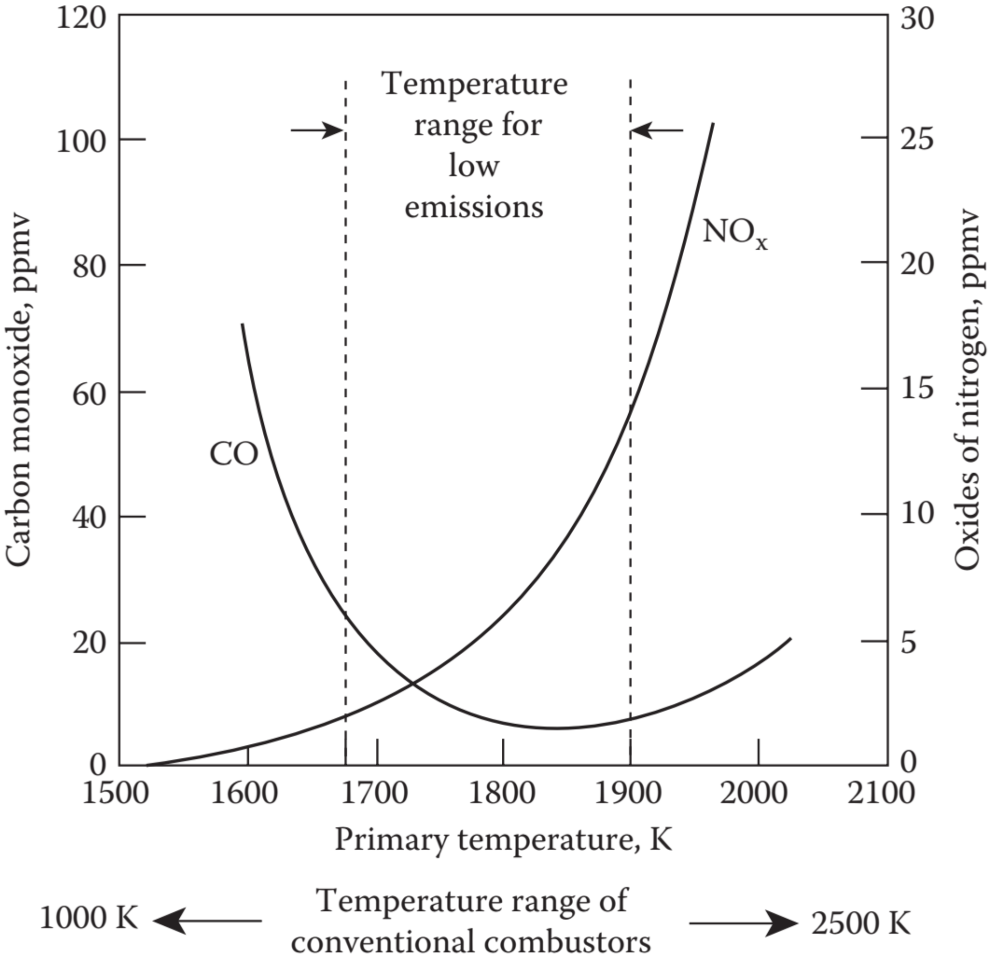

Figure 3.6.: Dependence of CO and NO_x emissions on Adiabatic Flame Temperature. Adapted from [85].

4. Combustor Configurations, Fuel variability, and Evaluation Methods

In this work, the combustion of Hydrogen is analysed to fully characterise the atmospheric (ATM) combustion chamber. Simulations of various parameters are conducted and compared for different operating points. The following sections will introduce the different combustor configurations and the air-fuel ratios used. Finally, the methods used for evaluation and the underlying calculations will be explained.

4.1. Configurations and Variation of the Air-Fuel mixture

For the purpose of this thesis, two configurations (and two variations for one configuration) of the combustion chamber are tested. These configurations are described as follows:

1. Both the main and pilot stages are jet-stabilised.
   a) Non-premixed Main stage.
   b) Premixed Main stage with a mixing length of $30\,\mathrm{mm}$.
2. Jet-stabilised Main stage with a swirl-stabilised Pilot stage, without premixing.

In both configurations, there are 10 Main stage nozzles.

As for the composition of the air-fuel mixture, λ variations were made from $\lambda = 2.5$ to $\lambda = 5$, with increments of 0.5 for all three variations, for the purposes of the characterisation. The fuel used was pure hydrogen, and air was used as an oxidiser, consisting of $23.1\%\,\mathrm{O_2}$ and $76.9\%\,\mathrm{N_2}$ by mass fractions.

4.2. Methods for Evaluating Simulation Results

Various methods are employed in this work to assess and evaluate the conducted simulations. It is verified whether any errors occur during the simulation that could distort the solution or whether the solution has fully converged. Additionally, the flow field is evaluated at predefined points within the flow.

To make a statement about the quality of the simulation, longitudinal sections through the combustor with various flow properties are created. Moreover, the heat release in the combustion chamber is calculated, and the heating value of the resulting combustion is checked against the predefined value. The methods used for checking and evaluation are detailed in the following chapters.

4.2.1. Representation of Convergence Behavior

Each simulation requires solving a certain number of balance and transport equations, which arise from the number of species involved in the reaction mechanism. These equations are solved iteratively, meaning the calculated field quantities of one iteration are used as the starting value for the next iteration step. As explained in Section 2.2, these equations are partially modeled, resulting in approximate solutions. An inherent deviation from the exact result, known as the residue, always occurs due to the approximation. The difference between two consecutive iteration results is referred to as the progress of the simulation.

The convergence behavior of a simulation is best determined by examining the residues. They are displayed over the entire course of a simulation.

Figure 4.1 presents a residual trend for the combustion simulation of the ATM-Combustor, swirl-stabilised jet stage with a thermal power of $P_{\text{therm}} = 80$ kW and $\lambda = 3.5$ for pure Hydrogen.

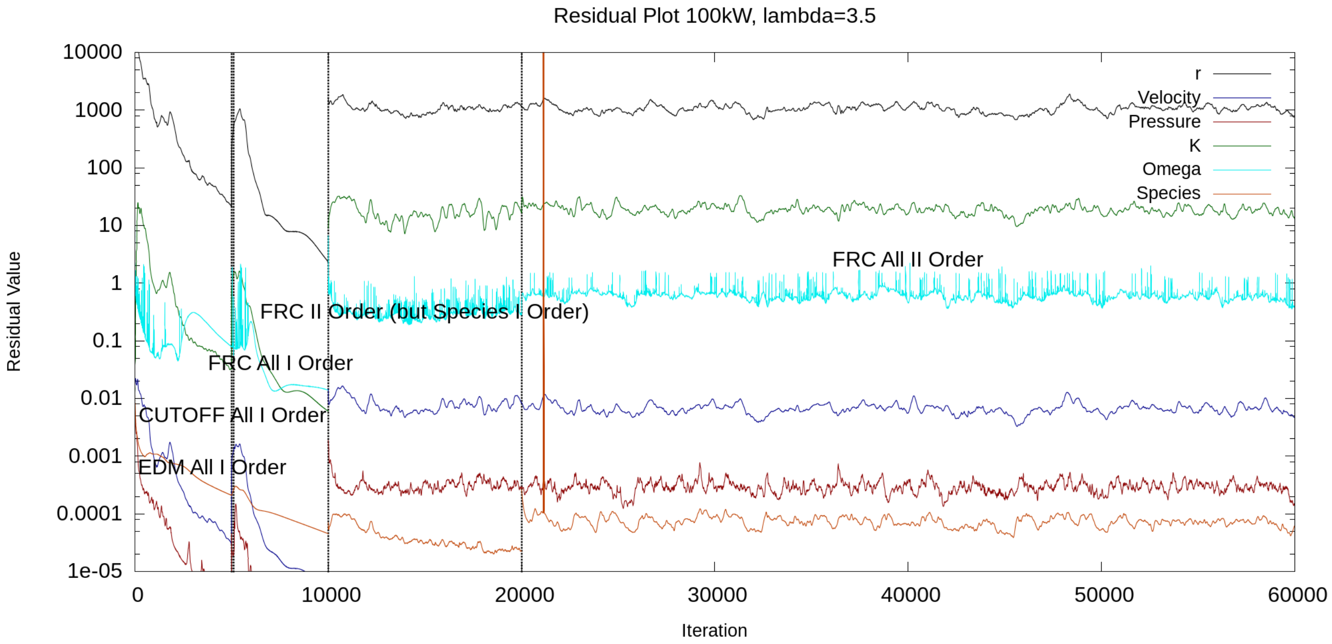

Figure 4.1.: Residual trend for the combustion simulation of the ATM-Combustor, swirl-stabilised jet stage with a thermal power of $P_{\text{therm}} = 80$ kW and $\lambda = 3.5$ for pure Hydrogen.

In this diagram, the residuals are plotted against the number of iterations. The change in residuals should ideally tends towards zero. Due to the logarithmic Y-axis, it is evident that the residuals for high iteration numbers fluctuate within a very small range. This is because each iteration passes its solution value as the starting value for the following iteration, and only a certain accuracy can be achieved due to the chosen modeling. The dashed vertical lines clarify at which point a new combustion model is activated. The exact sequence of a simulation is discussed in detail in Section 5.1.

From Figure 4.1, it is quite clear that the Simulation approaches absolute convergence with a First-order scheme. However, as soon as a switch to a higher-order scheme is made, either partially or fully; the Simulation seems to reach 'Oscillatory convergence' wherein the residuals neither decrease nor increase but rather fluctuate within a finite range. Possible reasons for this include increased numerical sensitivity of higher-order schemes and inherently transient properties of the flow.

4.2.2. Flow Evaluation at Fixed Monitor Points

While the analysis of residuals provides insights into the convergence, it does not guarantee that the flow result is physically sensible and that the flow properties do not change further. Similarly, when the Simulation residuals reach an 'Oscillatory' converge, one can verify if the physical properties have attained stability by evaluating them at certain locations. Therefore, measurement points (monitor points) are introduced at predefined locations where the flow can be evaluated over the course of the simulation. Both the monitor points line on the center line of the Combustion chamber, one being quite close to the outlet (5mm inside) and one roughly in the center (165 mm from the outlet/200 mm from the entry of pilot stage). The exact positions of the monitor points are illustrated in Figure 4.2.

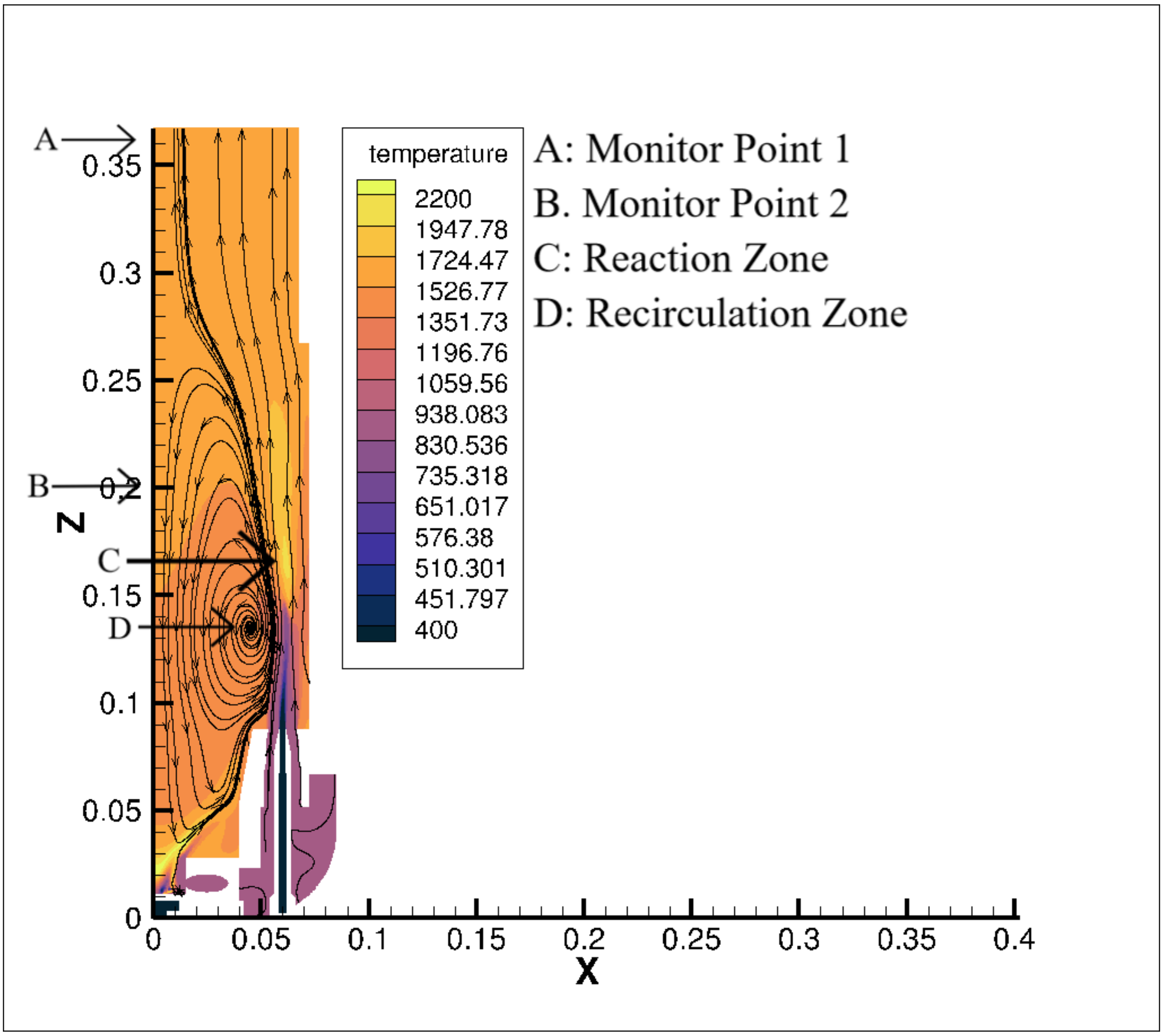

Figure 4.2.: Location of Monitor Points

At these positions, properties such as Temperature, Mass fractions of fuels and emissions are plotted over the course of the simulation, resulting in diagrams like those shown in Figure 4.3. These diagrams allow expressing the change in flow properties over the course of the simulation. When the change in a property approaches zero or the values do not diverge and keep on oscillating between two finite limits, it can be assumed that the result is no longer changing, and a solution has been achieved.

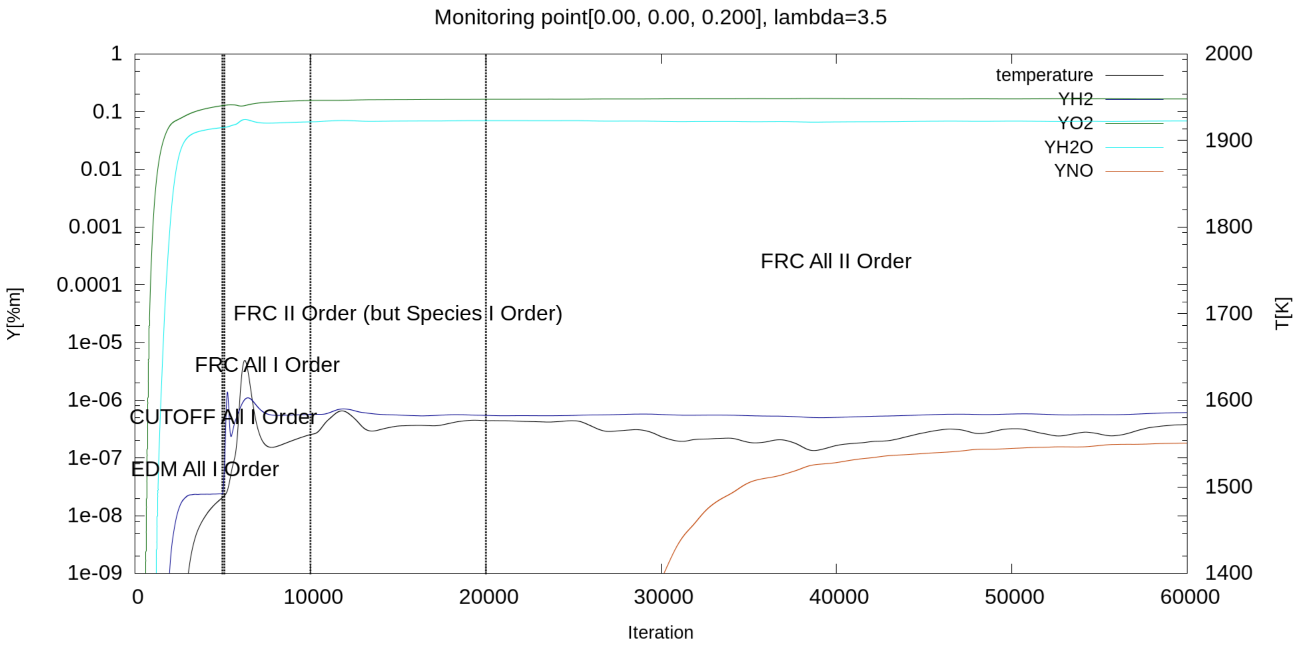

(a) Monitoring Point: 0.0 0.0 0.200

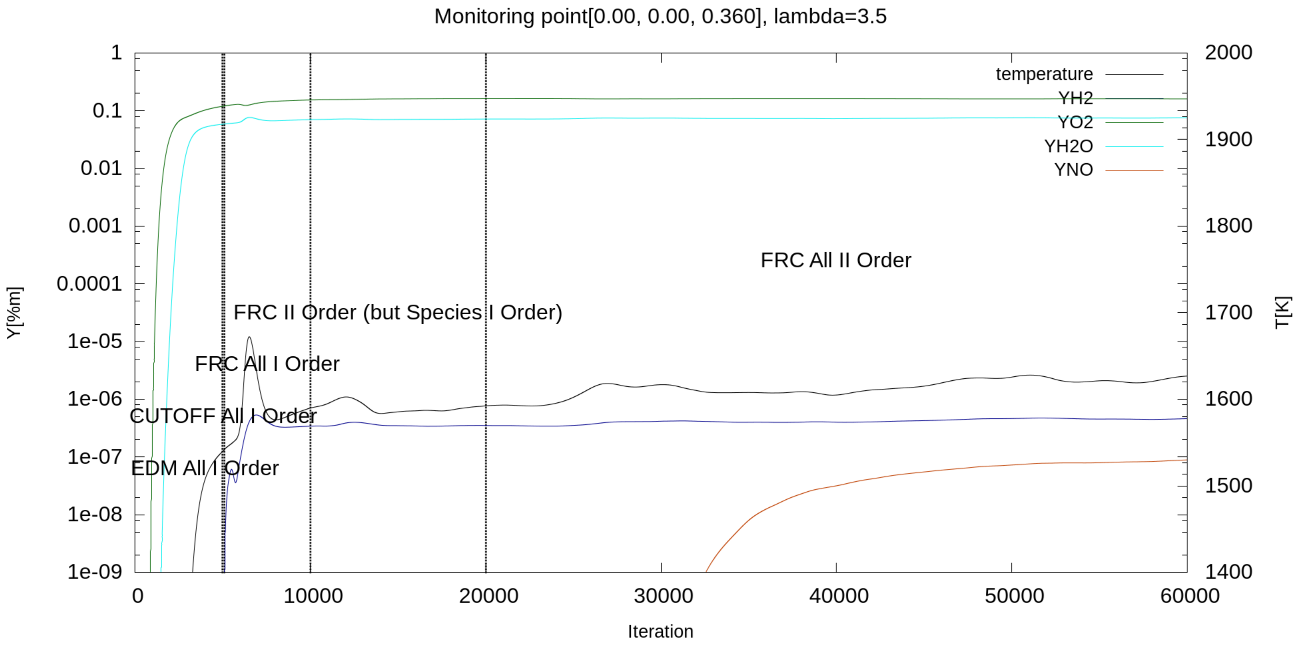

(b) Monitoring Point: 0.0 0.0 0.360

Figure 4.3.: Monitor Plots at two pre-defined reference points for air-fuel ratio λ = 3.5

The trend of velocity and temperature for the four monitor points in Figure 4.3 shows that an approximately constant value is reached for large iteration numbers. In combination with the evaluation of residuals, this allows for a detailed statement about the convergence and the result of the simulation.

4.2.3. Evaluation of the Flow characteristics over a section plane

The previous evaluation methods have shown that the simulation has converged and the flow properties provide physically correct and constant results. To gain a comprehensive understanding of the simulation outcome, it is essential to visualise the entire flow field. Therefore, cross-sectional views of various flow properties are created for each simulation. These include longitudinal sections through the entire combustor, cutting both the pilot and main stage nozzles, thus illustrating all effects during combustion. Figure 4.4 presents a comparison of the cross-sectional views for the ATM-Combustor operating on Hydrogen, corresponding to the reference case introduced in Section 4.2.

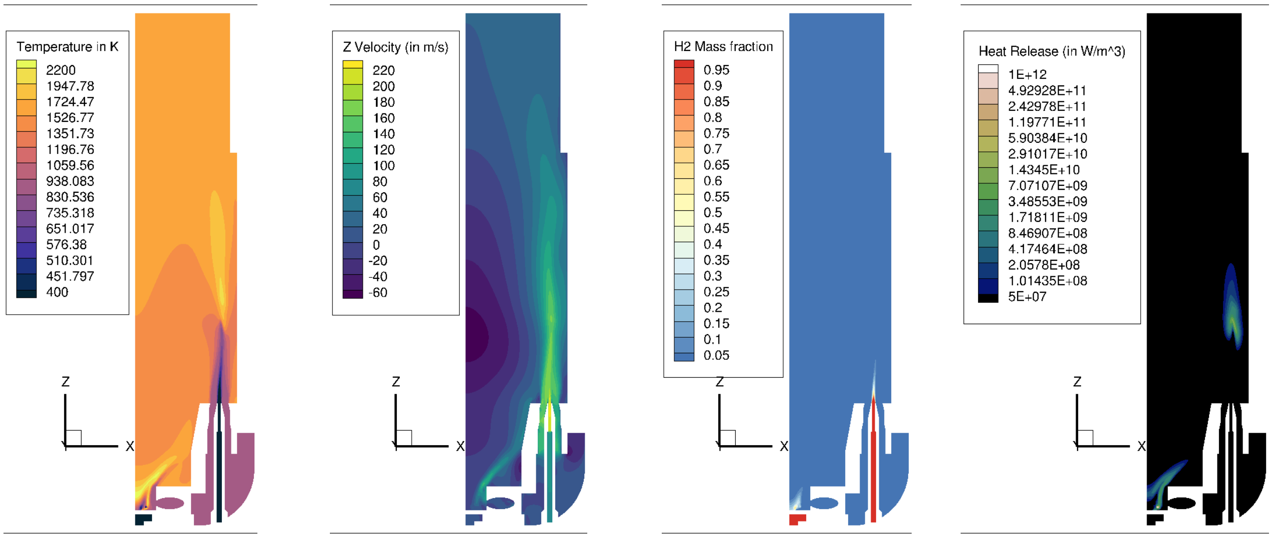

(a) Temperature (b) Z-velocity (c) H_2 Mass Fraction (d) Heat release

Figure 4.4.: Comprehensive evaluation of the flow characteristics: Temperature distribution, Z-velocity profile, H_2 mass fraction, and heat release profile.

The subfigures 4.4a to 4.4d illustrate different aspects of the flow and combustion. The velocity in the Z-direction(Figure 4.4b) allows assessment of the recirculation zone, while the temperature(Figure 4.4a) helps to locate temperature peaks. The hydrogen distribution 4.4c indicates the fuel distribution, providing insights into the reaction zone's position. The heat release(Figure 4.4d) depicts the flame's position and shape, with areas of highest heat release corresponding to the flame front.

4.2.4. Visualisation with OH*-chemiluminescence Images

Previous sections (4.2.1 to 4.2.3) introduced methods for assessing and verifying simulation results. Having demonstrated that the numerical setup shows good convergence behavior and the flow solution is physically accurate, the next step is to verify how precisely reality is depicted in the simulation. As mentioned in Section 3, OH*-chemiluminescence images are taken to determine the position and shape of the flame in an experimental setup [54]. The measured OH* radical, which forms in the reaction zone of the flame, can thus be compared with the experimental results (if available). In the OH*-chemiluminescence images, two flames positioned one behind the other are always observed due to the camera's position relative to the nozzle arrangement. Therefore, all OH* radicals within a specific measurement volume, as shown in Figure 3.2, are measured. To visualise these images it must be calculated for the specified measurement area. This involves creating an auxiliary zone in the shape and position of the measurement volume using the post-processing tool Tecplot 360 [145], and interpolating the flow solution data onto it (see Section 5.4 for more details). Subsequently, an integration of the individual slices of the auxiliary zone over the measurement direction/viewing direction of the camera (see Figure 3.2) is performed. This allows for the representation of the OH*-chemiluminescence of the entire measurement volume and comparison with the experimental results.

Figure 4.5 shows the integrated OH* chemiluminescence for the reference case. The coordinate system of the diagram is adapted to the combustion chamber's coordinate system.

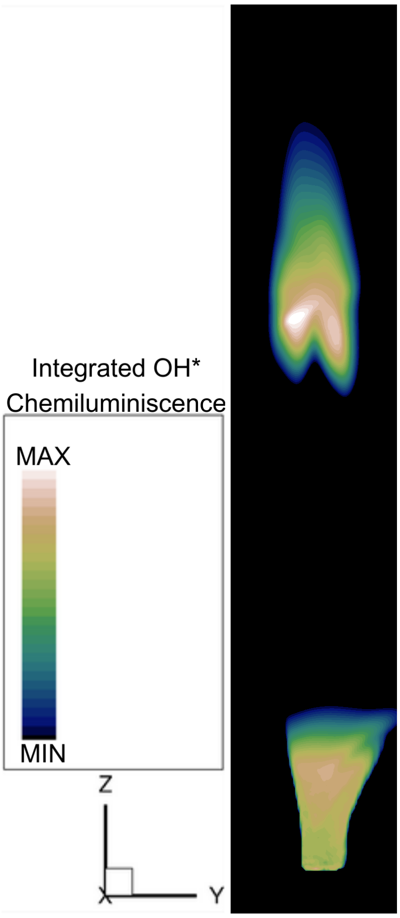

Figure 4.5.: Integrated OH*-chemiluminescence for the Reference Case

4.2.5. Calculation of the Heating Value

In addition to the optical evaluation of the OH*-chemiluminescence images, as discussed in previous sections (4.2.1 to 4.2.4), the heating value of the simulated combustion is calculated and compared with the actual value. The heating value is calculated based on the heat release within the entire combustion chamber.

The heating value is a material property that depends only on the properties of the species contained in the gas mixture and can then be calculated using the equation:

$$LHV = \frac{RH}{\dot{m}_{\text{fuel}}} \tag{4.1}$$

where RH represents the integrated heat release (can also be interpreted as Thermal Power), and $\dot{m}_{\text{fuel}}$ is the predefined fuel mass flow. A percentage deviation can be calculated in relation to the predefined heating value.

Additionally, by rearranging Equation (4.1) to $\dot{m}_{\text{fuel, calculated}} = RH/LHV$ and using the predefined heating value along with the calculated heat release value, the converted fuel mass flow $\dot{m}_{\text{fuel, calculated}}$ can be calculated. Comparing this with the set fuel mass flow at the fuel nozzles allows for the calculation of the percentage of fuel that is not converted in combustion and thus remains unburnt in the exhaust gas.

5. Numerical Simulation

The study conducted herein involves steady-state RANS simulations. The initial section of this chapter provides a detailed explanation of the underlying process. To select the most suitable turbulence and combustion models for this study, various modeling techniques were initially assessed and finally, a recommended approach is designed based on suitable methods and integrated into a numerical setup.

This chapter provides an overview of the models used in the numerical setup and the process of a simulation.

5.1. Simulation Process

The basis of every conducted simulation is a general framework into which various turbulence and combustion models can be integrated. In the framework, all further properties and basic settings of the numerical setup are stored. To achieve higher numerical stability of the steady-state RANS simulations, they are divided into sub-steps. To give an overview of the sequence of sub-steps, they are graphically represented in Figure 5.1.

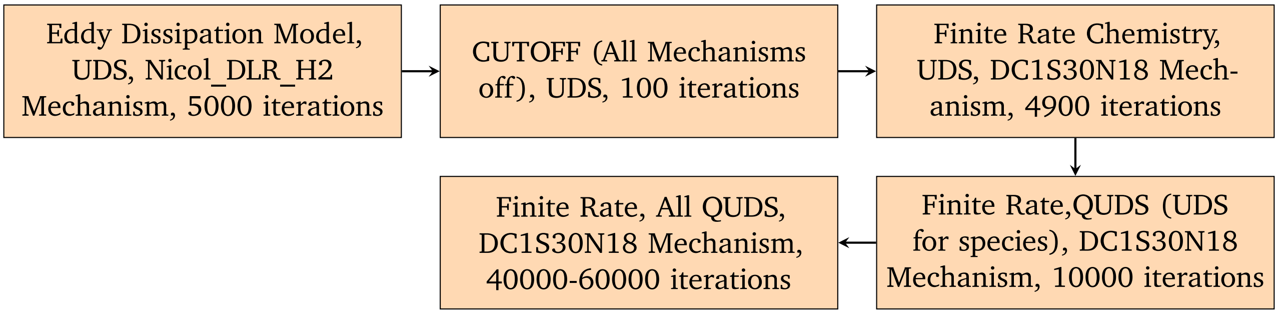

Figure 5.1.: Process flow of the CFD simulation steps.

Initially, general properties such as boundary conditions, reaction mechanisms, fuel and air mass flow rates, reference values, and the turbulence model are defined. Subsequently, settings for the solution methods are made. This includes, among other things, setting the relaxation factors, discretisation, and pressure-velocity coupling. Although a sufficient number of equations are available for determining the velocity and pressure components, all the sought variables appear in all equations. Therefore, they cannot be determined independently of each other, and the equation system is referred to as coupled. To address this, the **S**emi **I**mplicit **M**ethod for **P**ressure-**L**inked **E**quations (SIMPLE) algorithm [7] is used in this work. It is an iterative procedure with so-called pressure-velocity coupling. After solving the momentum equations, three additional steps, pressure correction, velocity correction, and mass flow correction, are performed [52].

The simulation begins with the **E**ddy **D**issipation **M**odel (EDM), using the first-order UDS for discretisation and the Nicol_DLR_H2 [42] mechanism for a total of 5000 iterations. This step establishes the initial conditions for the simulation.

The combustion process of Hydrogen is characterised by the following global reaction mechanism:

$$2H_2 + O_2 \rightarrow 2H_2O. \tag{5.1}$$

After the initial setup, the simulation enters a 'Cutoff' phase where all mechanisms are disabled. This phase lasts for 100 iterations and uses UDS. The rationale is to help achieve the detachment of the flame from the nozzle exit, which is often seen in the experiments.

The next phase reintroduces chemical reactions through the **F**inite **R**ate **C**hemistry (FRC) approach, utilizing the DC1S30N18 [135] mechanism and applying UDS to all equations for 4900 iterations.

Following that, the discretisation method is upgraded to a higher order QUDS for all equations, except for species which continue to use UDS. The DC1S30N18 mechanism is applied for a total of 10000 iterations.

In the final step, QUDS is employed for all equations along with the DC1S30N18 mechanism. This phase spans from 40000 to 60000 iterations, depending on the boundary conditions and the mesh refinement settings. While other physical properties converge in fewer iterations, the NO$_x$ emissions require a significant number of iterations to reach a constant value.

Each simulation is allocated a computing time (wall time) of 72 hours. If this limit is reached, the calculation is automatically terminated. No termination criterion is defined for the iterations, as the highest possible number of iteration steps is to be achieved.

5.2. Description and Selection of the Reference Case and Models Used for Simulating the ATM-Combustor

At the outset of this study, a suitable numerical setup was developed to most accurately represent the processes occurring within the combustion chamber. This involved conducting various simulations using different turbulence and combustion models. To facilitate a comprehensive comparison between the different approaches and with experimental results, all simulations were performed under identical boundary conditions. The reference operating point for these simulations was defined by the following parameters:

- Configuration: Jet-stabilised Main stage with a swirl-stabilised Pilot stage, without premixing.
- Thermal power: $80\,\mathrm{kW}$
- **L**ower **H**eating **V**alue (LHV): $120\,\mathrm{MJ\,kg^{-1}}$
- Air-fuel ratio λ: 4.5
- Fuel: Hydrogen
  - Mass flow rate: $0.668\,\mathrm{g\,s^{-1}}$ (of which $7\,\%$ is for the pilot stage)
  - Temperature: $298.15\,\mathrm{K}$ ($25\,^{\circ}\mathrm{C}$)
- Oxidiser: Air
  - Mass flow rate: $103\,\mathrm{g\,s^{-1}}$
  - Temperature: $873.15\,\mathrm{K}$ ($600\,^{\circ}\mathrm{C}$)

In the development of the numerical setup, the focus was primarily on evaluating various turbulence models and identifying the appropriate mesh refinement. Table 5.1 summarises the variations in the ATM-Combustor model configurations explored in this study. While selection of the Turbulence model is being discussed in Section 5.2.1. please refer to Section 5.3.1 for selection of appropriate Mesh.

Table 5.1.: Model variations of the ATM-Combustor.

Run	Turbulence Model	Computational Grid
01	Standard k-ε	Fine(Standard)
02	k-ω-SST	Fine(Standard)
03	k-ω-SST	Medium
04	k-ω-SST	Coarse

5.2.1. Selection of Turbulence model

For both turbulence models, meaningful solutions were obtained. It is important to note the following distinctions:

- The $k - \omega$ SST model did not achieve absolute convergence when switched to second-order schemes. Instead, it exhibited oscillatory convergence. In contrast, the standard $k - \varepsilon$ model was able to achieve absolute convergence in fewer iterations.
- Throughout the evaluation, simulations were also conducted using purely first-order schemes. Unfortunately, these simulations did not yield sensible NO_x emission values, despite achieving good convergence. Consequently, all simulations were eventually conducted using higher-order schemes for every equation.

As illustrated in Figure 5.2, following observations were made during the simulations:

1. While the flame lift-off height was similar for both the standard $k - \varepsilon$ and $k - \omega$ SST models, there was a noticeable difference in the shape and size of the flame and the recirculation zone.
2. The flame was slightly longer and narrower in the $k - \omega$ SST model compared to the standard $k - \varepsilon$ model.
3. The recirculation zone was also slightly larger in the $k - \omega$ SST model compared to the standard $k - \varepsilon$ model.
4. The reported NO_x emissions were very similar, with values of 2.4 ppm for the $k - \omega$ SST model and 2.35 ppm for the standard $k - \varepsilon$ model. (Note: While these are the raw values, the values used in Chapter 6 are as per the EU regulations [107])
5. The shape of the flame changed with each iteration, especially in the $k - \omega$ SST model.

As there is no experimental data to make the comparisons against, the decision to select the appropriate turbulence model was purely taken on the basis of the theoretical framework laid out in Section 2.2. As $k-\omega$ SST model performs better in near wall region, adverse pressure gradients and is also better when it comes to predicting flow separation and recirculation regions compared to standard $k-\varepsilon$, $k-\omega$ SST was finalised for rest of the simulations.

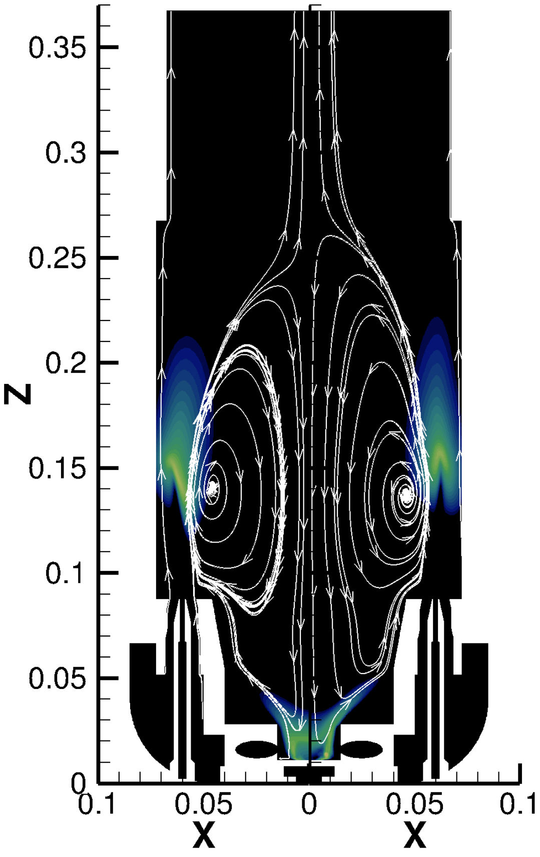

Figure 5.2.: Comparison of standard $k-\varepsilon$ (left) and $k-\omega$ SST models (right)

5.3. Computational Grid and Boundary Conditions

The computational grids necessary for CFD calculations are generated using ANSYS Meshing software [141]. Unstructured grids are utilised in this work due to their ability to be generated more quickly and efficiently for complex component geometries. As no measurement data necessary for detailed validation of simulation results, such as velocity fields or composition obtained through laser-based measurement methods, are available, the impact of structured or partially structured grids on the simulation outcomes is not considered in this study.

The computational grid for the atmospheric test rig, depicted in Figure 5.3, is locally refined in several areas to ensure an adequate number of cells across the nozzle cross-sections. Specifically, the reaction zone and fuel injection areas are meshed more finely than the rest of the fluid volume. The exit of the fuel nozzle is shown enlarged in Figure 5.3, displaying the stepped refinement of the grid towards the fuel nozzle exit. The wall transition is resolved across the entire volume with 15 prism layers of varying thicknesses, where the dimensionless wall distance y^+ is within the target value of 1. The grid for a 36°-segment for the first configuration (both, main and pilot stage are jet stabilised) consists of approximately 1.7 million grid nodes and 6.3 million elements while the grid for a 72°-segment for the second configuration (jet stabilised main stage with swirl-stabilised pilot stage) consists of approximately 3.5 million grid nodes and 12.3 million elements. The smallest elements in the vicinity of the fuel nozzle have an edge length of 0.2mm. Please refer to Section 5.3.1 for insights about Grid Study. All walls are considered adiabatic.

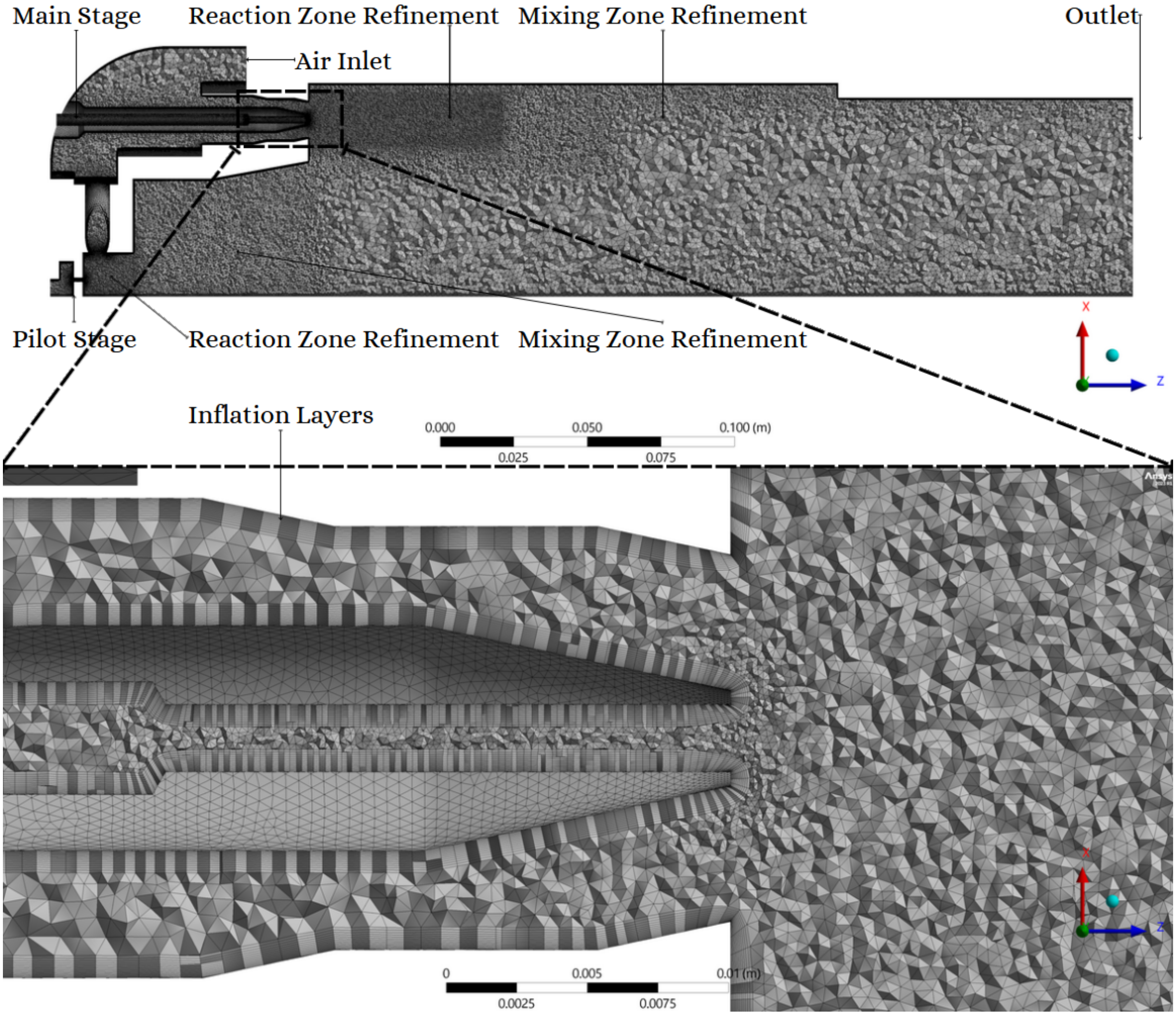

Figure 5.3.: Computational Grid for swirl-stabilised pilot stage - Overview and Refinement Regions. The visualization is done on a sectional plane that symmetrically cuts the nozzles along their axes.

5.3.1. Grid Study

In the generation of a discrete computational domain, a good compromise must be found between the necessary computational effort and a sufficiently high resolution to ensure stability, convergence, and accuracy of the simulations [43]. If the grid is too coarse, the scales of the reacting flow field cannot be adequately resolved, and if the grid is too fine, the computation times would be too long. As part of a grid study following Celik et al. [73] and Rumsey and Thomas [77], the influence of grid resolution on the simulation and the resulting discretisation error for three grids of different fineness is estimated. The key sizes of the three discretisations considered for the grid study are summarised in Table 5.2. From these values, refinement factors of $r_{21} = 1.12$ and $r_{32} = 1.2$ are derived. According to Celik et al. [73], these two refinement factors r_{21} and r_{32} should be approximately 1.3. However, this would have lead to extremely large 'fine' grid and resulted in a very computationally intensive and expensive grid study. This recommendation by Celik et al. [73] is based on empirical values and not on a formal derivation [73]. Therefore, the compromise of smaller refinement factors is accepted.

Index i	Grid	Node Count K_i	Cell Count N_i
1	Fine	3.5M	12.3M
2	Standard	2.5M	8.8M
3	Coarse	1.6M	5.1M

Table 5.2.: Characteristic parameters of the grids considered for the study.

	Temperature (in K)	NO$_x$ (ppm)
ϕ_3	1465.9	2.05
ϕ_2	1466.17	2.41
ϕ_1	1453.02	4.53
ϕ_{21}^{ext}	1465.87	1.86
e_{21}^{a}	0.018 %	17.5 %
GCI_{21}^{fine}	0.19 %	11.5%

Table 5.3.: Grid Convergence Index (GCI) [73, 77] of various parameters ϕ.

From these sizes, along with the refinement factors r_{21} and r_{32}, the necessary extrapolated values ϕ_{21}^{ext}, the approximate relative errors e_{21}^{a}, and the grid convergence index GCI_{21}^{fine} are calculated. The equations by Celik et al. [73] and code for calculation are given in the appendix. The mentioned compromise to smaller refinement factors of about 1.18 leads, according to these calculation equations, to somewhat higher grid convergence indices GCI_{21}^{fine} for the parameters listed in Table 5.3,especially for NO$_x$ emissions. Since the values of these grid convergence indices are around lower two-digit percentage range despite smaller refinement factors, the standard grid can be evaluated as sufficiently discretised according to the method by Celik et al. [73].

From the values in Table 5.3 and the calculation of the grid convergence indices GCI_{21}^{fine}, it emerges that while outlet temperature displays low sensitivity to the grid size, the NO$_x$ emissions seem to be very dependent on it. However, further refining the grid was not practical as it lead to very high processing times per iteration, required setting very-low under-relaxation factors and thus also required a very large number of iterations for convergence as a result. Hence, 'Fine' grid was chosen as the standard choice for further simulations.

5.4. Post-processing

The CFD simulations were evaluated using Tecplot 360 [145] software from Tecplot Inc. To assess flow characteristics across a section (see Figure 4.4) and recirculation (see Figure 6.5), a section plane perpendicular to the XY plane, cutting symmetrically through the pilot stage nozzle and the main stage nozzle, was constructed. Relevant contours were then plotted. The Z-axis represents the flow direction.

To analyze velocity magnitude variation downstream, the magnitude of velocity was calculated using $V = \sqrt{u^2 + v^2 + w^2}$. A probe line parallel to the Z-axis, passing through the center of the main stage nozzle, was created. Velocity magnitude was plotted along this line. Swirl (as depicted in Figure 6.15) was shown using a section plane parallel to the XY plane located $30\,\mathrm{mm}$ from the exit of the fuel inlet pilot stage. Velocity magnitude contours were plotted over this plane.

For calculating Lower Heating value and Mass flow rate (as shown in Figure 6.4 for example); first, thermal power/integrated heat release (RH) was obtained by, as the name suggests; integrating heat release over the fluid volume. Then, Lower Heating value and mass flow rate were calculated based on the formula provided in Section 4.2.5. NO_x emissions and the averaged outlet temperature were evaluated by performing mass flow weighted averaging on the outlet surface. The values for NO_x emissions were subsequently standardised and normalised according to the equations described in Section 6.1.5.

To evaluate and represent OH*-chemiluminescence (for example, see Figure 6.1), a new parameter called ’OH_mult’ was created by multiplying the mass fractions of oxygen (O) and hydrogen (H). Since OH*-chemiluminescence is a line-of-sight measurement, a cuboid with dimensions $100\,\mathrm{mm}\ \times 40\,\mathrm{mm}\ \times 220\,\mathrm{mm}$ was initially constructed. Measurements within this volume were then interpolated onto the XZ plane, considering that the line of sight was along the Y-axis. The flame liftoff height was determined by measuring the difference between the base of the flame and the exit of the air inlet nozzle. Although the flame of the pilot stage is not visible in the Line of Sight measurements conducted during the experiments, it is still detected within the defined zone and is consequently presented within this study. Additionally, while the Line of Sight (LoS) measurement in principle captures both the flames, including one positioned directly behind the other (refer to Figure 3.2), the study solely examines the single flame closest to the camera. Due to the lack of experimental data, this approach aims to better understand the flame characteristics, including shape and liftoff height.

For plotting purposes, Python [144] programming lanugage was utilised with the assistance of third party libraries.

6. Discussion and Results

This chapter has been divided into two sections; one for the configuration where both the main and pilot stages are jet-stabilised, and the second section for the configuration where we have the swirl-stabilised pilot stage. Each of the sections is further divided into multiple subsections as follows:

OH* Chemiluminescence and visualisation: This section aims to qualitatively and quantitatively assess the integrated OH* chemiluminescence visualisations. The main focus of this section is to observe the effect of variations in the air-fuel ratio (λ) and the configuration geometry on flame shape and liftoff height.

Calculation of the Lower Heating Value and the mass flow rate of the fuel: This section focuses on calculating the **L**ower **H**eating **V**alue (LHV) and mass flow rate, as described in Section 4.2.5, to cross-verify how closely the simulation results and the calculated thermal power align with the expected values.

Recirculation and velocity profiles: This section visualises the recirculation zones and examines the impact of configuration geometry and λ on the size of these zones. It also discusses the variation in velocity magnitude along a line passing through the center of the main stage nozzle and towards the outlet of the combustor. Furthermore, it analyses and explains the trends in velocity magnitude along this probe line.

Outlet temperature: This section focuses on how the outlet temperature changes with respect to the equivalence ratio.

NO$_x$ emissions: This section focuses on the impact of combustion chamber geometry and air-fuel mixture on NO$_x$ emissions. The plots and explanations, however, have been presented with respect to the adiabatic flame temperature, as discussed in Section 3.2.1.

6.1. Configuration 1: Jet-stabilised Main and Pilot stage

6.1.1. OH*-chemiluminescence visualisations

From the diagrams of the integrated OH* chemiluminescence along the Line of Sight (LoS), not only can a statement be made about the shape and lift-off height of the flame, but also a comparison with the experimental data can be conducted (if and when the results are available). Even though the experiments have not been set up to visualise the pilot stage flame, these flames have been depicted here in the simulation results.

The air-fuel ratio (λ) is increased from $\lambda = 2.5$ in six steps to $\lambda = 5$.

Variant 1: Premixed Length = 30mm

As evident in Figure 6.1, the intensity and the length of the flame seem to decrease as we gradually increase the λ from 2.5 to 5. However, the lift-off height increases linearly with respect to λ. This is explained by the fact that λ is directly proportional to the air mass flow rate and, since the fuel mass flow rate is constant across all the simulations, the linear increase in air mass flow rate/momentum translates to the linear increase in the flame lift-off height. The lift-off height has been quantified and plotted in Figure 6.3.

The base of the flame exhibits an inverted ”V” shape, with the angle becoming more and more acute as we increase the λ. Also, when referring to the overall flame shape, one can observe that the flame is not symmetric, especially for the lower λ values. The right portion of the flame appears significantly taller than the left one. However, the flame becomes more and more symmetric and resembles an isosceles triangle as we move towards leaner compositions, i.e., higher λ values.

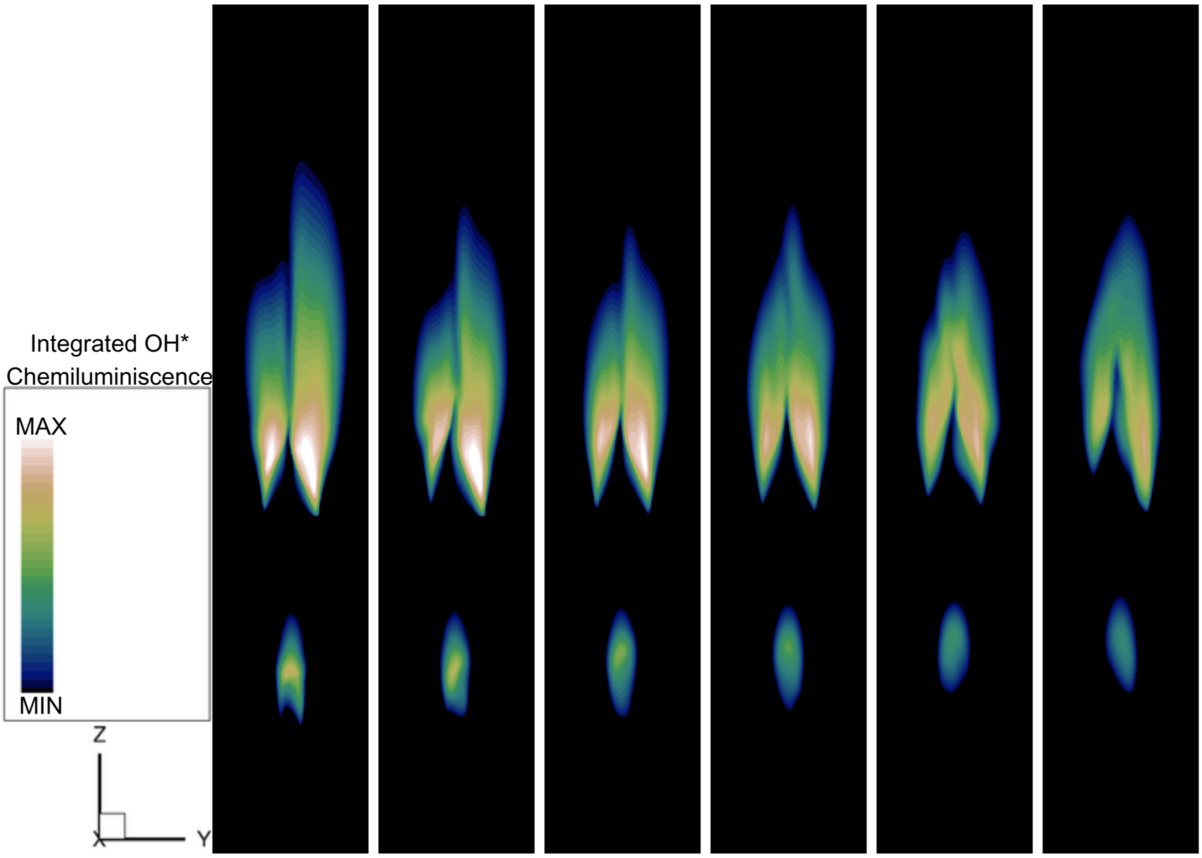

Figure 6.1.: OH*-chemiluminescence visualisation in the Jet-Stabilised Pilot stage configuration, premixed variant with respect to the air-fuel ratio (λ). The asymmetric flame and the inverted ”V” pattern for the base of the flame are evident for this variant

The pilot stage also exhibits a reduction in intensity and a slight increase in the lift-off height. While the base of the flame resembles an inverted ”U” pattern for $\lambda = 2.5$, it does not exhibit a similar pattern for the rest of the compositions.

Variant 2: Non-Premixed

As seen in Figure 6.2, similar to the Premixed case, a decrease in intensity and flame height is observed as we gradually increase the λ from 2.5 to 5. The lift-off height also shows an increase in a linear fashion.

As per the expectations, the lift-off heights seem to be considerably higher compared to the Premixed case. Another stark difference is observed in the shape of the base of the flame, which now exhibits an inverted ”U” pattern instead of the inverted ”V”. In addition to the shape of the base of the flame, the top of the flame also showcases a unique pattern, as it resembles a checkmark (✓) for the richer composition and it eventually flattens out as we move towards the leaner compositions.

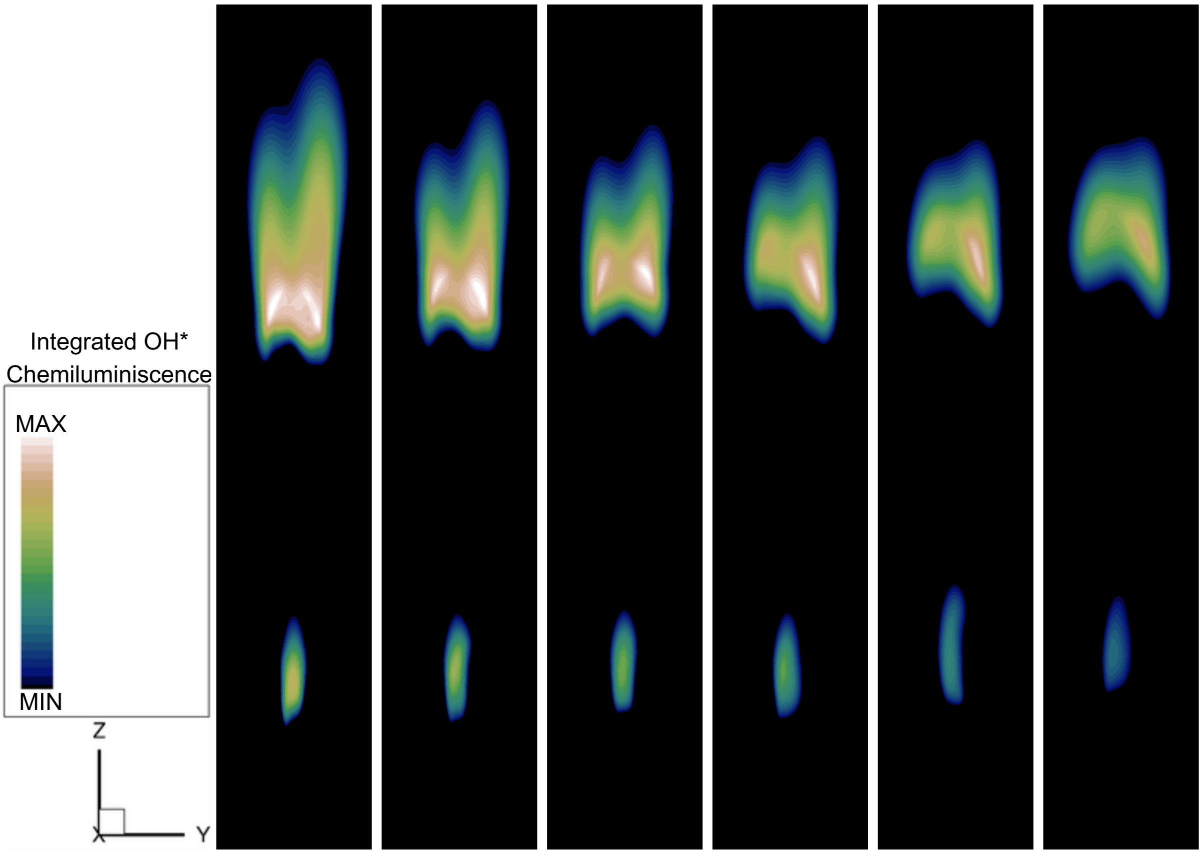

Figure 6.2.: OH*-chemiluminescence visualisation in the Jet-Stabilised Pilot stage configuration, non-premixed variant with respect to the air-fuel ratio (λ). Notable differences include the inverted ”U” pattern at the flame base and the transition of the flame top from a checkmark to a flattened shape with leaner mixtures

The pilot stage does show a slightly different pattern, and the base does not really have an inverted ”U” pattern. However, the flame length appears significantly longer and thinner for $\lambda = 4.5$.

In both variants, we can see that, for $\lambda = 2.5$, the flame height is considerably larger compared to the rest of the fuel compositions.

While flashbacks are expected, especially for Premixed configurations running on pure hydrogen combustion, no such phenomenon was observed via the simulations.

Comparison of Flame Lift-Off Heights

As depicted in Figure 6.3, the flame lift-off height increases linearly with respect to λ. For the Premixed case, the lift-off height linearly increases from $19.3\,\mathrm{mm}$ for $\lambda = 2.5$ to $28.3\,\mathrm{mm}$ for $\lambda = 4.5$, but it sees a sudden jump for $\lambda = 5$. For the Non-Premixed case, the increase is linear throughout, from $44.9\,\mathrm{mm}$ for $\lambda = 2.5$ to $62\,\mathrm{mm}$ for $\lambda = 5$. The average difference between the lift-off heights for these two configurations for any given λ is about $26.4\,\mathrm{mm}$, which aligns well with the expectations.

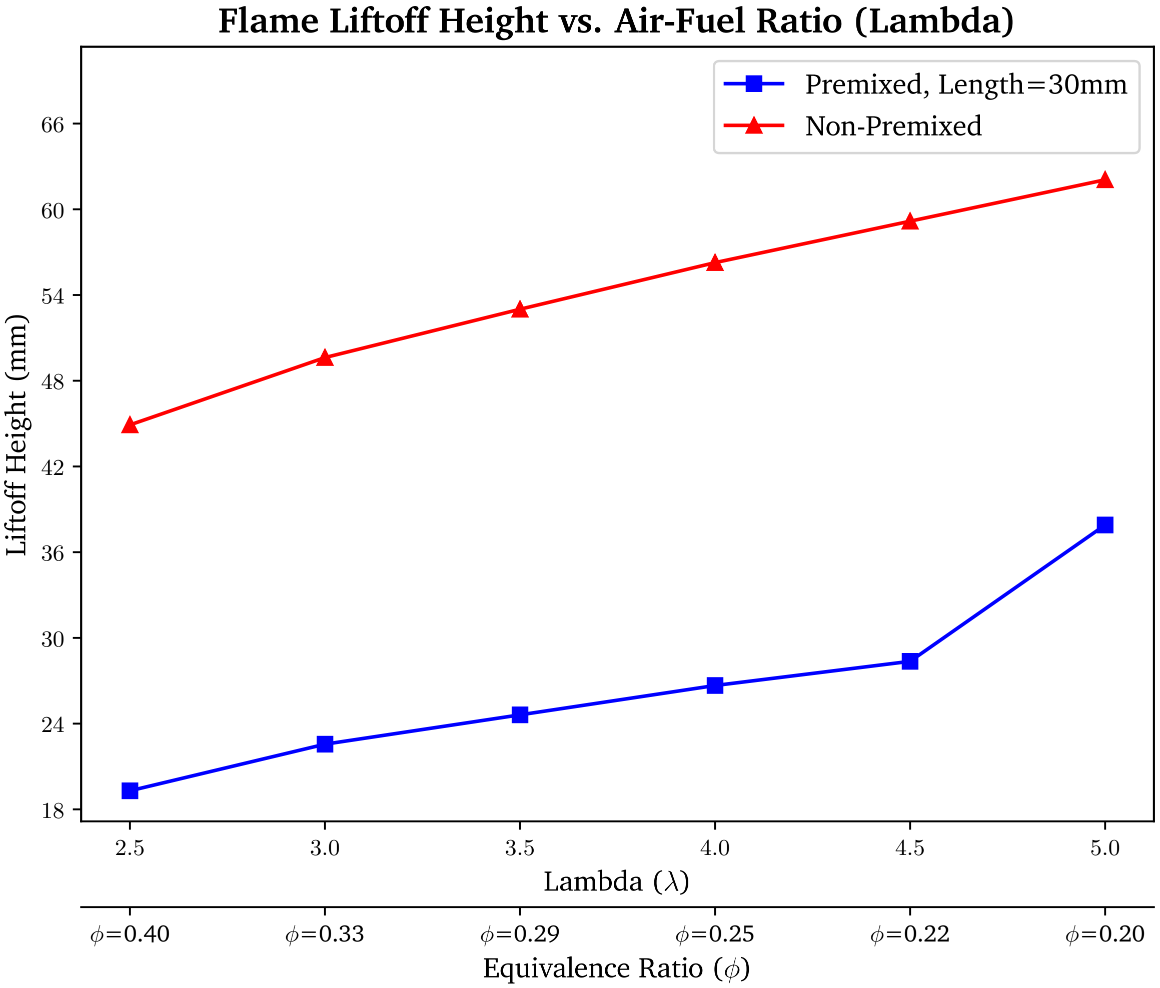

Figure 6.3.: Variation of flame lift-off height with air-fuel ratio (λ) for the Jet-Stabilised Pilot stage, demonstrating the sudden jump in height for $\lambda = 5$ for the premixed variant.

6.1.2. Calculation of Lower Heating Value and Mass Flow Rate

In addition to evaluating flow visually, as discussed in Section 6.1.1, the quality of the simulations can also be assessed by looking at the deviations in the Lower Heating Value (LHV) and the calculated fuel mass flow rates. For this purpose, in Figure 6.4, the top left Figure a shows the Lower Heating Value plotted against the equivalence ratio (ϕ) and the top right Figure b shows the calculated fuel mass flow rate plotted against the Equivalence Ratio (ϕ). However, since the variation in the boundary conditions was done by changing the mass flow rate of the air, keeping the air-fuel ratio (λ) in mind, the values for (λ) have also been mentioned on the secondary x-axis.

The bottom image of Figure 6.4 describes the deviation (in %) for both, the Lower Heating Value and the calculated fuel mass flow. Equation (4.1) makes it evident that the deviation (in %) for both these parameters is the same.

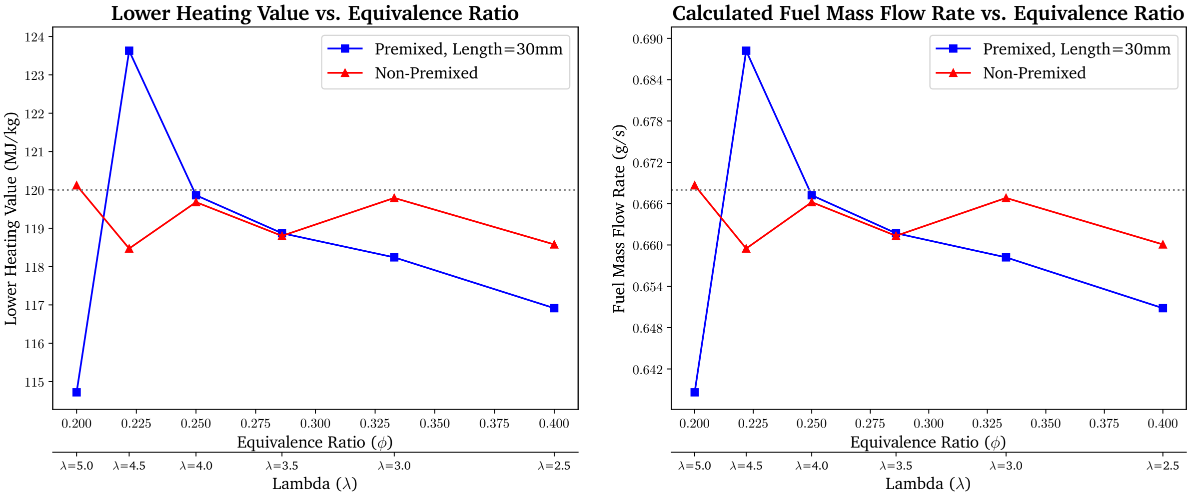

(a) LHV vs ϕ

(b) Calculated fuel mass flow rate vs ϕ

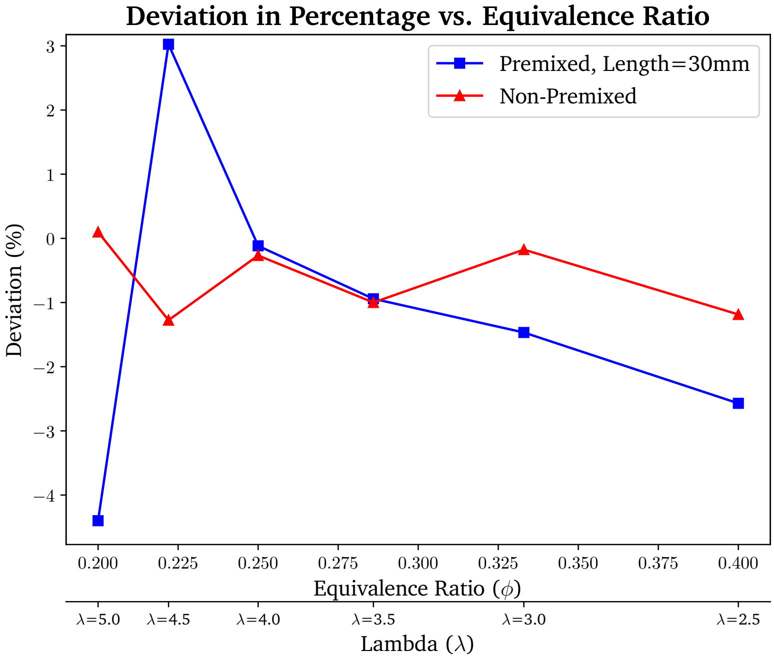

(c) Deviation in LHV and calculated fuel mass flow rate vs ϕ

Figure 6.4.: Comparative analysis of Lower Heating Value (LHV) and mass flow rate across different equivalence ratios (ϕ) for Jet-Stabilised Pilot stage.

For the premixed variant, the maximum magnitude of deviation is 4.4% and the rest of the deviations are between 0.8% to 3%. In the case of the non-premixed variant, the results are even better as the maximum deviation observed was 1.2%. However, in both configurations, the deviations are small enough to conclude that the simulations were sufficiently accurate and also small deviations at both the highest and lowest air-fuel ratios (λ) also reinforce the larger operating range, in terms of air-fuel compositions for hydrogen in [137].

6.1.3. Recirculation and Velocity profiles

Variant 1: Premixed Length = 30mm

The sequence of images displayed in Figure 6.5 provides a visual representation of the recirculation zone, in the form of streamlines and the axial/downstream velocity, in the form of contours. All the visualisations are done on a 2D section plane which is parallel to the combustion chamber downstream axis and which cuts symmetrically through both, one of the main stage nozzles and the pilot stage nozzle. Each of the six images corresponds to a discrete value of λ, beginning from 2.5 and incrementing by 0.5 up to a λ of 5, from left to right.

Recirculation is important in the context of flame stabilisation, lowering peak temperatures, promoting effective mixing of hot combustion products with the incoming reactants which in turn promotes ignition and continuous combustion.

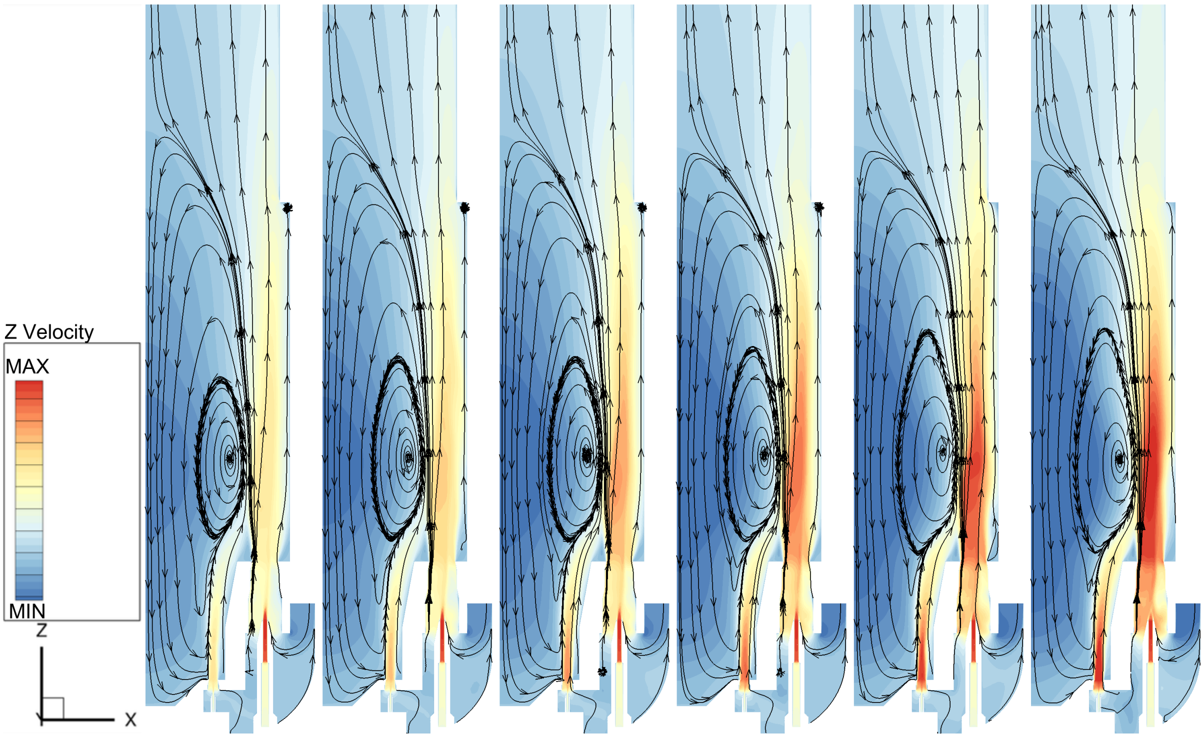

Figure 6.5.: Flow field characteristics in a premixed jet-stabilised configuration, showcasing the effect of air-fuel ratio (λ) on recirculation zones and axial velocity near the nozzle exit.

As λ increases, one can see an increase in the axial velocity component, especially near the exit of the air nozzle, which aligns with the expectations as λ can only be varied by altering the air mass flow rate for a fixed geometry and fuel mass flow rate.

While the height of the vortex center, or the ”eye” of the recirculation zone remains fairly consistent; independent of λ; the maximum extent of the recirculation zone seems to exhibit a decreasing trend as we increase the leanness of the mixture. This behaviour can be possibly attributed to the increased air flow at higher λ values, which reduces the extent of flow reversal. However, all of the recirculation zones extend beyond the ’step’ of the combustion chamber.

To quantitatively evaluate the velocity profile along downstream, a probe line was constructed which starts from the center of the Main stage fuel and ends at the combustion chamber outlet, running parallel to the downstream axis. Since the Main stage Air inlet nozzle surrounds the Main stage fuel inlet nozzle and is concentric, the probe line also passes through the center of it. The velocity magnitude was obtained using the relation $V = \sqrt{u^2 + v^2 + w^2}$ and the values were then plotted against the points present on this line for each air-fuel ratio (λ), which gives us plots similar to Figure 6.6. The locations of nozzle exits and the outlet have been marked in the Figures accordingly.

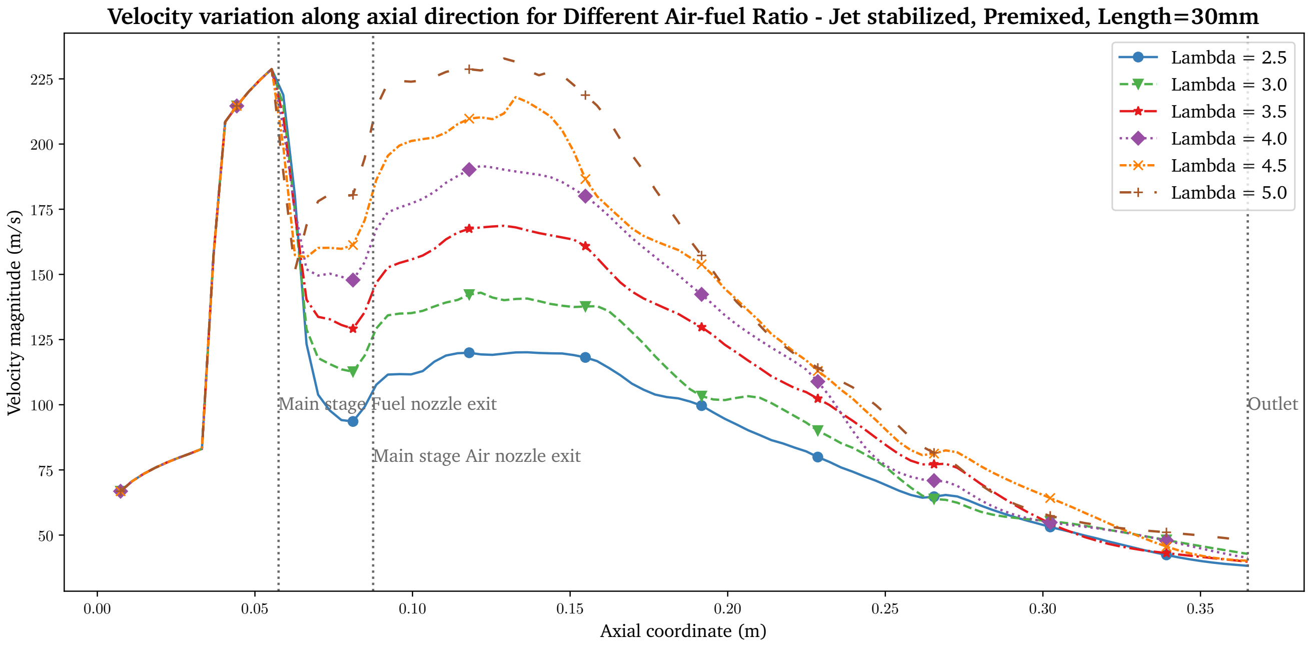

Figure 6.6.: Velocity magnitude variation in a premixed, jet-stabilised pilot stage configuration along the defined probe line, showing the differences in velocity peaks and trends for various air-fuel ratios (λ).

As seen in Figure 6.6, the velocity within the Main stage fuel nozzle reaches a maximum of $228.7\,\mathrm{m\,s^{-1}}$ for all air-fuel ratios λ when it encounters a decrease in the cross-sectional area. Subsequently, it decreases to a lower value in the premixing region, which refers to the region between the exit of the fuel nozzle and the exit of the air nozzle. However, the magnitude of this decrease varies depending on the specific value of λ. The lowest velocity in the premixing region is observed when $\lambda = 2.5$, with a value of $V = 93.6\,\mathrm{m\,s^{-1}}$. Additionally, the increase in the lowest velocity within this region follows a generally linear trend until $\lambda = 4$, with a slope of $34\,\mathrm{m\,s^{-1}}$ per λ. However, for $\lambda = 4.5$ and 5, the plot exhibits a sudden deviation $10\,\mathrm{mm}$ downstream from the exit of the fuel inlet nozzle. Furthermore, it also experiences a secondary inflection at a distance similar to that of other λ values, where the flow begins to accelerate again. In these cases as well, the velocity follows the same linear trend and slope. The linear trend is expected as λ can only be varied by altering the air mass flow rate and for constant cross-sectional area and density, the velocity is directly proportional to the velocity.

The velocity undergoes acceleration as the air-fuel mixture heats up and eventually undergoes combustion. Here, we observe a region that resembles a plateau with a relatively blunt peak, approximately corresponding to the location of the base of the flame. Moreover, the maximum velocity attained in this region increases linearly as the value of λ increases. Specifically, the velocity ranges from $120\,\mathrm{m\,s^{-1}}$ for $\lambda = 2.5$ to $232.8\,\mathrm{m\,s^{-1}}$ for $\lambda = 5$, with a slope of $45.1\,\mathrm{m\,s^{-1}}$ per λ. An exception to this trend is observed for $\lambda = 4.5$, where a sharp peak is observed in this region.

Subsequently, the velocities exhibit a decreasing trend all the way to the outlet, with the final exit velocity ranging from $38\,\mathrm{m\,s^{-1}}$ to $46\,\mathrm{m\,s^{-1}}$. Despite the linear variation, the values in this range are quite close to each other.

Variant 2: Non-Premixed

Similar to the Premixed variant (See Section 6.1.3), Figure 6.7 displays the flow field characteristics within a jet-stabilised combustor configuration devoid of premixing, across a spectrum of air-fuel ratios (λ). These visualisations are also arrayed in ascending order of λ from 2.5 to 5, advancing from left to right.

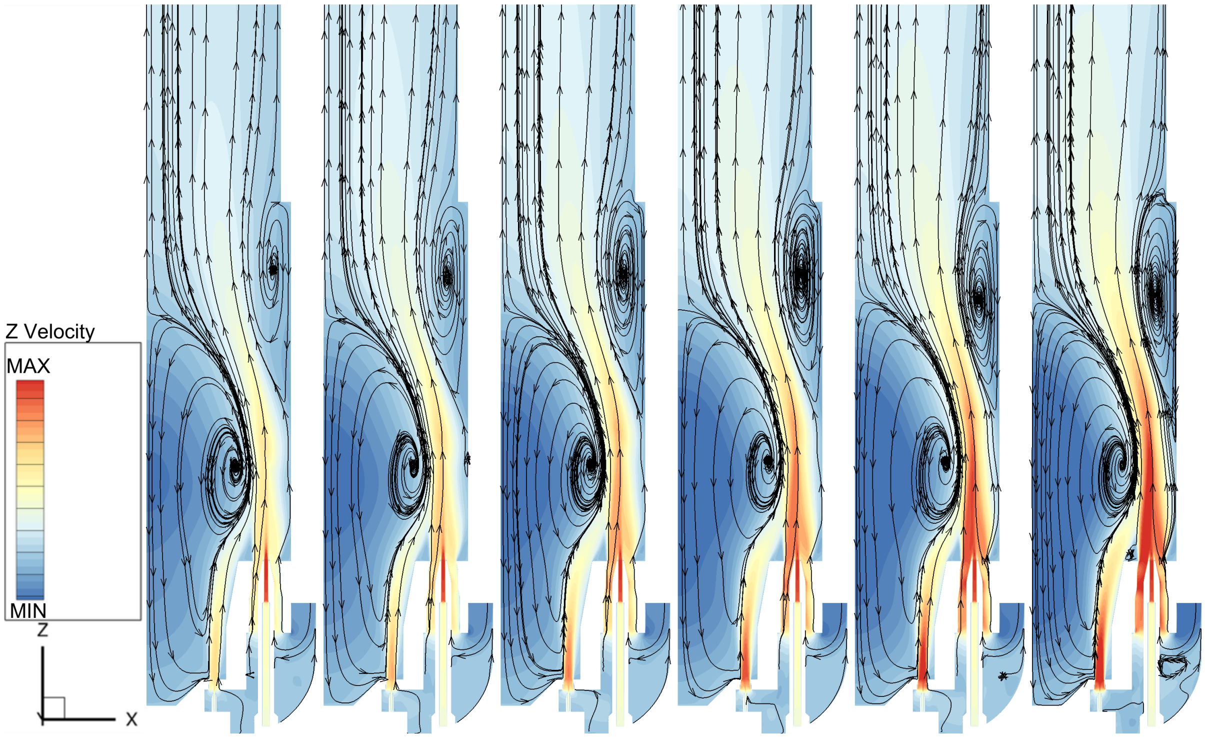

Figure 6.7.: Flow field characteristics in a non-premixed jet-stabilised configuration, showcasing the effect of air-fuel ratio (λ) on recirculation zones and axial velocity near the nozzle exit.

Here too, we see an increase in the axial velocity in the vicinity of the nozzle exit as we increase the value of λ. However, unlike the Premixed variant where the maximum extent of the recirculation zone was decreasing in the order of increasing λ, here we see the recirculation zone propagating in the downstream direction as we increase the leanness of the composition while the vortex center/eye of the zone still maintaining the same height across all λ.

It is also worth noting that while the size of the primary/inner recirculation zone is generally much smaller for every λ of its corresponding premixed counterpart, we see an emergence of a secondary/outer recirculation zone with its vortex center being close to the step of the combustion chamber. A possible explanation to this can be that the flow here is much more stratified compared to the premixed configuration while entering the combustion chamber and this inhomogenity might lead to different effects in the flow field. Here, similar to the primary recirculation zone, the size of this recirculation zone increases as the λ increases. In fact, for $\lambda = 3.5$ and above, we see the extent of the zone going beyond the step and the step causing a small pinch at the top in the secondary recirculation zone.

Similar to Figure 6.6, Figure 6.8 illustrates the variation of velocity magnitude along the defined probe line. The details about the construction of the probe line have already been mentioned in Section 6.1.3. In this case, the velocity rises up to $228.7\,\mathrm{m\,s^{-1}}$ near the Main stage fuel nozzle exit. The only difference is the location at which this peak is observed, since this configuration does not have pre-mixing.

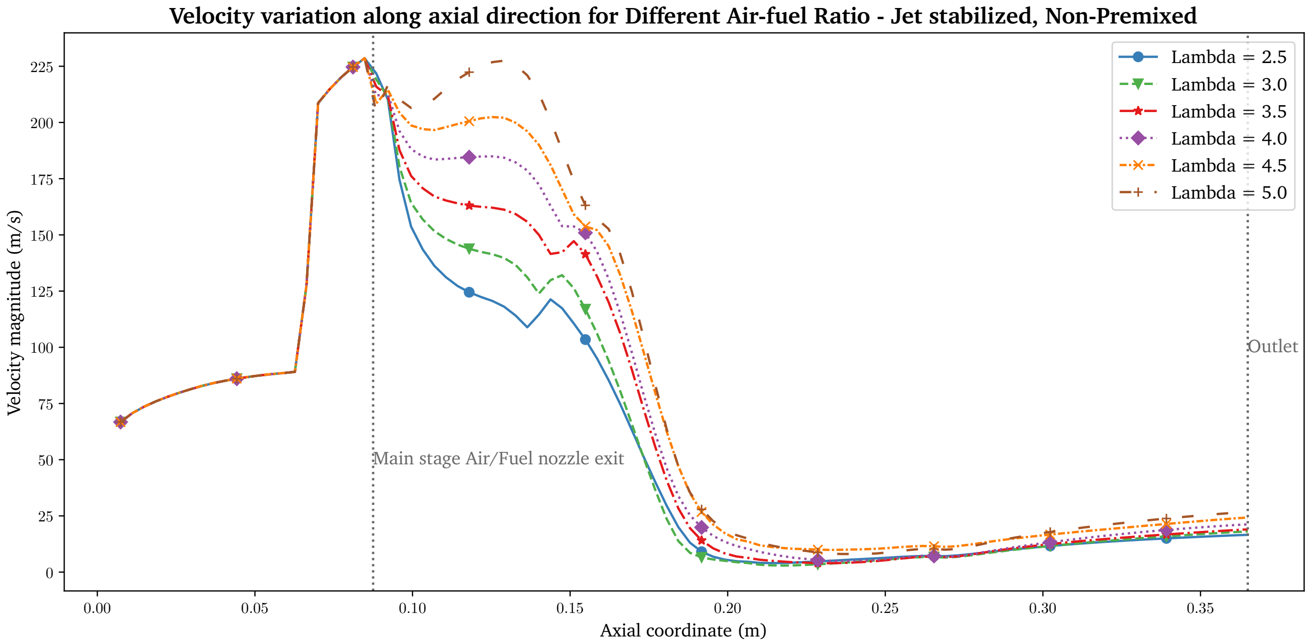

Figure 6.8.: Velocity magnitude variation in a non-premixed, jet-stabilised pilot stage configuration along the defined probe line, showing the differences in velocity peaks and trends for various air-fuel ratios (λ).

To study the velocity trends after exiting the nozzle, the plot needs to be divided into two cases: one for $\lambda = 4.5$ and 5, and the other case for $\lambda = 2.5, 3, 3.5$, and 4. This division is necessary because, in the former case, there is a minor increase in velocity after a slight decrease upon exiting the nozzle, followed by a peak. The velocity then follows a decreasing trend. In the latter case, the velocity shows a decreasing trend until a sharp, small peak is observed downstream, roughly corresponding to the base of the flame. After the peak, the velocity continues to decrease. Such a sharp peak is not observed for $\lambda = 4.5$ and 5, and only a minor inflection is observed at this point. One of the possible reasons why we see an initial peak for $\lambda = 4.5$ and 5 is because this location also corresponds to the region where both, the air and fuel seem to be mixed well enough in the context of temperatures as well as the velocities.

One notable aspect of this plot is that the velocity decrease is sharp, reaching its minimum value roughly halfway downstream and not at the outlet. The minimum velocity ranges from $4\,\mathrm{m\,s^{-1}}$ for $\lambda = 2.5$ to $8\,\mathrm{m\,s^{-1}}$ for $\lambda = 5$. After reaching the minimum, the velocity increases modestly in a logarithmic sense, with outlet velocities ranging from $16.7\,\mathrm{m\,s^{-1}}$ to $26.7\,\mathrm{m\,s^{-1}}$. This trend can be explained by the fact that the probe line passes through the secondary recirculation zone, and the location where the lowest velocities are observed is very close to the vortex center of the recirculation.

6.1.4. Outlet Temperature

In the design of a combustion chamber, it is crucial to have a thorough understanding of the temperatures at the outlet. While outlet temperatures alone do not provide definitive insights, analysing the trend of outlet temperatures across a range of equivalence ratios can offer preliminary understanding of combustion efficiency and NO_x emissions. Furthermore, this analysis can aid in making informed decisions regarding the design and operating range of the combustion chamber, specifically in terms of determining an acceptable thermal load for the specific configuration.

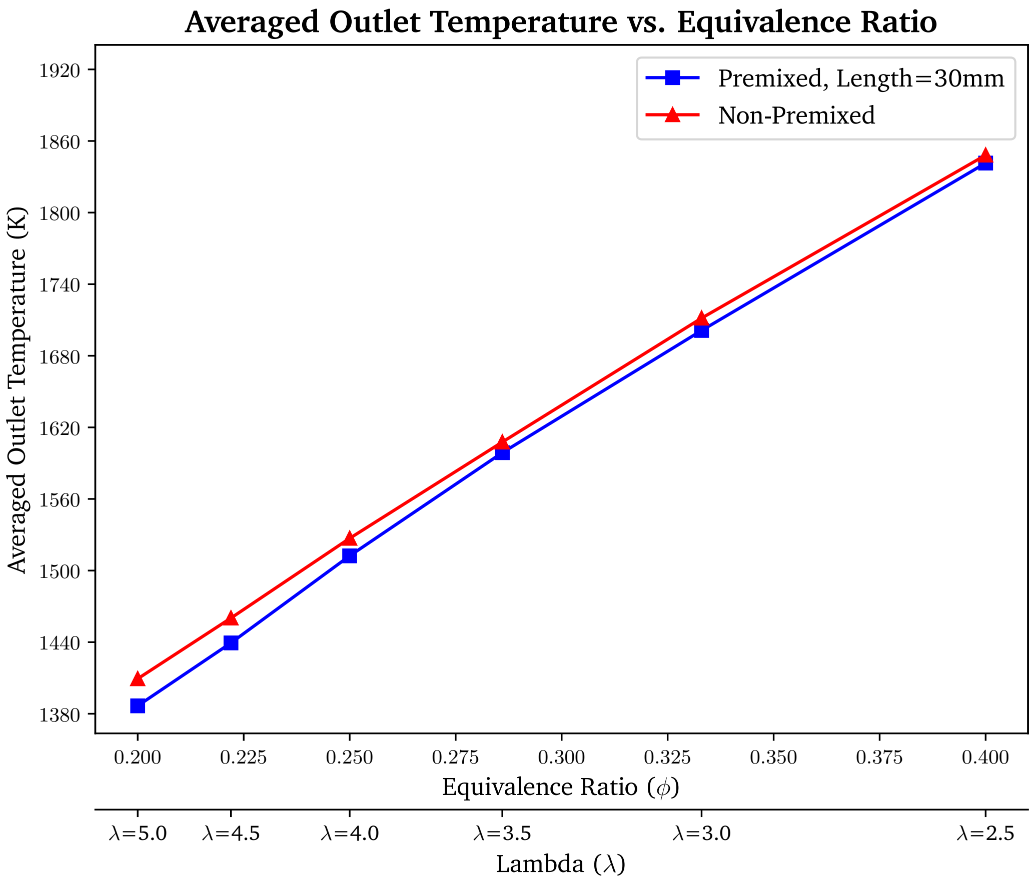

Figure 6.9.: Insights into the variation of average outlet temperature in relation to equivalence ratio (ϕ) for jet-stabilised pilot stage variants. The figure demonstrates a progressive increase in outlet temperature with the equivalence ratio and highlights differences between premixed and non-premixed configurations at leaner compositions.

Figure 6.9 provides valuable insights into the variation of the average outlet temperature in relation to the equivalence ratio ϕ for both variants of the jet-stabilised main and pilot stage configuration. The temperatures have been obtained by averaging over the surface of the outlet using a mass-flow weighted average method. Since the simulations were run by incrementing the air-fuel ratio λ, an additional secondary x-axis for λ has been provided.

As the equivalence ratio increases, both variants exhibit a progressive increase in outlet temperature. However, the non-premixed variant consistently shows slightly higher outlet temperatures at equivalent equivalence ratios.

At the lowest equivalence ratio of 0.2, the difference in outlet temperatures between the premixed ($1386.6\,\mathrm{K}$) and non-premixed ($1409.3\,\mathrm{K}$) configurations is most noticeable. This difference decreases as the equivalence ratio increases, with the premixed and non-premixed temperatures coming close to each other at an equivalence ratio of 0.4 (premixed at $1841.4\,\mathrm{K}$ and non-premixed at $1848.1\,\mathrm{K}$). This convergence suggests that the influence of the mixing process on combustion temperature becomes less significant as the mixture becomes richer.

6.1.5. NO$_x$ Emissions

Before starting with the discussion of NO$_x$ emissions, the standardisation and normalisation of these emissions are crucial for ensuring comparability across different combustion processes and compliance with regulatory standards. The process involves converting NO$_x$ emissions to a dry basis and normalising them to a standard oxygen concentration. The calculation for dry air is based on the principle that the water is removed from the sample to analyse and measure the amount of produced NO$_x$ [40, 143].

The conversion of NO$_x$ emissions from a wet basis to a dry basis is represented by the equation:

$$\mathrm{NO}_{x\mathrm{dry}} = \mathrm{NO}_{x\mathrm{measured}} \times \left(\frac{100}{100 - (\mathrm{H_2O})_{\mathrm{percentage}}} \right) \tag{6.1}$$

where $\mathrm{NO}_{x\mathrm{dry}}$ is the dry basis NO$_x$ concentration, $\mathrm{NO}_{x\mathrm{measured}}$ is the measured NO$_x$ concentration on a wet basis, and $(\mathrm{H_2O})_{\mathrm{percentage}}$ is the percentage of water vapor in the exhaust gas.

For stationary gas turbines, the NO$_x$ measurements are further corrected to 15% O$_2$ [40]. To normalise the NO$_x$ emissions to 15% O$_2$, the following formula is used:

$$\mathrm{NO}_{x\mathrm{normalised}} = \mathrm{NO}_{x\mathrm{dry}} \times \left(\frac{21 - \mathrm{O}_{2\mathrm{reference}}}{21 - \mathrm{O}_{2\mathrm{measured}}} \right) \tag{6.2}$$

Here, $\mathrm{NO}_{x\mathrm{normalised}}$ is the NO$_x$ concentration normalised to 15% O$_2$, $\mathrm{O}_{2\mathrm{reference}}$ is the reference oxygen concentration, and $\mathrm{O}_{2\mathrm{measured}}$ is the actual oxygen concentration measured in the exhaust gas.

The calculated NO$_x$ emissions should be checked for meeting the European Union regulation regarding produced NO pollutant [143]. This regulation states that for gaseous fuels other than natural gas (since we are using Hydrogen), current legislation is 200 mg/Nm^3 for existing gas turbines and 75 mg/Nm^{3}for new gas turbines [107]. To validate the produced NO$_x$, the measurement for legislation has to be converted to ppm [143]. This can be done using the following equation [68]:

$$\text{ppm} = \frac{\text{mg/Nm}^3 \times 24.46}{\text{Molecular weight of NO}_x} \tag{6.3}$$

where 24.46 Nm^3/kmol is the molar volume of an ideal gas at standard conditions (i.e., 298.15 K and 1 atm, and the molecular weight of NO_x (in kg kmol^{-1}) is considered based on the specific nitrogen oxide being measured, typically NO or NO_2. The molecular weight of nitrogen dioxide (NO_2), which is 46 kg kmol^{-1}, is used to express NO_x mass when calculating NO_x from emissions data [143]. This leads to a concentration of 106.36 ppm NO_x for existing gas turbines and a concentration of 39.88 ppm for new gas turbines.

Figure 6.10 illustrates the relationship between NO_x emissions and the adiabatic flame temperature for both the premixed and non-premixed variants. The secondary x-axis provides the values of λ.

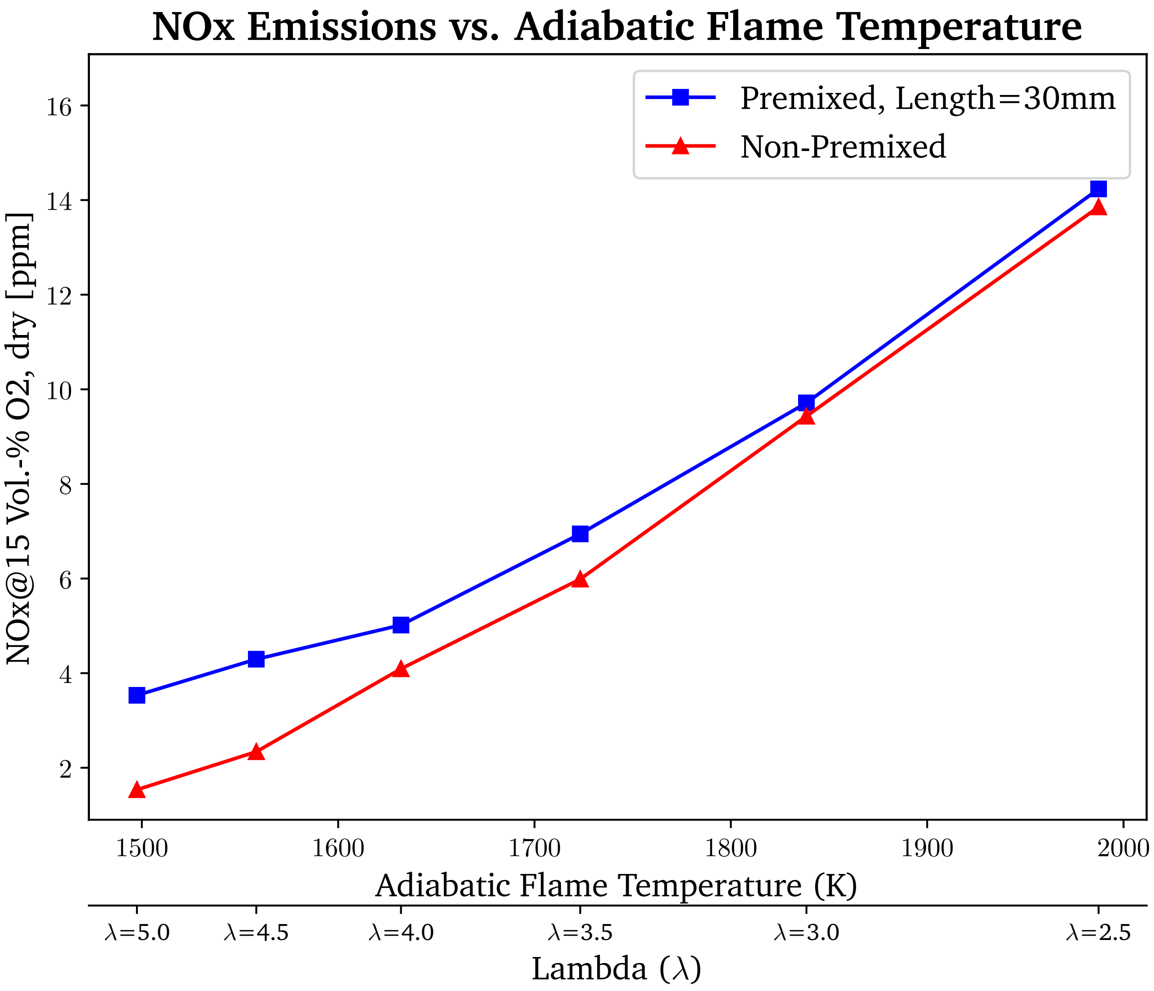

Figure 6.10.: Relationship between NO_x emissions and adiabatic flame temperature for the Jet-Stabilised Pilot Stage - both premixed and non-premixed variants. The trends highlight the exponential increase in NO_x with temperature.

Both trends exhibit an exponential increase in emissions, with the premixed variant consistently producing higher emissions compared to the non-premixed variant across the range of adiabatic flame temperatures.

While the difference in NO_x emissions is only 3% for temperatures above $1838\,K$ (i.e., λ values of 2.5 and 3, respectively), the difference becomes more significant at lower temperatures. For an adiabatic temperature of $1497\,K$ (i.e., $\lambda = 5$), the premixed case produces NO_x emissions that are 2.3 times higher than the non-premixed case. These results support the Zeldovich mechanism [2], which proposes that the formation of thermal NO_x is primarily dependent on temperature and the trends observed are also consistent with the findings presented in Figure 3.6. Importantly, it is worth noting that even the highest recorded NO_x emissions still comply with the NO_x emission regulations set forth by the European Union for new gas turbines [107].

6.2. Configuration 2: Jet-stabilised Main stage and swirl-stabilised Pilot stage

6.2.1. OH*-Chemiluminescence Visualisations

Similar to the jet-stabilised pilot stage configurations, the flame intensity reduces, the flame height becomes shorter, and the lift-off height increases as we move towards leaner compositions. However, due to the 'swirl' aspect of this configuration, there are some notable differences, which are discussed in this section.

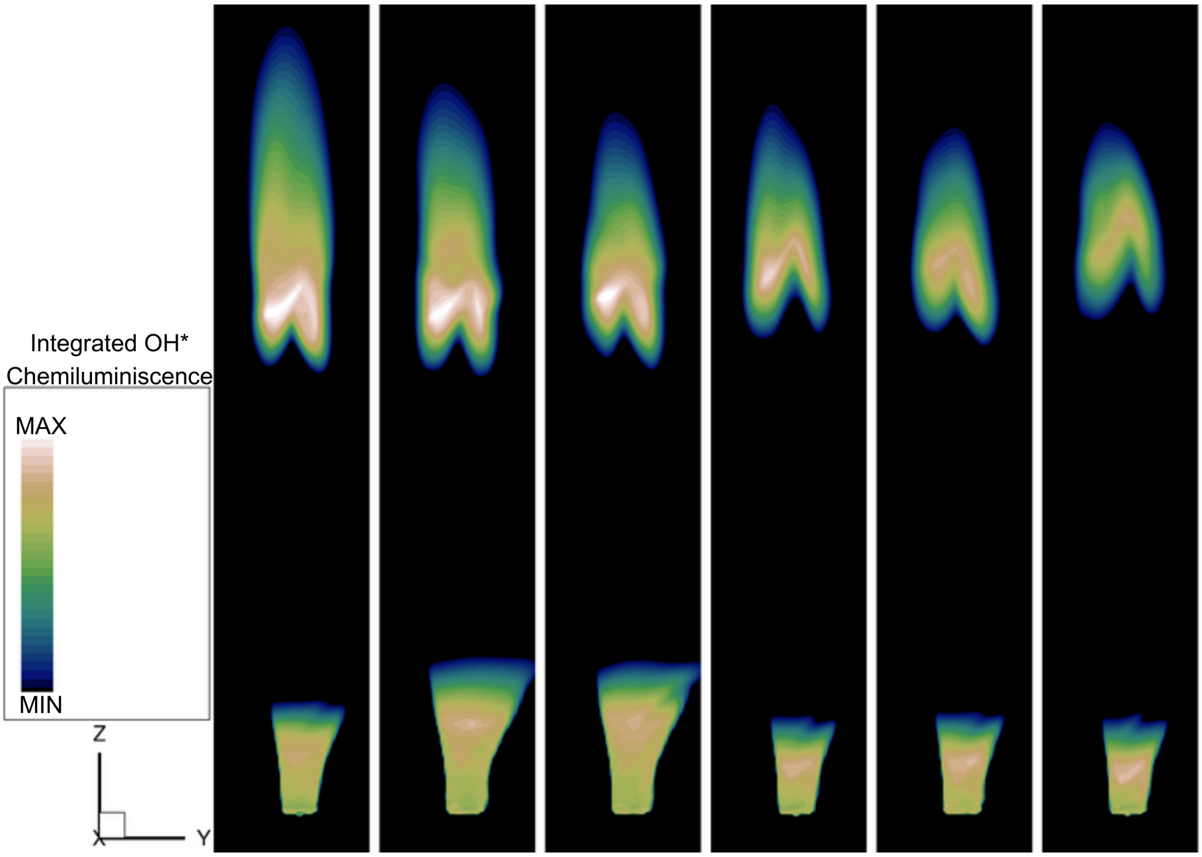

Figure 6.11.: OH*-chemiluminescence visualisation showing the symmetric flame shape and the inverted "V" base in a Swirl-Stabilised Pilot stage configuration with respect to the air-fuel ratio (λ)

Unlike the jet-stabilised pilot stage configuration, the flames in the swirl-stabilised pilot stage configuration exhibit a more symmetric shape, gradually tapering as we move towards the top. The base of the flame also exhibits a familiar inverted ”V” shape, similar to the non-premixed jet-stabilised pilot stage configuration, but the ”V” here is considerably smaller compared to the former configuration.

Coming to the pilot stage, the flame size and especially the width is considerably larger compared to the jet-stabilised pilot stage configuration. The stretching in the lateral direction is attributed to the swirl in this configuration. Since the size of the flame is considerably larger for $\lambda = 3$ and 3.5, and the size and location of flames is similar for $\lambda = 4, 4.5$, and 5; no conclusive comment can be made about the variation in size and lift-off height for the flame of the pilot stage.

Focusing more on the lift-off height, while it generally increases as we increase λ, there is a sudden jump seen for $\lambda = 4$, and the lift-off height is actually higher for $\lambda = 4$ than $\lambda = 4.5$, making $\lambda = 4$ an outlier for this comparison. Additionally, the increase rather resembles a higher-order/exponential relation rather than linear. This can be possibly attributed to the effect of swirl where it tries to confine the flame closer to the nozzle exit for richer compositions, and the effect of the swirl decreases as we move away from the swirl generator. It is expected that the pattern shows a linear increase for even higher values of λ (as long as the flame does not blow out).

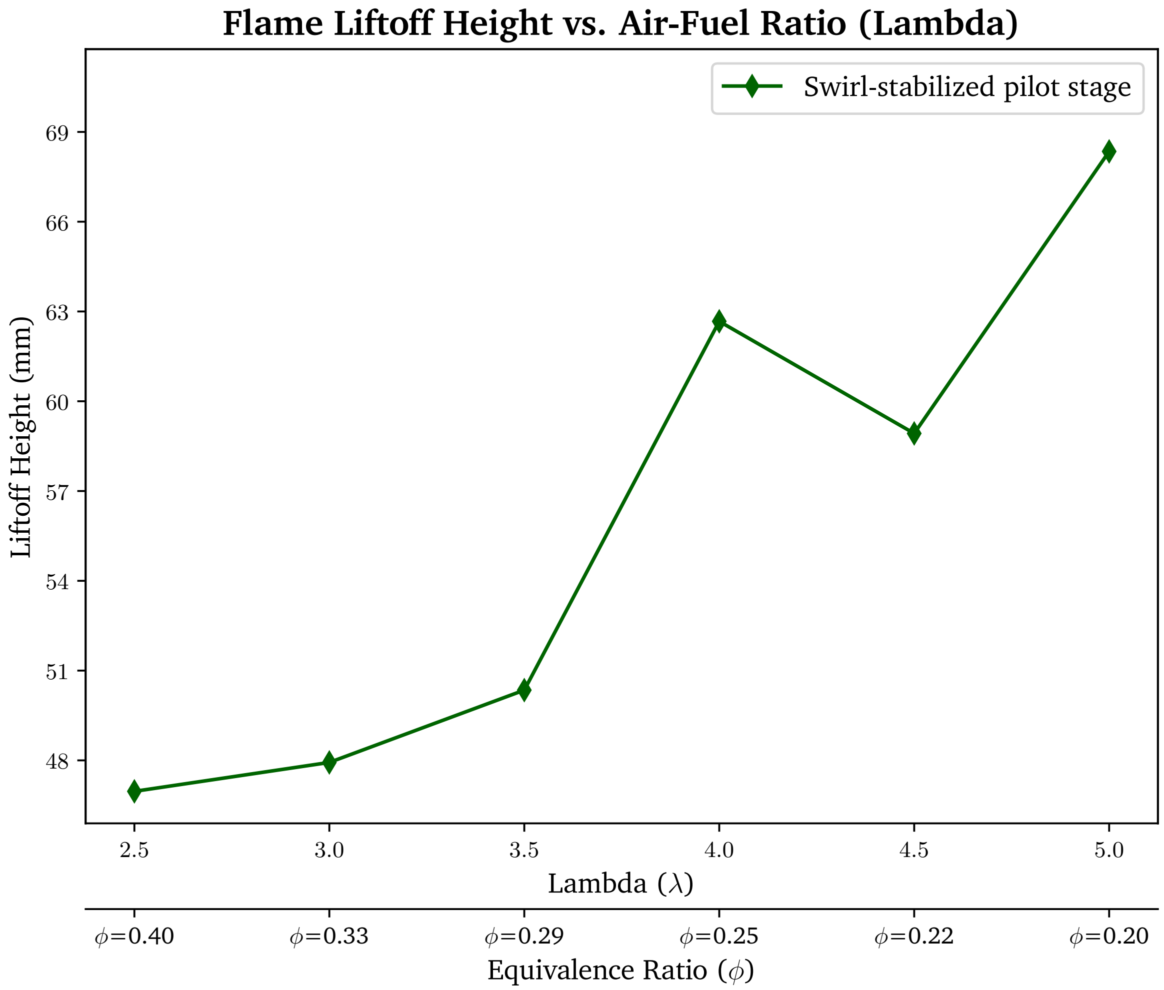

Figure 6.12.: Variation of flame lift-off height with air-fuel ratio (λ), demonstrating the sudden jump in height for $\lambda = 4$ for the Swirl-Stabilised Pilot stage.

6.2.2. Calculation of Lower Heating Value and Mass Flow Rate

In Figure 6.13, the top left image (a) illustrates the Lower Heating Value (LHV) plotted against the equivalence ratio (ϕ), and the top right image (b) displays the calculated fuel mass flow rate plotted against the Equivalence Ratio (ϕ). An additional x-axis for λ is also present. The bottom image (c) describes the deviation (in %) for both the Lower Heating Value and the calculated fuel mass flow rate.

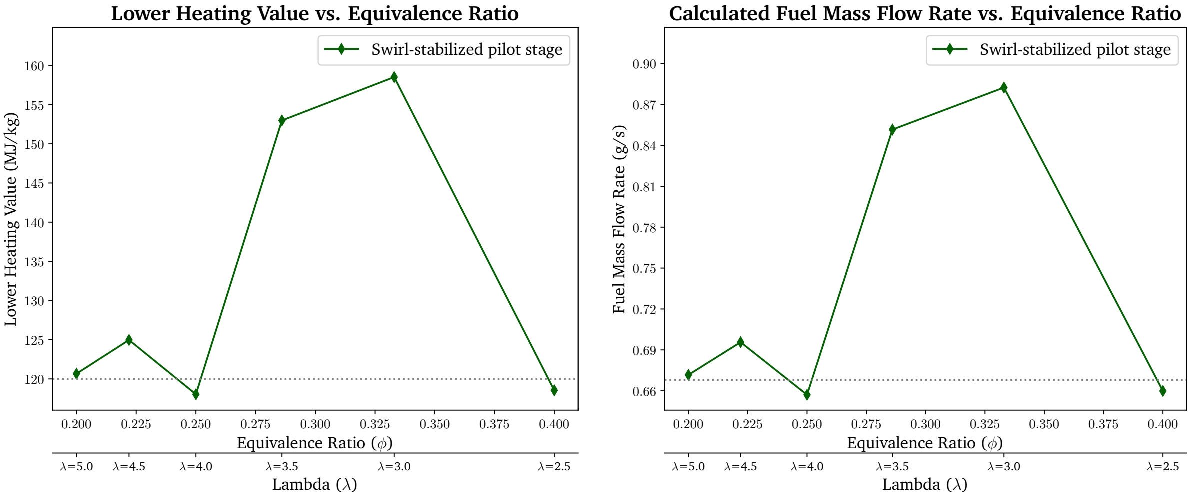

(a) LHV vs ϕ

(b) Calculated fuel mass flow rate vs ϕ

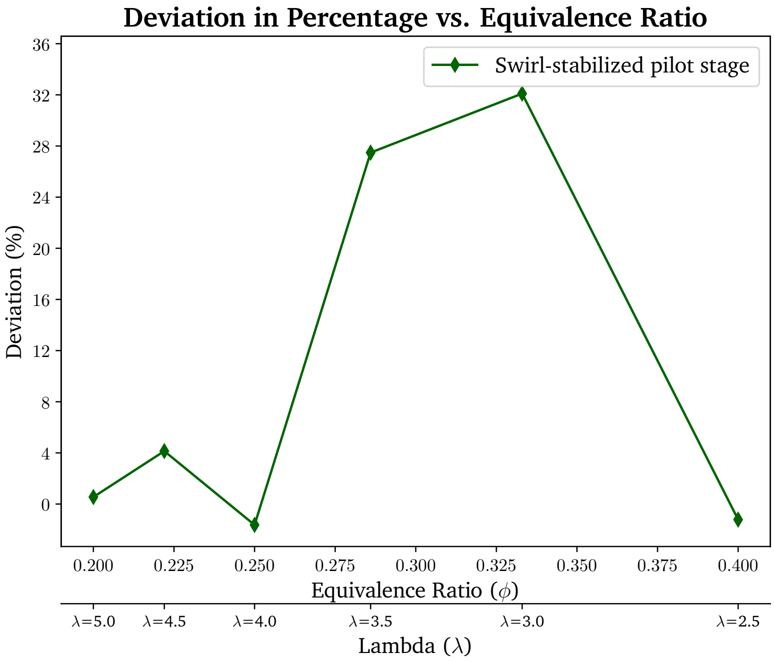

(c) Deviation in LHV and calculated fuel mass flow rate vs ϕ

Figure 6.13.: Comparative analysis of Lower Heating Value (LHV) and mass flow rate across different equivalence ratios (ϕ) for Swirl-Stabilised Pilot stage.

Unlike the jet-stabilised pilot stage configuration, where the deviations for all air-fuel ratios (λ) were insignificant, while the deviations for $\lambda = 2.5, 4, 4.5$, and 5 are still on the lower end (0.5% to 4.1%), the deviation for $\lambda = 3$ and 3.5 are significantly higher, i.e., 32% and 27.5% respectively. This observation also coincides with the finding that the flame size of the pilot-stage flame for these two operating points (Refer to Image 6.11, Section 6.2.1) is unusually large. This essentially indicates that a huge discrepancy should be expected between the simulation results and experimental results for $\lambda = 3$ and 3.5. A possible explanation to this might be the numerical instabilities/solver-related issues encountered during the simulations for these two cases, as it was ensured that element quality was generally good throughout the domain and the simulations still displayed consistent results for rest of the air-fuel compositions.

6.2.3. Recirculation and Velocity Profiles

Figure 6.14 illustrates the flow field characteristics within a jet-stabilised main stage and swirl-stabilised pilot stage configuration, across a range of air-fuel ratios (λ). From left to right, λ is increased from 2.5 to 5 in increments of 0.5. Since this configuration has swirl-stabilisation for the pilot stage, an additional visualisation has been provided in the form of Figure 6.15 to observe the swirl aspect of the flow.

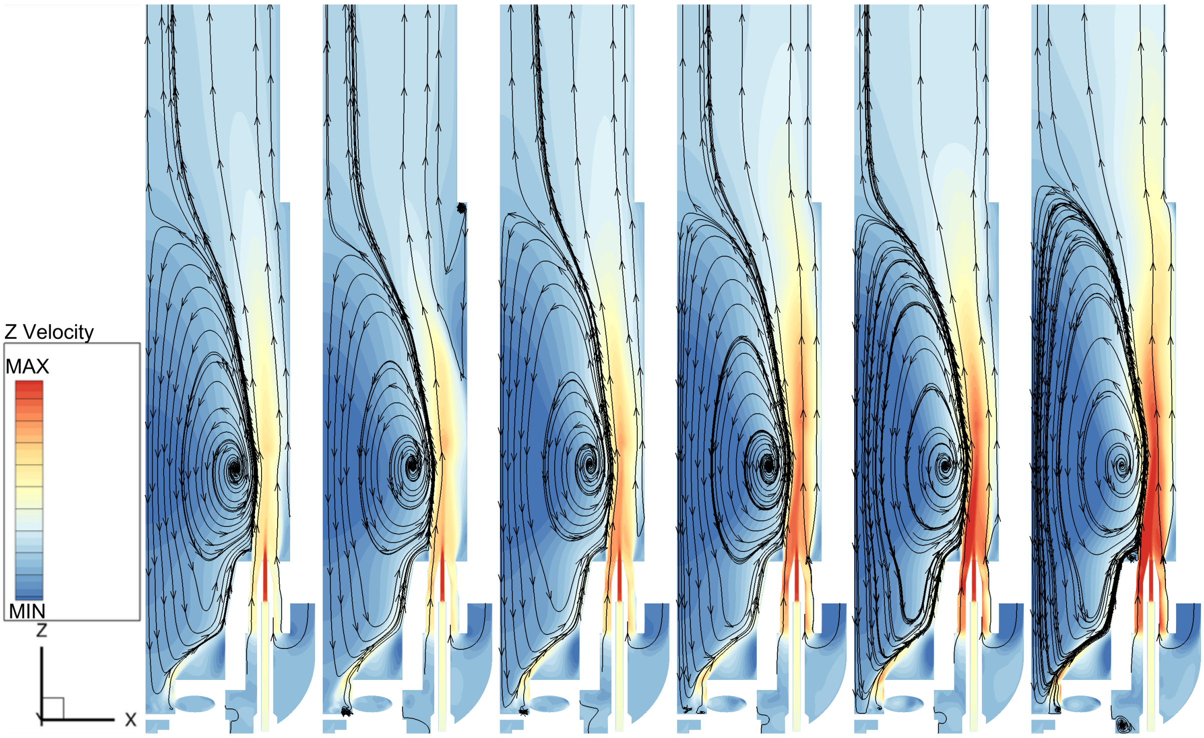

Figure 6.14.: Flow field characteristics across a range of air-fuel ratios (λ) for the Swirl-Stabilised Pilot stage configuration, showcasing the impact of λ increments on recirculation and axial velocity.

Similar to previous configurations, the streamlines indicate recirculation zones while the contour indicates the axial velocity. As we increase λ, we see an increase in Z velocity magnitude, especially near the nozzle exit. The swirl-stabilised configuration also produces a single recirculation zone, unlike the non-premixed jet-stabilised pilot stage configuration. While the vortex center of the recirculation zone stays at the same height across the range of λ, one can observe the extent of the recirculation zone moving towards downstream as we increase the λ. While the sizes of the recirculation zones are larger than the sizes of the primary recirculation zones observed in the jet-stabilised pilot stage, non-premixed configuration (for corresponding value of λ); the sizes are slightly smaller compared to its jet-stabilised pilot stage, premixed counterpart.

The contours present in Figure 6.15 are velocity magnitude contours $V = \sqrt{u^2 + v^2 + w^2}$ represented over a plane perpendicular to the downstream axis and located at a height of $30\,\mathrm{mm}$ above the pilot stage nozzle exit. Here, one can see that the swirl becomes stronger, which is evident from the velocity magnitude shifting to higher values across the contour, as we increase the leanness of the composition.

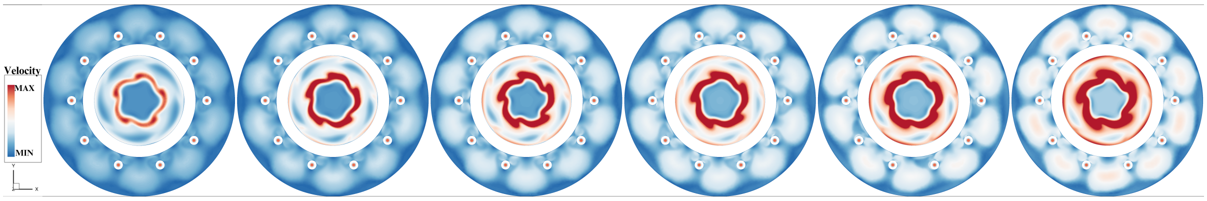

Figure 6.15.: Visualisation of swirl effects within the Swirl-Stabilised Pilot stage, highlighting the velocity magnitude contours ($V = \sqrt{u^2 + v^2 + w^2}$) and the increasing strength of swirl across different air-fuel ratios (λ).

Figure 6.16 illustrates the variation of velocity magnitude along the defined probe line (see Section 6.1.3). In this case, the velocity also rises up to $228.7\,\mathrm{m\,s^{-1}}$ near the Main stage fuel nozzle exit.

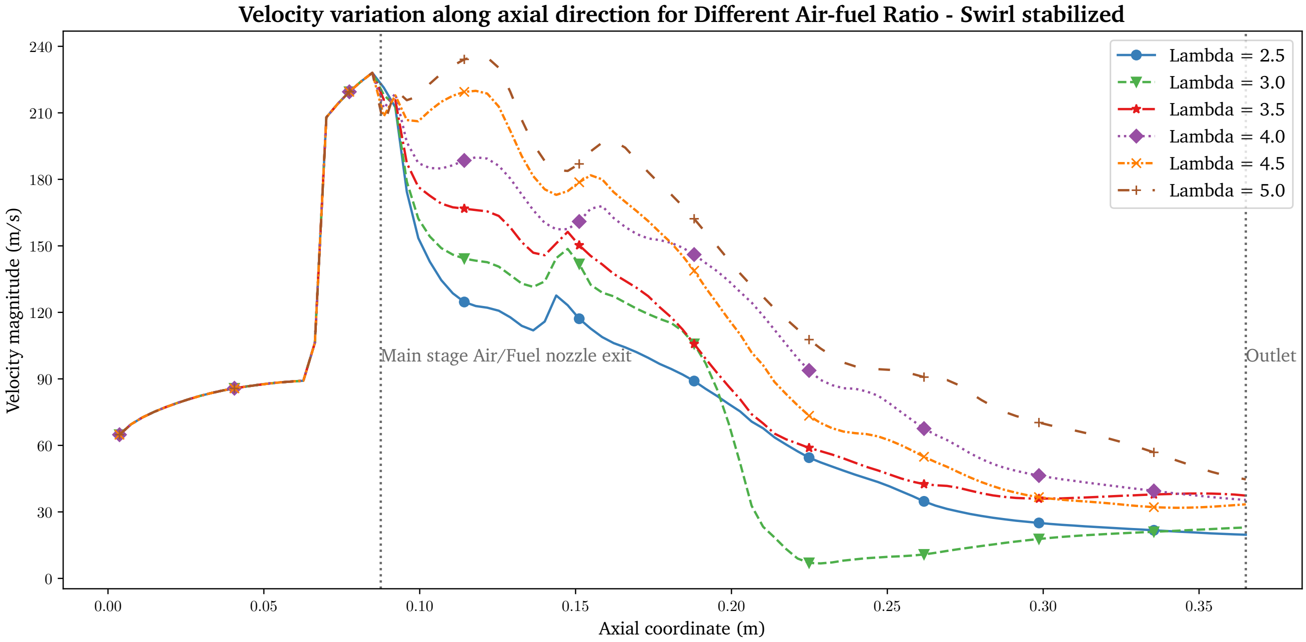

Figure 6.16.: Variation of velocity magnitude along the defined probe line (axial direction) in the Swirl-Stabilised Pilot stage, demonstrating velocity peaks and trends for different air-fuel ratios (λ).

Here too, similar to Section 6.1.3, we can divide the plot into two cases. The first case is for $\lambda = 4, 4.5$, and 5, where we observe two relatively blunt peaks. One peak is at the interface where the fuel and air appear to be well mixed, and the second peak is near the base of the flame. The second case is for $\lambda = 2.5, 3$, and

3.5, where we do not observe any peak related to the mixing. Instead, we see a sharp peak near the base of the flame.

The velocity then follows a decreasing trend all the way up to the outlet, except for $\lambda = 3$. In the case of $\lambda = 3$, the velocity decreases sharply until the midway of the downstream and then slightly increases until reaching the outlet.

6.2.4. Outlet Temperature

Figure 6.17 illustrates the variation of mass-flow averaged outlet temperature on the surface of the outlet. To evaluate these values, comparisons are made with respect to the averaged outlet temperatures for the non-premixed variant of the jet-stabilised pilot stage configuration (see Section 6.1.4).

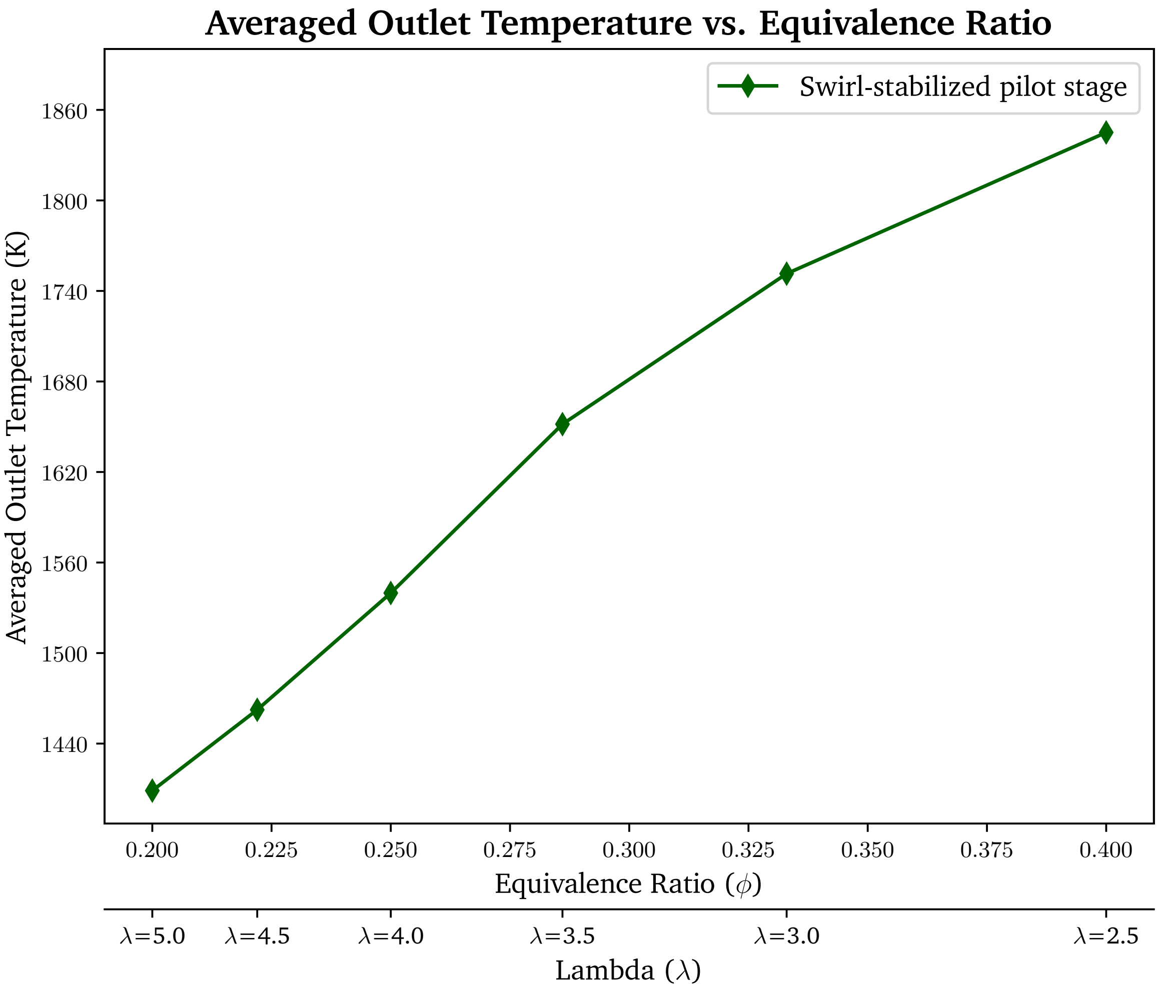

Figure 6.17.: Variation of mass-flow averaged outlet temperatures across different equivalence ratios (ϕ) in the Swirl-Stabilised Pilot stage, and inclusion of a secondary x-axis for air-fuel ratio λ

Similar to the non-premixed jet-stabilised pilot stage variant, an increase in the averaged outlet temperature is observed with an increase in the equivalence ratio ϕ. The temperature values range from $1408.8\,\mathrm{K}$ for

$\phi = 0.2$ to $1845\,\mathrm{K}$ for $\phi = 0.4$. The difference between the outlet temperatures of the swirl-stabilised and corresponding jet-stabilised configurations (both non-premixed) is minimal and within the error tolerances, ranging from $0.18\,\mathrm{K}$ for $\phi = 0.2$ to $12\,\mathrm{K}$ for $\phi = 0.25$. However, the $\phi = 0.33$ and 0.286 (which correspond to $\lambda = 3$ and 3.5, respectively) show anomalies as the difference between their corresponding jet-stabilised counterparts is quite significant, approximately $40\,\mathrm{K}$ higher. If a trend were to be established based on the values observed at other ϕ values, the temperatures observed at these two ϕ values are overestimations. This observation also aligns with the deviations observed in the Lower Heating Value (Section 6.2.2) and the size of the pilot stage flame (Section 6.2.1).

6.2.5. NO$_x$ Emissions

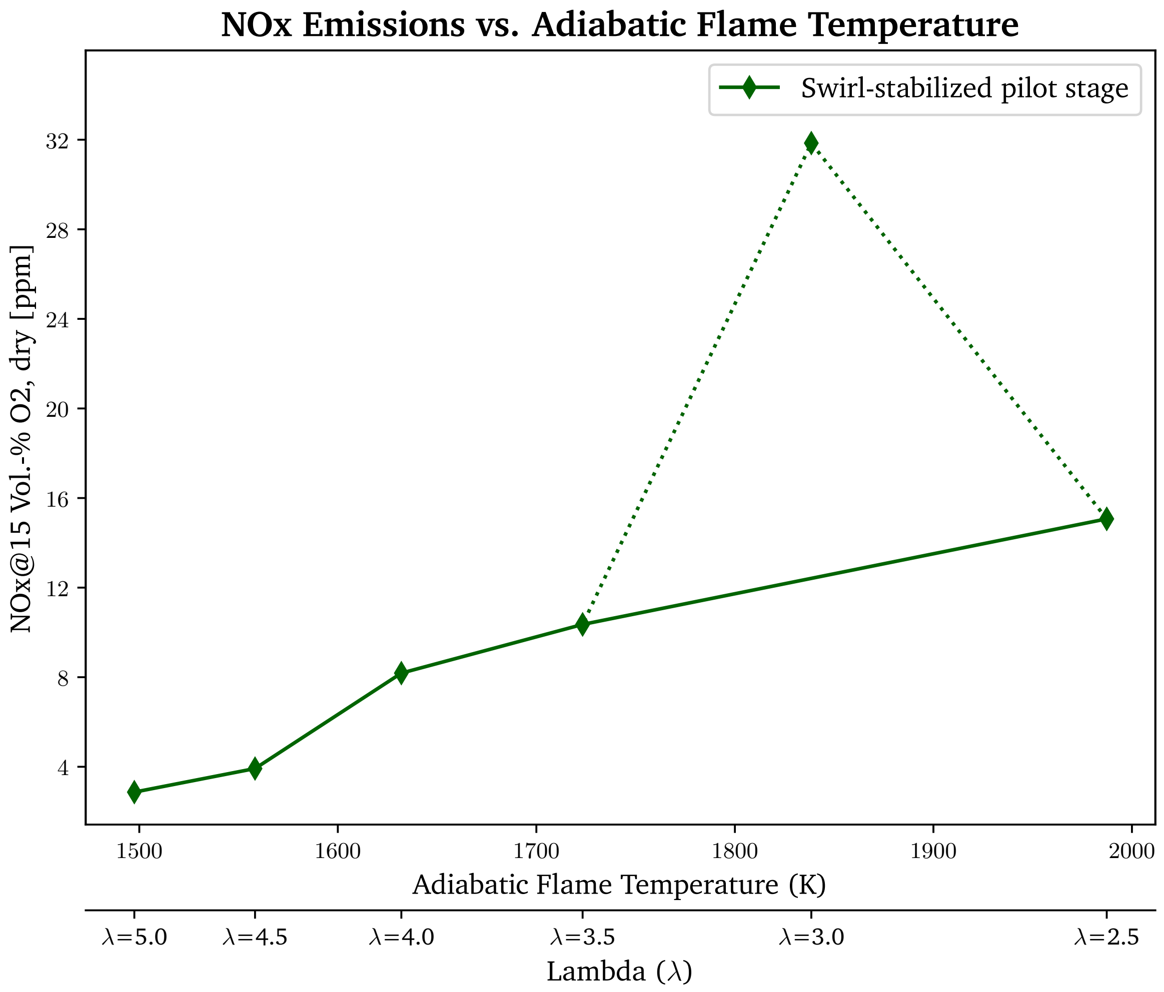

Figure 6.18.: Dependence of standardised NO$_x$ emissions on adiabatic flame temperature for the Swirl-Stabilised Pilot stage, and inclusion of a secondary x-axis for air-fuel ratio λ. An identified outlier at $1347.5\,\mathrm{K}$ has been excluded from the analysis.

Figure 6.18 describes the dependence of NO$_x$ emissions on the adiabatic flame temperature for the swirl-stabilised pilot stage. Here too, the emissions have been standardised and compared with respect to the EU regulations [107], similar to the discussion stated in Section 6.1.5. Also, an additional secondary x-axis containing the values for air-fuel ratio λ has been created.

While the data indicates a rapid increase in NO$_x$ emissions at lower temperatures, there is a transition to a linear trend as temperatures rise. We have identified an outlier at a temperature of $1838\,\mathrm{K}$ (i.e., $\lambda = 3$), where the calculated NO$_x$ emissions are significantly higher (approximately 2.1 times) than the next recorded value. As a result, this outlier has been excluded from the plotted data.

When comparing the swirl-stabilised pilot stage to the jet-stabilised pilot stage variants (refer to Figure 6.10), we observe that NO$_x$ emissions are higher in the swirl-stabilised pilot stage for temperatures above $1566\,\mathrm{K}$. For temperatures below $1566\,\mathrm{K}$, the emissions fall between the premixed and non-premixed variants of the jet-stabilised pilot stage. However, the difference diminishes as temperatures increase. At $1987\,\mathrm{K}$, the emissions are only 5.8% higher compared to the premixed variant, whereas at $1632\,\mathrm{K}$, they are 63% higher.

7. Summary and Outlook

In the context of this study, an investigation was conducted to characterize an atmospheric combustion chamber of Turbec T100 MGT by varying the air-fuel ratios λ for two different configurations. One configuration featured a jet-stabilised pilot stage, while the other had a swirl-stabilised pilot stage. Additionally, the jet-stabilised pilot stage had two variants: one with a premixed main stage and the other with a non-premixed main stage. The simulations were performed using the THETA combustion CFD code developed by DLR. In order to calculate the flow within the combustion chamber, incompressible transport equations for reactive flows had to be solved. The effects of grid size and turbulence models were assessed based on a reference point, and an appropriate numerical setup was consequently developed. After analyzing the results of the grid study, a fine grid was chosen. Regarding the selection of turbulence models, a reference case was simulated using the $k-\omega$ SST and the standard $k-\varepsilon$ models. After considering the advantages and disadvantages of each approach, the $k-\omega$ SST model was ultimately deemed the most suitable choice. For all simulations, a steady-state model was utilised with QUDS, the $k-\omega$ SST turbulence model, the Finite Rate Chemistry combustion model, and the DC1S30N18 (In-house DLR fuel surrogate) reaction mechanism. As there was no available experimental data for validation purposes, the selection of the numerical setup and the evaluation of the results were based solely on the theoretical framework and literature review. The combustion simulations for the jet-stabilised pilot stage yielded appropriate results for the entire range of air-fuel ratios (λ). The OH*-chemiluminescence plots for the premixed variant exhibited a primary flame in the shape of an upward pointing arrow, with the bottom of the flame forming an inverted ”V”. Additionally, the flame approached symmetry as the mixture became leaner. The non-premixed variant displayed a less pointed flame shape, resembling an inverted ”U” with a checkmark-like top, which flattened out as the mixture became leaner. However, in both cases, the flame size decreased and the flame lift-off height increased with increasing leanness of the mixture. As predicted, the flame lift-off height showed a linear increase with respect to λ, and, on average, the non-premixed case had a lift-off height 26.4 mm higher than its corresponding premixed counterpart for each λ value. Both variants demonstrated minimal deviations in calculated lower heating values and mass flow rate, with a maximum deviation of 4.4%.

Recirculation plays a vital role in flame stabilization, temperature reduction, and effective mixing. Interesting findings were observed for both variants. The premixed variant showed only one recirculation zone, with recirculation size decreasing as the mixture became leaner. In contrast, the non-premixed variant exhibited the emergence of a secondary recirculation zone, and the primary recirculation zone increased in size with increasing leanness of the mixture. Velocity magnitude along a probe line passing through the center of the main stage nozzle to the downstream region was plotted. These plots provided insights into the effects of premixing/non-premixing and the location of combustion initiation on velocity magnitude. By analyzing these plots, one can also partially determine the location of the flame base, where air and fuel sufficiently mix, and the region of recirculation.

The outlet temperature, averaged for mass flow, demonstrates a linear increase with respect to the equivalence ratio (ϕ) for both variants. Notably, at lower equivalence ratio values, a significant difference in outlet temperature was observed between the premixed and non-premixed variants. However, this difference became negligible as richer compositions were approached.

To analyse NO_x emissions and compare them with European Union regulations, they were first normalised and standardised to the reference level (dry NO_x emissions at 15% oxygen content). As expected, the NO_x emissions exhibited an exponential increase with increasing adiabatic flame temperatures. Interestingly, emissions from the premixed variant were consistently higher than those from the non-premixed counterpart, for a given adiabatic temperature. However, this difference decreased as higher temperatures were approached, and the maximum observed emissions were around 14.23 ppm, which is well below the EU regulation of 39.88 ppm.

Moving on to the second configuration, the swirl-stabilised pilot stage, the results remained consistent and aligned with theoretical fundamentals. However, a significant deviation was observed for the air-fuel ratios $\lambda = 3$ and 3.5, both in terms of visual representations and quantitative data. For instance, in OH*-chemiluminescence visualizations, while the main stage flame exhibited the expected shape and characteristics, with an inverted "U" shape at the base, the pilot stage flame was unexpectedly large for $\lambda = 3$ and 3.5. Regarding the main stage flame, an increase in liftoff height and a decrease in flame size were observed as leaner compositions were approached. The only exception was at $\lambda = 4.5$, where a small dip in the liftoff height was noted before the trend resumed.

Deviation of up to 32% and 27.5% was observed for $\lambda = 3$ and 3.5, respectively, in relation to the calculated lower heating value and mass flow rate. Concerning the recirculation zones, it was observed that the extent of the recirculation zone moved downstream as leaner compositions were approached. As this configuration included a swirl-stabilised pilot stage, an additional illustration was created to depict the swirl, and it is evident that the swirl strength increased as the λ value increased.

Similar to the jet-stabilised pilot stage, an increase in the mass-flow averaged outlet temperature is observed as the richness of the mixture increases. However, the increase is not linear, possibly due to the deviations observed for $\lambda = 3$ and 3.5. In terms of NO_x emissions, an outlier is observed at $\lambda = 3$ with the emissions reaching up to 31.85 ppm for this specific operating point. However, for the rest of the operating points, the values and trends were comparable to those seen in the jet-stabilised pilot stage configuration, and the emissions recorded here also met the directives of the European Union.

While the lack of experimental data makes it difficult to draw specific conclusions, the study suggests that the non-premixed variant has the lowest NO_x emissions for any given air-fuel composition. Flame flashbacks are a major concern in hydrogen combustion, particularly for premixed cases. However, no flashback phenomena were observed for any of the configurations and air-fuel compositions. Additionally, no flame blowout was observed even for $\lambda = 5$, which supports the statement that hydrogen has a wide operability range when it comes to air-fuel compositions.

The following points outline areas for future research:

According to the grid dependence study conducted in section 5.1, while the fine grid used in this work was sufficient, there was still a minor difference observed between the calculated and extrapolated NO_x emissions. Therefore, it is recommended to attempt a finer grid if sufficient computational resources are available. However, caution should be exercised when setting up the under-relaxation factors and determining the number of iterations required, as a finer mesh will increase both the time per iteration and the number of iterations needed to achieve convergence.

Considering that the simulations exhibited oscillatory convergence when using the $k - \omega$ SST model with QUDS, it is advisable to explore other approaches as well. One such approach is the use of the **R**eynolds **S**tress **M**odel (RSM), which is capable of handling the modeling of anisotropic turbulence. Since the flame shape also changed after every few iterations, pseudo transient approaches or even transient approaches like URANS and LES should be attempted, at least for one reference case. However, it is important to prioritize experimental data collection and assess the available computational resources.

As neither flame flashback nor flame blowout was observed, simulations should be conducted over a wider range of air-fuel compositions.

Since DLR hosts a variety of other reaction mechanisms, it is highly recommended to study and determine the most suitable reaction mechanism. Lastly, while running a micro gas turbine on 100% hydrogen operation appears feasible, greater focus should be placed on testing conventional fuels with hydrogen blends, as this approach seems to be a more viable solution in the near future.

Bibliography

[1] J. Boussinesq. *Essai sur la théorie des eaux courantes*. Imprimerie Nationale, 1877. URL: `https://books.google.de/books?id=4NdQAAAAYAAJ`.

[2] Y. B. Zeldovich. “The Oxidation of Nitrogen in Combustion and Explosions”. In: *Acta Physicochim. SSSR* (1946), pp. 577–625.

[3] F. A. Williams. *Combustion Theory: the fundamental theory of chemical reacting flow systems*. Addison-Wesley, 1965.

[4] D. B. Spalding. “Mixing and chemical reaction in steady confined turbulent flames”. In: *Symposium (International) on Combustion*. Vol. 13. Elsevier, 1971, pp. 649–657.

[5] W. P. Jones and B. Launder. “The prediction of laminarization with a two-equation model of turbulence”. In: *International Journal of Heat and Mass Transfer* 15.2 (1972), pp. 301–314.

[6] B. E. Launder and D. B. Spalding. *Mathematical Models of Turbulence*. Academic Press, 1972. URL: `https://books.google.de/books?id=CEGrGwAACAAJ`.

[7] S. V. Patankar and D. B. Spalding. “A calculation procedure for heat, mass, and momentum transfer in three-dimensional parabolic flow”. In: *International Journal of Heat and Mass Transfer* 15.1 (1972), pp. 787–806.

[8] J. Wolfrum. “Bildung von Stickstoffoxiden bei der Verbrennung”. In: *Chemie Ingenieur Technik* 44.10 (1972), pp. 656–659. DOI: `10.1002/cite.330441004`.

[9] B. E. Launder and D. B. Spalding. *The Numerical Computations of Turbulent Flows*. Imperial College of Science and Technology, 1973. URL: `https://books.google.de/books?id=DUCKtgAACAAJ`.

[10] B. E. Launder and B. I. Sharma. *Application of the Energy-dissipation Model of Turbulence to the Calculation of Flow Near a Spinning Disc*. HTS. Imperial College of Science and Technology, Department of Mechanical Engineering, 1974. URL: `https://books.google.de/books?id=jwlemwEACAAJ`.

[11] B. E. Launder, G. Jr. Reece, and W. Rodi. “Progress in the development of a reynolds-stress turbulence closure”. In: *Journal of Fluid Mechanics* 68.3 (1975), pp. 537–566.

[12] P. Malte and D. Pratt. “Measurement of atomic oxygen and nitrogen oxides in jet-stirred combustion”. In: *Symposium (International) on Combustion*. Vol. 15. 1. 1975, pp. 1061–1070. DOI: `10.1016/S0082-0784(75)80371-7`.

[13] F. A. Williams. “Criteria for existence of wrinkled laminar flame structure of turbulent premixed flames”. In: (1976).

[14] B. Magnussen and B. Hjertager. “On mathematical modeling of turbulent combustion with special emphasis on soot formation and combustion”. In: *Symposium (International) on Combustion*. Vol. 16. Elsevier, 1977, pp. 719–729.

[15] B. Magnussen. “On the structure of turbulence and a generalized eddy dissipation concept for chemical reaction in turbulent flow”. In: *19th Aerospace Sciences Meeting*. 1981.

[16] J. O. Keller, L. Vaneveld, D. Korschelt, et al. “Mechanism of Instabilities in Turbulent Combustion Leading to Flashback”. In: *AIAA Journal* 20.2 (Feb. 1982), pp. 254–262. DOI: `10.2514/3.51073`.

[17] R. Borghi, C. Bruno, and C. Casci. *Recent Advances in Aeronautical Science*. London, UK: Pergamon, 1984.

[18] C. K. Westbrook and F. L. Dryer. “Chemical kinetic modeling of hydrocarbon combustion”. In: *Progress in Energy and Combustion Science* 10.1 (1984), pp. 1–57. DOI: `10.1016/0360-1285(84)90118-7`.

[19] W. Hackbusch. *Multigrid Methods and Applications*. Springer, 1985.

[20] S. B. Pope. “PDF Methods for Turbulent Reactive Flows”. In: *Progress in Energy and Combustion Science* 11 (1985), pp. 119–192.

[21] Y. Saad and M. H. Schulz. “GMRES: A generalized minimal residual algorithm for solving non-symmetric linear systems”. In: *SIAM Journal on Scientific and Statistical Computing* 7.3 (1986), pp. 856–869.

[22] J. H. Seinfeld. *Atmospheric chemistry and physics of air pollution*. New York: John Wiley and Sons, 1986.

[23] J. L. Toof. “A model for the prediction of thermal, prompt, and fuel NOx emissions from combustion turbines”. In: *Journal of Engineering for Gas Turbines and Power* 108.2 (Apr. 1986), pp. 340–347. DOI: `10.1115/1.3239909`.

[24] S. B. Pope. “Turbulent premixed flames”. In: *Annual Review of Fluid Mechanics* 19.1 (1987), pp. 237–270.

[25] D. C. Wilcox. “Multiscale model for turbulent flows”. In: *AIAA Journal* 26.11 (1988), pp. 1311–1320.

[26] D. A. Masten, R. K. Hanson, and C. T. Bowman. “Shock tube study of the reaction H+O2→OH+O using OH laser absorption”. In: *Journal of Physical Chemistry* 94.18 (1990), pp. 7119–7128. DOI: `10.1021/j100382a021`.

[27] H. S. Johnston. “Atmospheric ozone”. In: *Annual Review of Physical Chemistry* 43.1 (1992), pp. 1–31.

[28] M. Khalil and P. Wesseling. “Vertex-centered and cell-centered multigrid for interface problems”. In: *Journal of Computational Physics* 98.1 (1992), pp. 1–10.

[29] H. A. van der Vorst. “BI-CGSTAB: A fast and smoothly converging variant of BI-CG for the solution of nonsymmetric linear systems”. In: *SIAM Journal on Scientific and Statistical Computing* 13.2 (1992), pp. 631–644.

[30] L. H. Cowell and K. O. Smith. “Development of a liquid-fueled, lean-premixed gas turbine combustor”. In: *Journal of Engineering for Gas Turbines and Power* 115.3 (July 1993), pp. 554–562. DOI: `10.1115/1.2906743`.

[31] B. Noll. *Numerische Strömungsmechanik*. In German. Springer, 1993.

[32] D. Baulch, C. Cobos, R. Cox, et al. “Evaluated Kinetic Data for Combustion Modelling Supplement I”. In: *Journal of Physical and Chemical Reference Data* 23.6 (1994), pp. 847–1033. DOI: `10.1063/1.555953`.

[33] F. R. Menter. “Two-equation eddy-viscosity turbulence models for engineering applications”. In: *AIAA Journal* 32.8 (1994), pp. 1598–1605.

[34] S.-O. Ryu, S. M. Hwang, and M. J. Rabinowitz. “Shock tube and modeling study of the H+O2=OH+O reaction over a wide range of composition, pressure, and temperature”. In: *The Journal of Physical Chemistry* 99.38 (1995), pp. 13984–13991. DOI: `10.1021/j100038a022`.

[35] T. H. Shih et al. “A new k-epsilon eddy viscosity model for high Reynolds number turbulent flows”. In: *Computers & Fluids* 24.3 (1995), pp. 227–238.

[36] I. R. Gran and B. Magnussen. “A numerical study of a bluff-body stabilized diffusion flame. Part 2. Influence of combustion modeling and finite-rate chemistry”. In: *Combustion Science and Technology* 119.1-6 (1996), pp. 191–217.

[37] S. A. Orszag et al. *Introduction to Renormalization Group Modeling of Turbulence*. ICASE/LaRC Series in Computational Science and Engineering. Oxford University Press, 1996. ISBN: 9780195355567. URL: `https://books.google.de/books?id=qQvQS_5NSYwC`.

[38] C. J. Chen. *Fundamentals Of Turbulence Modelling*. Taylor & Francis, 1997. ISBN: 9781560324058. URL: `https://books.google.de/books?id=HSCUGJ1n8tgC`.

[39] K. Minakawa, T. Miyajima, and S. Yuasa. “Development of a hydrogen-fueled micro gas turbine with a lean premixed combustor”. In: *33rd Joint Propulsion Conference and Exhibit*. 1997. DOI: `10.2514/6.1997-3388`.

[40] C. E. Baukal and P. B. Eleazer. “Quantifying NOx for industrial combustion processes”. In: *Journal of the Air and Waste Management Association* 48.1 (1998). ISSN: 10473289. DOI: `10.1080/10473289.1998.10463664`.

[41] J. D. Morris et al. “Combustion aspects of application of hydrogen and natural gas fuel mixtures to MS9001E DLN-1 gas turbines at elsta plant, Terneuzen, The Netherlands”. In: *Proceedings of the ASME Turbo Expo*. Stockholm, Dec. 1998. DOI: `10.1115/98-GT-359`.

[42] D. G. Nicol et al. “Development of a Five-Step Global Methane Oxidation-NO Formation Mechanism for Lean-Premixed Gas Turbine Combustion”. In: *Journal of Engineering for Gas Turbines and Power* 121.2 (Apr. 1999), pp. 272–280. DOI: `10.1115/1.2817117`.

[43] M. Casey and T. Wintergerste. *Best Practice Guidelines, European Research Community On Flow, Turbulence and Combustion, Special Interest Group on Quality and Trust in Industrial CFD*. Version 1.01.2000. Fluid Dynamics Laboratory Sulzer Innotec, 2000.

[44] A. D. Little. *Opportunities for micropower and fuel cell gas turbine hybrid systems in industrial applications*. Tech. rep. 85X-TA009V. Cambridge, Massachusetts 02140-2390 U.S.A.: DOE, Jan. 2000.

[45] S. Roller and C.-D. Munz. “A low Mach number scheme based on multi-scale asymptotics”. In: *Computational Visual Science* 3 (2000), pp. 85–91.

[46] J. Fritz, M. Kröner, and T. Sattelmayer. “Flashback in a Swirl Burner With Cylindrical Premixing Zone”. In: *Proceedings of ASME Turbo Expo 2001*. Paper No. 2001-GT-0054. New Orleans, Louisiana, June 2001. DOI: `10.1115/2001-GT-0054`.

[47] Norbert Peters. *Turbulent Combustion*. Cambridge University Press, 2001.

[48] J. Y. Ren et al. “Methane reforming and its potential effect on the efficiency and pollutant emissions of lean methane-air combustion”. In: *Chemical Engineering Science* 56.4 (Mar. 2001), pp. 1541–1549. DOI: `10.1016/S0009-2509(00)00381-X`.

[49] S. Candel. “Combustion dynamics and control: progress and challenges”. In: *Proceedings of the Combustion Institute* 29.1 (Jan. 2002), pp. 1–28. DOI: `10.1016/S1540-7489(02)80007-4`.

[50] J. Ferziger and M. Perić. *Computational Methods for Fluid Dynamics*. 3rd revised. Springer, 2002.

[51] Paul Hedman et al. “Observations of Flame Behavior in a Laboratory-Scale Pre-Mixed Natural Gas/Air Gas Turbine Combustor From PLIF Measurements of OH”. In: *American Society of Mechanical Engineers, International Gas Turbine Institute, Turbo Expo (Publication) IGTI* 2 (Jan. 2002). DOI: `10.1115/GT2002-30052`.

[52] R. Sieber. “Numerische Simulation technischer Strömungen mit Fluid-Struktur-Kopplung”. PhD thesis. Technische Universität Darmstadt, 2002.

[53] O. Kunz. “PDF-Simulation von Verbrennungsvorgängen in praxisnahen Brennkammern”. PhD thesis. Universität Stuttgart, Institut für Verbrennungstechnik, 2003.

[54] J.G. Lee and D.A. Santavicca. “Experimental diagnostics for the study of combustion instabilities in lean premixed combustors”. In: *Journal of Propulsion and Power* 19.5 (2003), pp. 735–750.

[55] F. R. Menter, M. Kuntz, and R. Langtry. “Ten years of industrial experience with the sst turbulence model”. In: *Turbulence, Heat and Mass Transfer* 4.1 (2003), pp. 625–632.

[56] P. Gerlinger. *Numerische Verbrennungssimulation, Effiziente numerische Simulation turbulenter Verbrennung*. In German. Springer, 2005. ISBN: 9783540233374. URL: `https://books.google.de/books?id=Su4mBAAAQBAJ`.

[57] H. Guo et al. “The effect of hydrogen addition on flammability limit and NOx emission in ultra-lean counterflow CH4/air premixed flames”. In: *Proceedings of the Combustion Institute* 30.1 (Jan. 2005), pp. 303–311. DOI: `10.1016/J.PROCI.2004.08.177`.

[58] K. K. Kuo. *Principles of Combustion*. John Wiley, 2005. ISBN: 9780471046899. URL: `https://books.google.de/books?id=jAYoAQAAMAAJ`.

[59] B. Magnussen. “The eddy dissipation concept a bridge between science and technology”. In: *ECCOMAS Thematic Conference on Computational Combustion*. 2005, pp. 21–24.

[60] O. Özcan, K. E. Meyer, and P. S. Larsen. “Measurement of mean rotation and strain-rate tensors by using stereoscopic piv”. In: *Experiments in Fluids* 39.4 (2005), pp. 771–783.

[61] Thierry Poinsot and Denis Veynante. *Theoretical and Numerical Combustion*. R.T. Edwards, Inc., 2005.

[62] S. Roller. “Ein numerisches Verfahren zur Simulation schwach kompressibler Strömungen”. In German. Ph.D. thesis. University of Stuttgart, Institute of Aerodynamics and Gasdynamics, 2005.

[63] G. Sanna and G. Tomassetti. *Introduction to molecular beams gas dynamics*. World Scientific, 2005.

[64] R. Fortenbach. “Mehrskalenmodellierung von aeroakustischen Quellen in schwach kompressibler Strömungen”. In German. Ph.D. thesis. University of Stuttgart, Institute of Aerodynamics and Gasdynamics, 2006.

[65] F. Joos. *Technische Verbrennung: Verbrennungstechnik, Verbrennungsmodellierung, Emissionen*. Springer Berlin Heidelberg, 2006. ISBN: 9783540343349. URL: `https://books.google.de/books?id=NC4iBAAAQBAJ`.

[66] P. Sagaut, D. Deck, and M. Terracol. *Multiscale and Multiresolution Approaches in Turbulence*. Imperial College Press, 2006.

[67] H. Schütz et al. “Analysis of the Pollutant Formation in the FLOX Combustion”. In: *Proceedings of the ASME Turbo Expo: Power for Land, Sea and Air*. 2006.

[68] P. Terrie and K. Boguski. *Understanding units of measurement*. Environmental Science and Technology Briefs for Citizens. 2006.

[69] D. C. Wilcox. *Turbulence Modeling for CFD*. Bd. 1 in Turbulence Modeling for CFD. DCW Industries, 2006. ISBN: 9781928729082. URL: `https://books.google.de/books?id=q4ypAQAACAAJ`.

[70] M. Kröner et al. “Flame Propagation in Swirling Flows-Effect of Local Extinction on the Combustion Induced Vortex Breakdown”. In: *Combustion Science and Technology* 179 (2007), pp. 1385–1416. DOI: `10.1080/00102200601149902`.

[71] Lewis Fry Richardson. *Weather prediction by numerical process*. Cambridge University Press, 2007.

[72] W. Versteeg and H. K. Malalasekera. *An Introduction to Computational Fluid Dynamics: The Finite Volume Method*. Pearson Education Limited, 2007. ISBN: 9780131274983. URL: `https://books.google.de/books?id=RvBZ-UMpGzIC`.

[73] I. Celik, U. Ghia, and P. Roache. "Procedure of Estimation and Reporting of Uncertainty Due to Discretization in CFD Application". In: *Journal of Fluids Engineering* 130.7 (2008), pp. 078001-1–078001-4. DOI: `10.1115/1.4004762`.

[74] M. Di Domenico. "Numerical Simulation of Soot Formation in Turbulent Flows". Ph.D. thesis. University of Stuttgart, Institute of Combustion Technology for Aerospace Engineering, 2008.

[75] Franz Durst. *Fluid Mechanics: An Introduction to the Theory of Fluid Flows*. Springer Science & Business Media, 2008.

[76] T. Lieuwen et al. "Burner Development and Operability Issues Associated with Steady Flowing Syngas Fired Combustors". In: *Combustion Science and Technology* 180.6 (2008), pp. 1169–1192. DOI: `10.1080/00102200801963375`.

[77] C. L. Rumsey and J. L. Thomas. *Application of FUN3D and CFL3D to the Third Workshop on CFD Uncertainty Analysis*. Techn. Ber. NASA, Nov. 2008.

[78] B. Epple et al. *Simulation von Kraftwerken und wärmetechnischen Anlagen*. Springer Vienna, 2009. ISBN: 9783211296974. URL: `https://books.google.de/books?id=F7gmBAAAQBAJ`.

[79] J. P. Frenillot et al. "Impact of H2 addition on flame stability and pollutant emissions for an atmospheric kerosene/air swirled flame of laboratory scaled gas turbine". In: *International Journal of Hydrogen Energy* 34.9 (May 2009), pp. 3930–3944. DOI: `10.1016/J.IJHYDENE.2009.02.059`.

[80] W. Kimmerle and M. Stroppel. *Analysis für Ingenieure, Mathematiker und Physiker*. edition delkhofen, 2009. ISBN: 9783936413236. URL: `https://books.google.de/books?id=d1JYcgAACAAJ`.

[81] S. R. Sellevåg, Y. Georgievskii, and J. A. Miller. "Kinetics of the Gas-Phase Recombination Reaction of Hydroxyl Radicals to Form Hydrogen Peroxide". In: *The Journal of Physical Chemistry A* 113.16 (2009), pp. 4457–4467. DOI: `10.1021/jp8110524`.

[82] C. Eichler and T. Sattelmayer. "Experiments on Flame Flashback in a Quasi-2D Turbulent Wall Boundary Layer for Premixed Methane-Hydrogen-Air Mixtures". In: *Journal of Engineering for Gas Turbines and Power* 133.1 (Sept. 2010). DOI: `10.1115/1.4001985`.

[83] O. Lammel et al. "FLOX®combustion at high power density and high flame temperatures". In: *Journal of Engineering for Gas Turbines and Power* 132.12 (2010).

[84] C. K. Law. *Combustion Physics*. Cambridge University Press, 2010.

[85] A. H. Lefebvre and D. R. Ballal. *Gas Turbine Combustion: Alternative Fuels and Emissions*. Taylor & Francis, 2010.

[86] F. R. Menter and Y. Egorov. "The scale-adaptive simulation method for unsteady turbulent flow predictions. Part 1: Theory and model description". In: *Flow, Turbulence and Combustion* 85.1 (2010), pp. 113–138. DOI: `10.1007/s10494-010-9264-5`.

[87] S. Burmberger and T. Sattelmayer. "Optimization of the Aerodynamic Flame Stabilization for Fuel Flexible Gas Turbine Premix Burners". In: *Journal of Engineering for Gas Turbines and Power* 133.10 (2011), p. 101501. DOI: `10.1115/1.4003066`.

[88] M. Di Domenico, P. Gerlinger, and B. Noll. "Numerical Simulations of Confined, Turbulent, Lean, Premixed Flames using a Detailed Chemistry Combustion Model". In: *Proceedings of the ASME Turbo Expo*. GT2011-45520. Vancouver, British Columbia, Canada, June 2011.

[89] Z. Hong et al. “A new shock tube study of the $H+O2\rightarrow OH+O$ reaction rate using tunable diode laser absorption of $H2O$ near 2.5µm”. In: *Proceedings of the Combustion Institute*. Vol. 33. 1. 2011, pp. 309–316. doi: `10.1016/j.proci.2010.05.101`.

[90] M. Lambert. *THETA-Code Developer’s Guide*. Release 8.2. German Aerospace Center (DLR), Institute of Aerodynamics and Flow Technology, 2011.

[91] P. Li et al. “Progress and Recent Trend in MILD Combustion”. In: *Science China Technological Sciences* 54.2 (2011), pp. 255–269.

[92] A. Meister. *Numerik linearer Gleichungssysteme: Eine Einführung in moderne Verfahren*. 4th ed. In German. Vieweg und Teubner, 2011.

[93] M. Oberlack et al. “Direkte Numerische Simulation der Turbulenz”. In: *Wissenschaftsmagazin forschen* 2 (2011), pp. 32–35.

[94] C. Eichler and T. Sattelmayer. “Premixed flame flashback in wall boundary layers studied by long-distance micro-PIV”. In: *Experiments in Fluids* 52.2 (Feb. 2012), pp. 347–360. doi: `10.1007/s00348-011-1226-8`.

[95] A. Gruber et al. “Direct numerical simulation of premixed flame boundary layer flashback in turbulent channel flow”. In: *Journal of Fluid Mechanics* 709 (2012), pp. 516–542. doi: `10.1017/jfm.2012.345`.

[96] T. C. Lieuwen. *Unsteady Combustor Physics*. Cambridge University Press, 2012.

[97] B. Mühlbauer. “Numerische Simulation von Verbrennungslärm”. Dissertation. Universität Stuttgart, Institut für Verbrennungstechnik der Luft- und Raumfahrt, 2012. url: `http://elib.uni-stuttgart.de/opus/volltexte/2012/7137/`.

[98] R. Schwarze. *CFD-Modellierung: Grundlagen und Anwendungen bei Strömungsprozessen*. Springer Berlin Heidelberg, 2012. isbn: 9783642243776. url: `https://books.google.de/books?id=vFGEkds_zY0C`.

[99] Luis Roberto Tay Wo Chong Hilares. “Numerical Simulation of the Dynamics of Turbulent Swirling Flames”. PhD thesis. Lehrstuhl für Thermodynamik, Technische Universität München, 2012. url: `https://mediatum.ub.tum.de/doc/1093223/1093223.pdf`.

[100] S. R. Turns. *An Introduction to Combustion: Concepts and Applications*. McGraw-Hill Series in Mechanical Engineering. McGraw-Hill, 2012. isbn: 9780071086875. url: `https://books.google.de/books?id=idM8twAACAAJ`.

[101] K. K. Venkataraman et al. “Mechanism of combustion instability in a lean premixed dump combustor”. In: *Journal of Propulsion and Power* 15.6 (May 2012), pp. 909–918. doi: `10.2514/2.5515`.

[102] J. Warnatz, U. Maas, and R. W. Dibble. *Combustion: Physical and Chemical Fundamentals, Modeling and Simulation, Experiments, Pollutant Formation*. Springer Berlin Heidelberg, 2012. isbn: 9783642980275. url: `https://books.google.de/books?id=DdnzCAAAQBAJ`.

[103] P. Böckh and C. Saumweber. *Fluidmechanik: Einführendes Lehrbuch*. Springer Berlin Heidelberg, 2013. isbn: 9783642338922. url: `https://books.google.de/books?id=D1kEMpNa3wC`.

[104] W. Jost. *Explosions-und Verbrennungsvorgänge in Gasen*. Springer-Verlag, 2013.

[105] G. Reichling, B. Noll, and M. Aigner. “Numerical simulation of the non-reactive and reactive flow in a swirled model gas turbine combustor”. In: *21st AIAA Computational Fluid Dynamics Conference*. AIAA 2013-2434. 2013.

[106] T. Zornek, T. Monz, and M. Aigner. “A micro gas turbine combustor for the use of product gases from biomass gasification”. In: *Proceedings of the 6th European Combustion Meeting*. 2013.

[107] European Union. *Directive (EU) 2015/2193 of the European Parliament and of the Council on the limitation of emissions of certain pollutants into the air from medium combustion plants*. Official Journal of the European Union EN. 2014.

[108] I. Glassman, R. A. Yetter, and N. G. Glumac. *Combustion*. Academic Press, 2014.

[109] A. Meister. *Numerik linearer Gleichungssysteme: Eine Einführung in moderne Verfahren*. Springer Fachmedien Wiesbaden, 2014. ISBN: 9783658072001. URL: `https://books.google.de/books?id=Z_5MBQAAQBAJ`.

[110] H. Y. Shih and C. R. Liu. "A computational study on the combustion of hydrogen/methane blended fuels for a micro gas turbines". In: *International Journal of Hydrogen Energy* 39.27 (Sept. 2014), pp. 15103–15115. DOI: `10.1016/J.IJHYDENE.2014.07.046`.

[111] C. Tang, Y. Zhang, and Z. Huang. "Progress in combustion investigations of hydrogen enriched hydrocarbons". In: *Renewable and Sustainable Energy Reviews* 30 (Feb. 2014), pp. 195–216. DOI: `10.1016/J.RSER.2013.10.005`.

[112] T. Knacke. *Numerische Simulation des Geräusches massiv abgelöster Strömung bei großer Reynoldszahl und kleiner Machzahl*. Universitätsverlag TU Berlin, 2015. ISBN: 9783798327351. URL: `https://books.google.de/books?id=D_XyBgAAQBAJ`.

[113] Hocine Oumeraci. *Vorlesungsskript Hydromechanik*. Lecture notes by Prof. Dr.-Ing. Hocine Oumeraci. 2015.

[114] G. Reichling. "Development of numerical methods for the calculation of thermo-acoustic interactions in gas turbine combustion chambers". PhD thesis. University of Stuttgart, Institute of Combustion Technology for Aerospace Engineering, 2015. DOI: `http://dx.doi.org/10.18419/opus-3961`. URL: `https://elib.uni-stuttgart.de/bitstream/11682/3978/1/Dissertation_Reichling_final.pdf`.

[115] J. Zanger, T. Monz, and M. Aigner. "Experimental investigation of the combustion characteristics of a double-staged FLOX-based combustor on an atmospheric and a micro gas turbine test rig". In: *ASME Turbo Expo 2015: Turbine Technical Conference and Exposition*. American Society of Mechanical Engineers. 2015.

[116] A. Lechtenberg. "Hybride Verbrennungslärm-Simulation eines FLOX®-Einzeldüsen-Brenners unter Hochdruckbedingungen". Master's Thesis. Institut für Verbrennungstechnik der Luft- und Raumfahrt, 2016.

[117] J. M. Lourier. "Numerische Simulation von thermoakustischen Instabilitäten in Gasturbinenbrennkammern mithilfe von Impedanzrandbedingungen". Dissertation. Deutsches Zentrum für Luft-und Raumfahrt, Institut für Verbrennungstechnik, 2016. URL: `http://elib.dlr.de/105654/1/Dissertation_Lourier_20290616.pdf`.

[118] F. Setzwein. "Untersuchungen zu Verbrennungslärm in einer Modellbrennkammer unter Berücksichtigung verschiedener Verbrennungsparameter". MA thesis. Universität Stuttgart, Institut für Feuerungs- und Kraftwerkstechnik, 2016.

[119] A. Cappelletti and F. Martelli. "Investigation of a pure hydrogen fueled gas turbine burner". In: *International Journal of Hydrogen Energy* 42.15 (Apr. 2017), pp. 10513–10523. DOI: `10.1016/J.IJHYDENE.2017.02.104`.

[120] F. Grimm. "Effiziente, stochastische Vorhersage von turbulentem Brennkammerlärm". Dissertation. Deutsches Zentrum für Luft-und Raumfahrt, Institut für Verbrennungstechnik, 2017. URL: `https://elib.uni-stuttgart.de/handle/11682/9600`.

[121] V. Hoferichter and T. Sattelmayer. *Boundary Layer Flashback in Premixed Hydrogen-Air Flames With Acoustic Excitation*. 2017. DOI: `10.1115/GT2017-63080`.

[122] C. J. Lapeyre, M. Mazur, P. Scouflaire, et al. “Acoustically Induced Flashback in a Staged Swirl-Stabilized Combustor”. In: *Flow, Turbulence and Combustion* 98.1 (Jan. 2017), pp. 265–282. DOI: `10.1007/s10494-016-9745-2`.

[123] S. Lecheler. *Numerische Strömungsberechnung: Schneller Einstieg in ANSYS CFX 18 durch einfache Beispiele*. Springer Fachmedien Wiesbaden, 2017. ISBN: 9783658191924. URL: `https://books.google.de/books?id=kx0-DwAAQBAJ`.

[124] H. Amar et al. “Effect of the addition of H2 and H2O on the polluting species in a counter-flow diffusion flame of biogas in flameless regime”. In: *International Journal of Hydrogen Energy* 43.6 (Feb. 2018), pp. 3475–3481. DOI: `10.1016/J.IJHYDENE.2017.11.159`.

[125] T. Best et al. “CO2-enhanced and humidified operation of a micro-gas turbine for carbon capture”. In: *Journal of Cleaner Production* 176 (Mar. 2018). DOI: `10.1016/J.JCLEPRO.2017.12.062`.

[126] B. A. Imteyaz et al. “Combustion behavior and stability map of hydrogen-enriched oxy-methane premixed flames in a model gas turbine combustor”. In: *International Journal of Hydrogen Energy* 43.34 (Aug. 2018), pp. 16652–16666. DOI: `10.1016/J.IJHYDENE.2018.07.087`.

[127] P. Rajpara, R. Shah, and J. Banerjee. “Effect of hydrogen addition on combustion and emission characteristics of methane fuelled upward swirl can combustor”. In: *International Journal of Hydrogen Energy* 43.36 (Sept. 2018), pp. 17505–17519. DOI: `10.1016/J.IJHYDENE.2018.07.111`.

[128] Stefan Hasemann-Seeger. “Entwicklung eines Brennkammersystems mit Abgasrückführung für den Einsatz in Mikrogasturbinen”. PhD thesis. Jan. 2019. URL: `https://elib.uni-stuttgart.de/bitstream/11682/10849/3/VT-FB_2020-01_StefanHasemann-Seeger.pdf`.

[129] Q. Zhou et al. “Effects of fuel composition and initial pressure on laminar flame speed of H2/CO/CH4 bio-syngas”. In: *Fuel* 238 (Feb. 2019), pp. 149–158. DOI: `10.1016/J.FUEL.2018.10.106`.

[130] M. Ditaranto, T. Heggset, and D. Berstad. “Concept of hydrogen fired gas turbine cycle with exhaust gas recirculation: assessment of process performance”. In: *Energy* 192 (Feb. 2020), p. 116646. DOI: `10.1016/J.ENERGY.2019.116646`.

[131] E. V. Jithin, R. J. Varghese, and R. K. Velamati. “Experimental and numerical investigation on the effect of hydrogen addition and N2/CO2 dilution on laminar burning velocity of methane/oxygen mixtures”. In: *International Journal of Hydrogen Energy* 45.33 (June 2020), pp. 16838–16850. DOI: `10.1016/J.IJHYDENE.2020.04.105`.

[132] L. Xiang et al. “Numerical study of the physical and chemical effects of hydrogen addition on laminar premixed combustion characteristics of methane and ethane”. In: *International Journal of Hydrogen Energy* 45.39 (Aug. 2020), pp. 20501–20514. DOI: `10.1016/J.IJHYDENE.2019.11.040`.

[133] Sandro Bücheler. “Entwicklung eines jet-stabilisierten Brennkammersystems für niederkalorische Brennstoffzellenabgase”. Development of a jet-stabilized combustion system for the use of low-caloric fuel cell off-gas. Dissertation. Stuttgart : Deutsches Zentrum für Luft- und Raumfahrt, Institut für Verbrennungstechnik, 2021. DOI: `10.18419/opus-11520`. URL: `https://elib.dlr.de/148591/1/VT-FB_2021-01_SandroBuecheler.pdf`.

[134] C. T. Chong and J.-H. Ng. “Combustion performance of biojet fuels”. In: *Biojet fuel in aviation applications*. Elsevier, 2021, pp. 175–230. DOI: `10.1016/B978-0-12-822854-8.00002-0`.

[135] Trupti Kathrotia et al. “Combustion kinetics of alternative jet fuels, Part-II: Reaction model for fuel surrogate”. In: *Fuel* 302 (2021), p. 120736. ISSN: 0016-2361. DOI: `https://doi.org/10.1016/j.fuel.2021.120736`. URL: `https://www.sciencedirect.com/science/article/pii/S001623612100613X`.

[136] J. Yang et al. “Thermodynamic modelling and real-time control strategies of solar micro gas turbine system with thermochemical energy storage”. In: *Journal of Cleaner Production* 304 (July 2021), p. 127010. DOI: `10.1016/J.JCLEPRO.2021.127010`.

[137] Reyhaneh Banihabib and Mohsen Assadi. “A Hydrogen-Fueled Micro Gas Turbine Unit for Carbon-Free Heat and Power Generation”. In: *Sustainability* 14.20 (2022). ISSN: 2071-1050. DOI: `10.3390/su142013305`. URL: `https://www.mdpi.com/2071-1050/14/20/13305`.

[138] Darshan Raju. “CFD Study on Flame Flashback in Low Swirl Premixed Burners”. Masters thesis. Delft University of Technology (TU Delft), Mechanical, Maritime and Materials Engineering, Aug. 2022. URL: `http://resolver.tudelft.nl/uuid:4d0ab9d6-b6e4-4e48-92d9-4e6cda34f712`.

[139] Y. Sun et al. “Effect of hydrogen addition on the combustion and emission characteristics of methane under gas turbine relevant operating condition”. In: *Fuel* 324 (Sept. 2022), p. 124707. DOI: `10.1016/J.FUEL.2022.124707`.

[140] Y. Zhang, D. Davis, and M. J. Brear. “The role of hydrogen in decarbonizing a coupled energy system”. In: *Journal of Cleaner Production* 346 (Apr. 2022). DOI: `10.1016/J.JCLEPRO.2022.131082`.

[141] ANSYS, Inc. *ANSYS Workbench Meshing User Guide*. 2023. URL: `https://www.ansys.com/`.

[142] Deutsches Zentrum für Luft- und Raumfahrt e.V. *The Development of Flexible Jet Stabilised Combustion Chamber Systems*. 2023. URL: `https://www.dlr.de/en/vt/research-transfer/themes/the-development-of-flexible-jet-stabilised-combustion-chamber-systems`.

[143] Cedric Peter Devriese. “The CFD design and optimisation of a compressor, combustor and turbine system towards a 100 kWe hydrogen fuelled micro gas turbine”. English. PhD thesis. Mechanical Engineering, Université de Mons, 2023. ISBN: 978-90-386-5871-1. URL: `https://pure.tue.nl/ws/portalfiles/portal/307934571/20231018_Devriese_hf.pdf`.

[144] Python Software Foundation. *Python Language Reference*. Version 3.X. Python Software Foundation. https://www.python.org/, 2023. URL: `https://www.python.org/doc/`.

[145] Tecplot, Inc. *Tecplot 360*. Tecplot, Inc. 2023. URL: `https://www.tecplot.com/products/tecplot-360/#docs`.

List of Figures

List of Tables

A. Appendix

A.1. Remaining k-ε Models

A.1.1. The RNG k-ε Model

To compensate for the deficits of the Standard k-ε Model, such as the occasional overestimation of turbulent viscosity, modified models like the RNG k-ε Model are used. The Renormalization-Group (RNG) k-ε Model develops the transport equations for k and ε using the Renormalization Group Theory [37], a method of statistical physics. Among other things, the interactions in the turbulent energy cascades are approximated in a kind of flow calculation during the derivation. As a result, the same transport equation for k as in the Standard k-ε Model can be used. However, the transport equation for ε undergoes a significant modification, which is as follows:

$$\frac{\partial(\bar{\rho}\varepsilon)}{\partial t} + \nabla(\bar{\rho}\boldsymbol{u}\varepsilon) - \nabla \cdot \left[\left(\mu + \frac{\mu_t}{\sigma_\varepsilon}\right)\nabla\varepsilon\right] = C_1 P_k \frac{\varepsilon}{k} - C_2^* \bar{\rho}\frac{\varepsilon^2}{k} \tag{A.1}$$

The model parameter C_2^* is calculated by the following term:

$$C_2^* = C_2 + \underbrace{\frac{C_\mu \eta^3 \left(1 - \frac{\eta}{\eta_0}\right)}{1 + \beta\eta^3}}_{R} . \tag{A.2}$$

Additionally, for the parameter η, we have

$$\eta = \|S_{ij}\| \cdot \frac{k}{\varepsilon} \quad \text{with } \|S_{ij}\| = \sqrt{2S_{ij} \cdot S_{ij}} \tag{A.3}$$

where $\|S_{ij}\|$ represents the invariant measure of the stress tensor [105] and $S_{ij} = \frac{1}{2}\left[(\nabla\boldsymbol{u})_{ij} + (\nabla\boldsymbol{u})_{ji}\right]$ for the shear rate [60]. The parameter η significantly determines the properties of the RNG k-ε Model and is physically composed of the ratio of the time scale of the turbulence τ_t and the time scale of the mean flow field τ_m as $\eta = \tau_t/\tau_m$. The model constants are partially determined directly during the derivation of the equations and only slightly deviate from those of the Standard k-ε Model, except for σ_ε. The values of the model constants for the RNG k-ε Model are listed in Table 1.These constants are adapted for flows with low shear rates and large time scales of the mean flow. In such flows, $\eta < \eta_0$ and the model produces similar values for k and ε as the Standard k-ε Model. In recirculation zones, where high shear rates prevail and strong streamline curvature is present, $\eta > \eta_0$. This leads to a change in the sign of R in Equation (A.2) and a decrease in the value of C_2^*. Consequently, the dissipation rate ε increases in these areas, while k and μ_t decrease. Therefore, the RNG k-ε Model provides significantly better results in complex flows compared to the Standard k-ε Model [37].

Table 1.: Model constants of the RNG k-ε Model.

C_μ	σ_k	σ_ε	C_1	C_2	η_0	β
0.0845	0.72	0.72	1.42	1.68	4.38	0.012

A.1.2. The Realizable k-ε Model

The Realizable (RLZ) k-ε Model [35] involves a modification only in the model equation for ε, but not for k and μ_t. Some model parameters, which are set as constants in the Standard k-ε Model, are determined here through functional relationships. The equations for the RLZ k-ε Model are given as:

$$\frac{\partial(\bar{\rho}\varepsilon)}{\partial t} + \nabla(\bar{\rho}\boldsymbol{u}\varepsilon) - \nabla \cdot \left[\left(\mu + \frac{\mu_t}{\sigma_\varepsilon}\right)\nabla\varepsilon\right] = \bar{\rho}C_1 \|S_{ij}\| \varepsilon - \bar{\rho}C_2\frac{\varepsilon^2}{k+\sqrt{\mu\varepsilon}}, \tag{A.4}$$

$$\mu_t = C_\mu \bar{\rho}\frac{k^2}{\varepsilon}. \tag{A.5}$$

The model constants are calculated by the expressions:

$$C_1 = \max\left[1, \frac{\eta}{\eta+5}\right] \quad \text{and} \quad \eta = \|S_{ij}\| \cdot \frac{k}{\varepsilon}. \tag{A.6}$$

The unique feature of the RLZ k-ε Model lies in determining the parameter C_μ through a functional relationship involving S_{ij} and the mean rotation $\bar{\Omega}_{ij}$ of the flow field [60]:

$$\bar{\Omega}_{ij} = \frac{1}{2}\left[(\nabla\boldsymbol{u})_{ij} - (\nabla\boldsymbol{u})_{ji}\right] \tag{A.7}$$

leading to

$$C_\mu = \frac{1}{A_0 + A_s\sqrt{S_{ij}S_{ji} + \bar{\Omega}_{ij}\bar{\Omega}_{ji}}\frac{k}{\varepsilon}} \tag{A.8}$$

The model parameters A_0, C_2, σ_ε, and σ_k are constant values, approximately similar to those of the Standard k-ε Model. Table 2 lists the constant model parameters for the RLZ k-ε Model.

Table 2.: Model constants of the Realizable k-ε Model.

σ_k	σ_ε	C_2	A_0
1.0	1.2	1.9	4.04

The model parameter A_s depends solely on the shear rate S_{ij}, leading to the function $A_s = f(S_{ij})$. For a more precise calculation of A_s, refer to Shih et al. [35].

In certain flow configurations, such as stagnation point flows, the RLZ k-ε Model yields physically realistic turbulence values. In such flow conditions, other turbulence models often produce non-physical results

A.2. Calculations and Code for Grid Convergence Study

The representative cell size h of a grid for a three-dimensional simulation with the number of cells N and the volume ΔV_i of the i-th cell, where $h_1 < h_2 < h_3$, is defined as [133]:

$$h = \left[\frac{1}{N} \sum_{i=1}^{N} (\Delta V_i) \right]^{\frac{1}{3}} . \tag{A.9}$$

From this, the refinement factors

$$r_{21} = \frac{h_2}{h_1} \quad \text{and} \quad r_{32} = \frac{h_3}{h_2} \tag{A.10}$$

can be calculated. If ϕ_k stands for a global parameter of the grid with index k, and it holds that $\varepsilon_{32} = \phi_3 - \phi_2$ and $\varepsilon_{21} = \phi_2 - \phi_1$, then the apparent order p of the method is calculated as

$$p = \frac{1}{\ln(r_{21})} \left| \ln \left| \frac{\varepsilon_{32}}{\varepsilon_{21}} \right| + q(p) \right| \tag{A.11}$$

with

$$q(p) = \ln \left(\frac{r_{21}^p - s}{r_{32}^p - s} \right) \quad \text{and} \quad s = 1 \cdot \text{sgn} \left(\frac{\varepsilon_{32}}{\varepsilon_{21}} \right) , \tag{A.12}$$

where for the signum function on the real numbers

$$\text{sgn}(x) := \begin{cases} +1 & \text{if } x > 0 \\ 0 & \text{if } x = 0 \\ -1 & \text{if } x < 0 \end{cases} \tag{A.13}$$

applies. The calculation of p and $q(p)$ must be performed iteratively due to their mutual dependency. Subsequently, the extrapolated values

$$\phi_{21}^{\text{ext}} = \frac{r_{21}^p \phi_1 - \phi_2}{r_{21}^p - 1} \tag{A.14}$$

can be calculated. As representative error values for evaluating a numerical simulation within a grid study, the approximate relative error

$$e_{21}^a = \left| \frac{\phi_1 - \phi_2}{\phi_1} \right| \tag{A.15}$$

and the Grid Convergence Index

$$GCI_{21}^{\text{fine}} = 1.25 \cdot \frac{e_{21}^a}{r_{21}^p - 1} \tag{A.16}$$

are defined.

The Python script outlined below calculates the apparent order of accuracy (p), the correction term ($q(p)$), the Grid Convergence Index (GCI), the extrapolated value (ϕ_{21}^{ext}), and the approximate relative error $(e^a)_{21}$.

```python
import numpy as np

def sign(x):
    """Signum function for x."""
    if x > 0:
        return 1
    elif x < 0:
        return -1
    else:
        return 0

def calculate_p_and_q(r21, r32, epsilon_32, epsilon_21):
    """Calculate p and q(p) iteratively."""
    p = 1  # Initial guess for p
    s = sign(epsilon_32 / epsilon_21)
    for _ in range(100):  # Iterating 100 times for refinement
        q_p = np.log((r21**p - s) / (r32**p - s))
        p = (1 / np.log(r21)) * np.abs(np.log(np.abs(epsilon_32 / epsilon_21)) + q_p)
    return p, q_p

def calculate_gci(e21_a, r21, fs=1.25):
    """Calculate the Grid Convergence Index (GCI)."""
    return (fs * e21_a) / (r21**p - 1)

def calculate_extrapolated_value(phi_1, phi_2, r21):
    """Calculate extrapolated value phi_21_ext."""
    return (r21**p * phi_1 - phi_2) / (r21**p - 1)

# Receive inputs
r21 = float(input("Enter r21: "))
r32 = float(input("Enter r32: "))
phi_1 = float(input("Enter phi_1: "))
phi_2 = float(input("Enter phi_2: "))
phi_3 = float(input("Enter phi_3: "))

# Calculate parameters
epsilon_32 = phi_3 - phi_2
epsilon_21 = phi_2 - phi_1
e21_a = abs((phi_1 - phi_2) / phi_1)
p, q_p = calculate_p_and_q(r21, r32, epsilon_32, epsilon_21)
GCI = calculate_gci(e21_a, r21)
phi_21_ext = calculate_extrapolated_value(phi_1, phi_2, r21)

print(f"Apparent Order of Accuracy (p): {p}")
print(f"Correction Term (q(p)): {q_p}")
print(f"Grid Convergence Index (GCI): {GCI}")
print(f"Extrapolated Value (phi_21_ext): {phi_21_ext}")
print(f"Approximate Relative Error (e^a)_21: {e21_a}")
```

Listing A.1: Python script for Grid Convergence Study

A.3. Code for the calculation of Adiabatic Flame Temperature

```python
import cantera as ct
import numpy as np
import matplotlib.pyplot as plt
import pandas as pd

# Enable LaTeX rendering in Matplotlib and specify XCharter font
plt.rcParams.update({
    'text.usetex': True,
    'text.latex.preamble': r'\usepackage{XCharter}',
    'font.family': 'serif',
    'font.serif': ['XCharter'],
    'text.color': 'black',
    'axes.labelcolor': 'black',
    'xtick.color': 'black',
    'ytick.color': 'black',
})

# Load the reaction mechanism
gas = ct.Solution('DC1S30N18_reaction.yaml')

# Initial conditions
P = 96000
T_inlet = 873.15  # Inlet temperature in K

# Equivalence ratio range for smooth graph
phi_values = np.linspace(0.1, 7.1, 50000)

# Placeholder for results
results = []

for phi in phi_values:
    # Calculate lambda for each phi
    lambda_val = 1 / phi

    # Set the composition based on the equivalence ratio for hydrogen-air combustion
    gas.set_equivalence_ratio(phi, 'H2:1.0', 'O2:0.231, N2:0.769')
    gas.TP = T_inlet, P

    # Compute equilibrium to find adiabatic flame temperature
    gas.equilibrate('HP')
    aft_temp = gas.T

    # Store phi, lambda, and AFT in the results list
    results.append((phi, lambda_val, aft_temp))

# Convert results to a DataFrame
df = pd.DataFrame(results, columns=['Equivalence Ratio (phi)', 'Lambda', 'Adiabatic Flame Temperature (K)'])

# Save to CSV
df.to_csv('phi_lambda_aft.csv', index=False)

# Plotting
plt.figure(figsize=(8, 6))
plt.plot(phi_values, [result[2] for result in results], 'k-', label='AFT vs. $\phi$')  # Continuous line for AFT
```

```python

# Specific lambda values to highlight
specific_lambdas = [2.5, 3, 3.5, 4, 4.5, 5]
# Calculate corresponding phi values for these specific lambdas
specific_phi_values = [1 / lambda_val for lambda_val in specific_lambdas]

# Overlay dots and labels for specific lambda values
for lambda_val in specific_lambdas:
    phi_val = 1 / lambda_val
    # Find the nearest phi in the computed range for accurate labeling
    idx = (np.abs(phi_values - phi_val)).argmin()
    plt.plot(phi_values[idx], [result[2] for result in results][idx], 'ko')  # Place a dot
    plt.text(phi_values[idx]+0.05, [result[2] for result in results][idx], f' $\lambda={lambda_val}$',
             verticalalignment='center', horizontalalignment='left')

plt.xlabel('Equivalence Ratio ($\phi$)')
plt.ylabel('Adiabatic Flame Temperature (K)')
plt.title('Adiabatic Flame Temperature vs. Equivalence Ratio for Hydrogen Combustion')
plt.grid(False)

# Save the plot as a PDF file
plt.savefig('AFT.pdf', format='pdf', bbox_inches='tight')

plt.show()
```

Listing A.2: Python Script for Calculating and Plotting Adiabatic Flame Temperature vs. Lambda for Hydrogen Combustion